Nano and Micro Morphology of Type I Collagen as a Function of Disease and Drug Treatment

by

Meagan A. Cauble

A dissertation submitted in partial fulfillment
of the requirements for the degree of
Doctor of Philosophy
(Chemistry)
in the University of Michigan
2016

Doctoral Committee:

Professor Mark M. Banaszak Holl, Chair
Professor Carol A. Fierke
Associate Professor Kenneth M. Kozloff
Professor Michael D. Morris
Professor Bradford G. Orr

For my dad

This thesis is dedicated to my dad, Mike Cauble, because he loves science as much as I do. Whenever I get stressed about research, he reminds me how exciting and happy science really is. I remember when he made sure that Santa brought me the best telescope and then he helped me learn to use it and we marveled at how pretty the moon was. A decade later, he came to visit me in Ann Arbor after reading about AFM. He knew the year it was invented and brought a lab notebook to lab. He took notes as I prepared a bone sample and then sat at the AFM while I imaged. To this day, he will still ask me if the lyophilizer is still on because he is worried that it should be turned off. My dad is an accountant but he still does all of these things. My dad gives me a place to belong and a place to be excited about science. He will always be my favorite scientist.

ACKNOWLEDGMENTS

The most important person to thank is my research advisor, Dr. Mark Banaszak Holl. He has supported me and provided me with input almost daily for five years. Without him, this thesis would not exist. I want to thank Mark for the time and energy he has invested in me. I can't even count the hours he has spent reading my papers, meeting with me, teaching me something new, sitting at the AFM with me, responding to my text messages when I was excited about an image, or providing compassionate advice when I was having a really hard time. I have learned so much from him and I admire his creativity, intellect, and compassion for his students. I am thankful that God guided me to someone who could not only teach me *a lot* of science, but also someone who cared enough about me to believe in me when I didn't even believe in myself.

I would also like to thank my committee members. My entire committee has been involved from the very beginning and has provided help and valuable insight every step of the way.

Dr. Carol Fierke has been an important member of my committee because she knows an incredible amount of biochemistry. I really appreciate her ideas related to the mechanisms of action for the drug treatments used in my project.

Dr. Ken Kozloff has been particularly helpful because of his expertise in bone biology and bisphosphonate drugs. I met with him throughout my time as a graduate student. I would like to thank him for taking the time to give me bone biology lectures in his office, inviting me to his bone biology lectures for courses he taught, and providing countless ideas and insights into my experiments.

Dr. Morris has been an important committee member for his expertise in characterizing bone with Raman spectroscopy. Through our interactions, he has taught me about the material properties of bone and the mineralization of bone. He has also provided ideas and insight to experiments.

Dr. Brad Orr has been especially involved in my time as a graduate student because he has been at every group meeting, is an expert at AFM, and has provided valuable feedback throughout

the five years. Anytime there is an AFM problem that seems impossible to solve – Brad will have the answer! He is brilliant at physics and AFM.

There are several collaborators that have made this thesis possible:

Merck Research Laboratories funded a large portion of the thesis and provided the rabbit samples for chapters 2, 3, and 4. Dr. Le Duong and Dr. Brenda Pennypacker were very important to this thesis. They were the driving force behind obtaining funding, running the animal studies, and providing experiment ideas and insight. I want to thank Dr. Le Duong for taking the time to provide experiment ideas and teaching our group about bone biology. I admire her for her success and her incredible knowledge of bone biology and osteoporosis drugs. I hope I can know as much as her one day!

Kathy Welch and Ed Rothman from CSCAR developed the statistical methods used in chapters 2 and 3. I am very thankful for their time and effort into developing those methods and running the statistical models on all of my data. I also want to thank Ed Rothman for teaching me in an independent study statistics course.

Dr. Jeff Fessler and Dr. Matt Muckley developed the methods to calculate the fibril alignment parameter in chapter 3. That chapter would not have been possible without them and I am very grateful for their time and effort.

Chapter 4 would not have been possible without our collaborators Jan Gebauer and Ulrich Baumann at the University of Cologne in Germany. They provided the PEDF protein that was recombinantly made with a streptavidin tag attached.

I am very lucky to have a family that supports me as much as they do. My entire extended family has been cheering me on from the beginning. I am so thankful to have my mom to talk to anytime I want and she will listen to all of my stories. I can call her to vent because I'm stressed or I can call her excited about an experiment. She is my best friend. My dad is always genuinely interested in my research even though he is not in a science field and he makes me feel significant. He shares my excitement for science and I cherish that special bond we have. My parents have done everything possible to make sure I have everything I need to succeed. From buying cool science books in middle school, to spontaneously buying me a new laptop while writing my thesis – my parents are always there to love me and help me. My sister, Meredith, and my brother-in-

law, Shawn, played a big role in helping me get past some difficult times in graduate school. I am so thankful to have their unconditional love.

Johanna Soet has met with me weekly. Her office is the one place that I know I can say anything and I'm not going to be judged. She is the only person who really understands what graduate school was like for me behind the scenes. When I felt like I didn't belong and there was nobody in the world who could talk to me and understand what I was going through – Johanna was *always* on my side and is the most nonjudgmental person I've ever met. I am very thankful that she invested so much time and energy into helping me.

Dr. Marcus Lay was my undergraduate research advisor and Dr. Pornnipa Vichchulada was my graduate student research mentor. They are the real reason that I am so excited and passionate about research. From day one, they gave me a real research project to work on and not just busy work. They believed in me and constantly encouraged me to see myself the way they see me. They became very special people in my life and were more than just people I saw in lab. They even came to my dance recital in college! They both kept in touch with me throughout graduate school to offer advice. I would never have had the opportunity to be a graduate school at UM if Dr. Lay and Pornnipa did not give the abundant opportunities that I had in their lab: talks at conferences, posters at national conferences, the Goldwater scholarship, nominating me for various awards, etc. I am so thankful that they are a part of my life.

TABLE OF CONTENTS

LIST OF FIGURES

LIST OF SCHEMES

LIST OF TABLES

LIST OF APPENDICES

LIST OF ABBREVIATIONS

Alendronate = ALN

Atomic Force Microscopy = AFM

Bone Mineral Density = BMD

Cathepsin K Inhibitor = CatKI

Ethylenediaminetetraacetic acid = EDTA

Estrogen Replacement Therapy = ERT

Fibril Alignment Parameter = FAP

Generalized estimating equation = GEE

Kolmogorov-Smirnov = KS

Lumbar Vertebrae = LV

Ovariectomized = OVX

ABSTRACT

Type I collagen, the most abundant protein in the human body, is the primary organic component of bone and forms fibrils with a periodic spacing (D-spacing) along the fibril axis. These collagen fibrils are organized into larger hierarchical structures. Using atomic force microscopy (AFM), individual microfibrils were quantitatively characterized and a minimum of 90 collagen molecules were required before D-spacing was observed. The arrangement of type I collagen fibrils into microstructures in bone tissue altered upon estrogen depletion, a model for postmenopausal osteoporosis, as well as drug treatments for osteoporosis.

Micro-scale structural changes were measured in a rabbit animal model from the following treatment groups: Sham, ovariectomized (OVX), OVX + alendronate (ALN), OVX + cathepsin K inhibitor (CatKI), and OVX + estrogen replacement therapy (ERT). AFM images were collected for 84 animals across all five treatment groups. A fibril-by-fibril analysis was conducted by hand-coding fibrils into *Parallel* (collagen bundles or collagen sheets) or *Oblique* microstructures. In cortical bone, OVX increased the proportion of fibrils coded as *Oblique* and decreased the proportion of fibrils coded as *Parallel* with statistical significance ($p < 0.05$). Treatment with ALN or ERT partially prevented this change from occurring and treatment with CatKI completely prevented this change from occurring within error.

An automated imaged level analysis was conducted using an autocorrelation technique and calculating a fibril alignment parameter (FAP) to describe the degree of local collagen fibril alignment in an image. At this level of hierarchical structure, OVX altered trabecular bone and showed no changes to cortical bone. Treatment with CatKI prevented the trabecular microstructural change from occurring but also introduced a change to the cortical bone. Treatment with ALN altered both the cortical and trabecular microstructure.

Sites of collagen interactions with the collagen chaperone PEDF, pigment epithelium derived factor, were imaged in bone tissue by phase imaging during tapping mode AFM. Gold nanoparticles were used as a secondary tag on PEDF to allow detection of PEDF binding in tissue. PEDF bound heterogeneously and was detected between collagen fibrils with a low amount of alignment.

Chapter 1
Introduction

1.1 Negative Impact of Osteoporosis

Osteoporosis, or "porous bone," is a debilitating disease that causes low bone mass and increased bone fracture risk.[1] According to the National Osteoporosis Foundation, 54 million Americans were affected by osteoporosis and low bone mass in December 2015.[2,3] Osteoporosis is responsible for two million broken bones and $19 billion in medical expenses every year in the United States. One in two women and one in four men aged 50 or older will break a bone due to osteoporosis.[2] Typically located in the spine, hip, or wrist,[1] the number of osteoporotic fractures surpasses breast cancer, stroke, and heart attacks.[4]

This disease has a powerful negative impact on the quality of life.[1,5] Bones weakened from osteoporosis can fracture with stresses as minimal as sneezing or bumping into furniture.[2] As the bone weakens, chronic localized pain may develop. Spinal vertebrae are often affected by osteoporosis and a vertebrae fracture or collapse can lead to a stooped or hunched posture, along with acute, debilitating pain.[5] Many people who suffer from osteoporosis will ultimately develop depression due to the isolation, and loss of lifestyle caused by compromised mobility, along with pain and generally declining quality of life.[2,5]

When a senior breaks a bone, they often need long term nursing care.[5] 20% of seniors who break a hip will die within one year due to complications with the broken bone itself or the surgery to treat the broken bone.[2] Within this demographic, the stress caused by the trauma of the broken bone and displacement from the customary domicile during the extended rehabilitation period, triggers an accelerated death rate from pneumonia, heart attack and stroke.

Osteoporosis is sometimes called a "silent disease" because there are often no symptoms until there is a broken bone. A woman's risk of breaking a hip is equal to her combined risk of breast, uterine, and ovarian cancer. Post-menopausal women are particularly susceptible to osteoporosis because of the dramatic decrease in estrogen after menopause.[6–8] The disease has

become more common as the age of life expectancy has increased.[1,2,6,9] A 50 year old woman in the United States has a 40% lifetime risk of an osteoporotic fracture. A third of women and an eighth of men over age 80 will have a hip fracture at some point and 15-20% of those people will die from complications.[6] With such a large portion of the population suffering from the disease, it is important that accurate and reliable diagnostic methods are in place as well as treatments for individuals who battle this disease.

1.2 Current Diagnostic Methods

The standard procedure for the diagnosis of osteoporosis is to measure bone mineral density (BMD) using dual-energy X-ray absorptiometery (DEXA). An individual's BMD value is compared to the distribution of BMD values for young adults to generate a T-score. A T-score indicates how much a given BMD value deviates from the mean BMD value in a population. For example, a T-score of -1.0 would mean that the BMD for that individual is one standard deviation lower than the mean BMD value for a population of young adults.[4,10]

According to the World Health Organization (WHO), a T-score of ≤ 2.5 is diagnostic of osteoporosis.[3,4] However, BMD is not always a good predictor of bone fracture risk and a large proportion of postmenopausal women who experience bone fractures have a normal T-score.[11] As shown in **Figure 1.1**, a high bone turnover rate is associated with osteoporotic fractures independently of BMD.[12] It is interesting to note that there is a higher incidence of osteoporotic fracture with a high BMD and high bone turnover rate than there is with low BMD, which is the diagnostic standard for osteoporosis. A high rate of bone remodeling can change the architecture of the bone without change the bone mass or BMD.[4] This can have negative effects on the bone strength.[4]

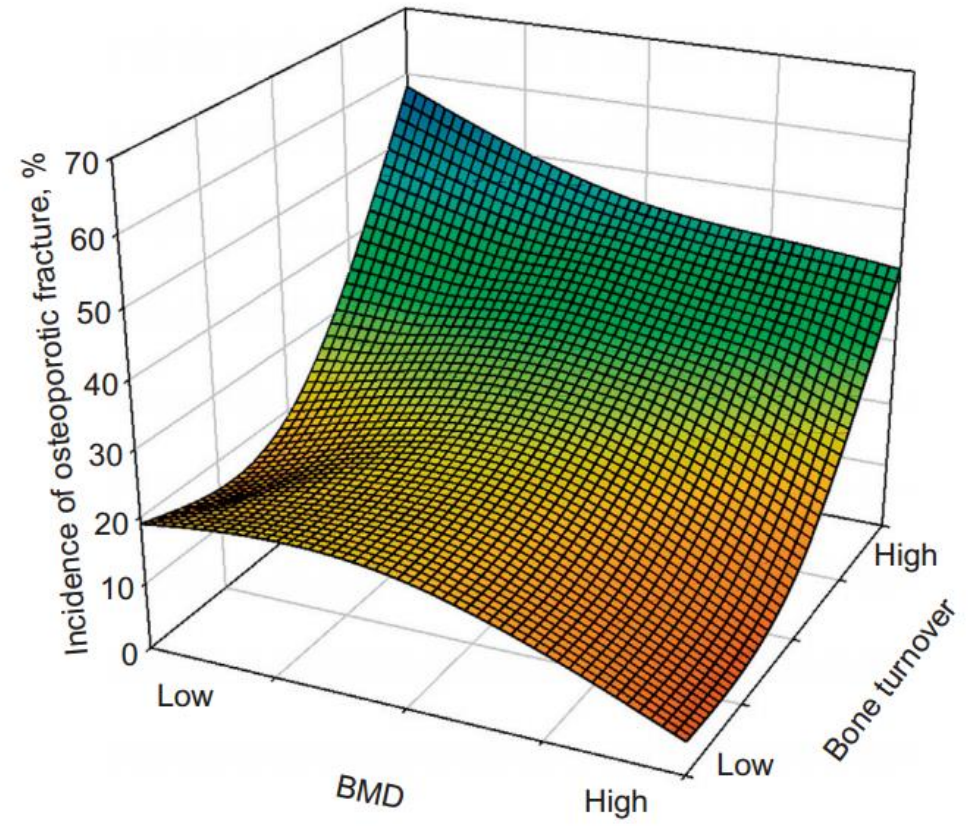

The incidence of osteoporotic fracture is related to bone density (BMD), but also to the degree of bone turnover. In general, patients with higher bone turnover or lower BMD have more fractures. Patients with both these features have the highest risk of fractures. *Adapted from Meier et al. J Bone Miner Res 2005;20:579–587.*

Figure 1.1 Reprinted from Basic and Applied Bone Biology 2014; Burr and Allen[4]

BMD and bone remodeling rate influence bone fracture risk independently as well as resulting in an even greater risk when both factors are present. Bone remodeling rates can be altered by estrogen depletion and various drug treatments, as described in the next several sections. The overall theme of this thesis is to understand how estrogen depletion and drug treatments alter the architecture of bone at the level of type I collagen fibrils, the primary protein component of the bone.

1.3 Effects of Estrogen Depletion on Bone Architecture and Bone Remodeling

Estrogen plays a key role in bone mass homeostasis by inducing osteoclast apoptosis[13] to suppress remodeling on both trabecular and endocortical surfaces. Production of receptor activator of the NF-KB ligand (RANKL) by osteoblasts and bone marrow stromal cells is inhibited by estrogen. In addition, estrogen increases the production of osteoprotegerin (OPG). When estrogen levels decline with menopause, the balance of RANKL and OPG is altered and the results are increased osteoclast differentiation, stimulation of osteoclast activation on bone surfaces, and reduction of osteoclast apoptosis. In summary, the loss of estrogen leads to an increase in osteoclast-mediated bone resorption.[4,8]

The cellular changes caused by estrogen depletion lead to dramatic changes in the overall architecture of both cortical and trabecular bone. In addition to reduced bone volume, trabecular bone experiences a decrease in connectivity and thinning of the trabeculae. Cortical bone undergoes thinning over time and this is observed in the long bones as well as the femoral neck and cortical shell of lumbar vertebrae. In the long bones, cortical thinning is often compensated for by apposition of bone at the periosteal surface, which increases the diameter. This compensation is not observed elsewhere. In addition to cortical thinning, the femoral neck also experiences increased porosity.[4,13]

1.4 Osteoporosis Treatments

1.4.1 Bisphosphonates

Bisphosphonates are a class of antiresorptive agents that are structurally similar to pyrophosphate and contain a "P-C-P" backbone (**Figure 1.2**).[6,14] Pyrophosphate binds to hydroxyapatite in bone and is involved in various biochemical pathways once taken in by osteoclasts. The substitution of a carbon atom for the central oxygen atom makes the molecule more stable and prevents hydrolysis inside the cell.[14] There are two side chains available for substitution on the central atom of the bisphosphonate. A hydroxyl group on one side chain increases the affinity for hydroxyapatite and the other side chain determines potency of the drug.[14]

Alendronate (**Figure 1.2**) was the first orally available bisphosphonate in the United States for the treatment of postmenopausal osteoporosis[1] and is marketed by Merck. Bisphosphonates enter the osteoclast during resorption and the downstream cellular effects of the drug lead to a loss of the osteoclast's characteristic "ruffled border" morphology and resorptive activity. These

changes lead to apoptosis of the osteoclast. The nitrogen containing bisphosphonates, such as alendronate, are hypothesized to induce osteoclast apoptosis by interfering with the prenylation of membrane proteins and thus the signaling function of key regulatory proteins.[6,14]

Several concerns with the long-term use of bisphosphonate drugs have led to the development of alternative therapies for osteoporosis.[15,16] Bone formation and resorption are coupled processes. The antiresorptive activity of bisphosphonates ultimately leads to suppression of bone formation due to the elimination of signaling between osteoclasts and osteoblasts. In addition, the sustained secondary mineralization of older bone coupled with a decrease in bone turnover results in an overall increase in tissue mineral content. This is initially an advantage because the bone becomes stiffer. However, over time the bone will become more mineralized and more homogeneous. Long-term use of bisphosphonates can lead to brittle bones and this is a concern that has led to the development of alternative drugs.[6]

1.4.2 Cathepsin K Inhibitors

Cathepsin K is a lysosomal protease highly expressed by osteoclasts and is the primary collagenase responsible for osteoclast-mediated bone resorption. Studies have shown that treatment with a cathepsin K inhibitor (CatKI) in rats[17] and monkeys[18] produces biochemical markers of bone resorption and increased BMD. Numerous CatKIs have been developed for the treatment of various conditions including osteoporosis, osteoarthritis, metastatic bone disease, and atherosclerosis.[19] In order to treat post-menopausal osteoporosis, it is important to minimize off-target activity of the drug and maximize selectivity for the cathepsin K enzyme in bone. A 2007 review by Black and Percival goes into great detail on the many structural designs considered for a therapeutic cathepsin K inhibitor.[19] The most successful drug candidate to date is MK-0822, or odanacatib, developed by Merck. Odanacatib (Figure 1.2) is the most selective and bioavailable CatKI developed to date. This drug has been successful in clinical trials and is near the end of the FDA approval process for the treatment of post-menopausal osteoporosis.[20]

Merck, Inc. has worked develop alternatives to odanacatib. In 2010, MK-0674 (**Figure 1.2**) was reported as a CatKI that is structurally similar to odanacatib, is orally bioavailable, and is a good drug candidate with a different metabolic profile from odanacatib.[21]

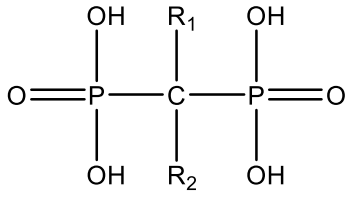

bisphosphonate

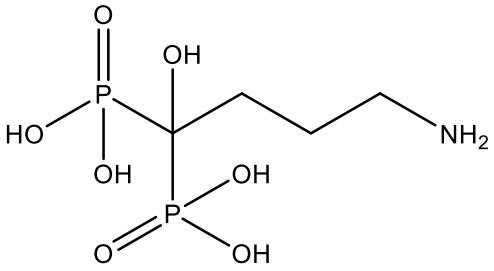

alendronate

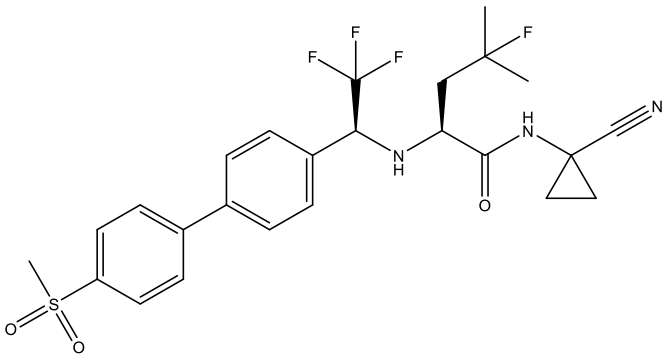

odanacatib

Figure 1.2 Chemical structures for bisphosphonates and various cathepsin K inhibitors

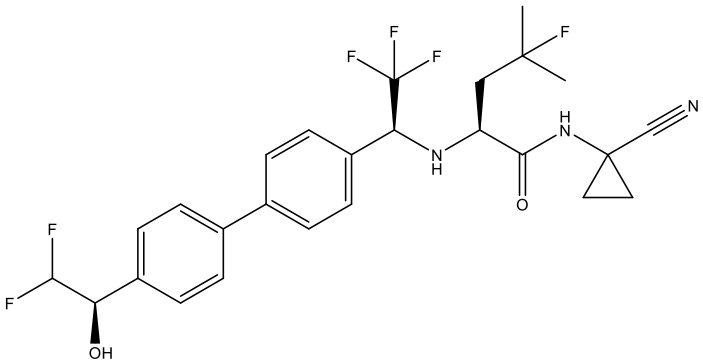

MK-0674

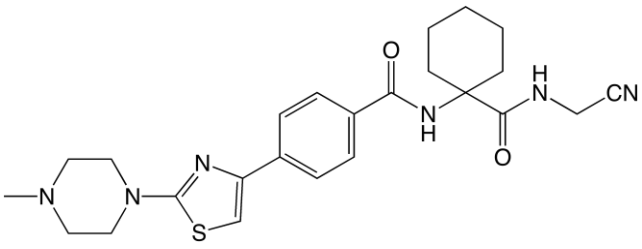

L-235

1.5 Rabbit Animal Model to Study the Effect of Drug Treatments on Nano and Micro Structure of Type I Collagen in Bone

The effects of alendronate and the CatKI L-235 (**Figure 1.2**) have been studied in a rabbit animal model developed at Merck Research laboratories.[22] New Zealand white female rabbits were weight-randomized into two groups: Sham + vehicle or ovariectomy (OVX) + vehicle. The OVX animals were again weight-randomized and either received no drug or received alendronate, the CatKI L-235, or estrogen replacement therapy. The animal models are summarized in **Figure 1.3**.

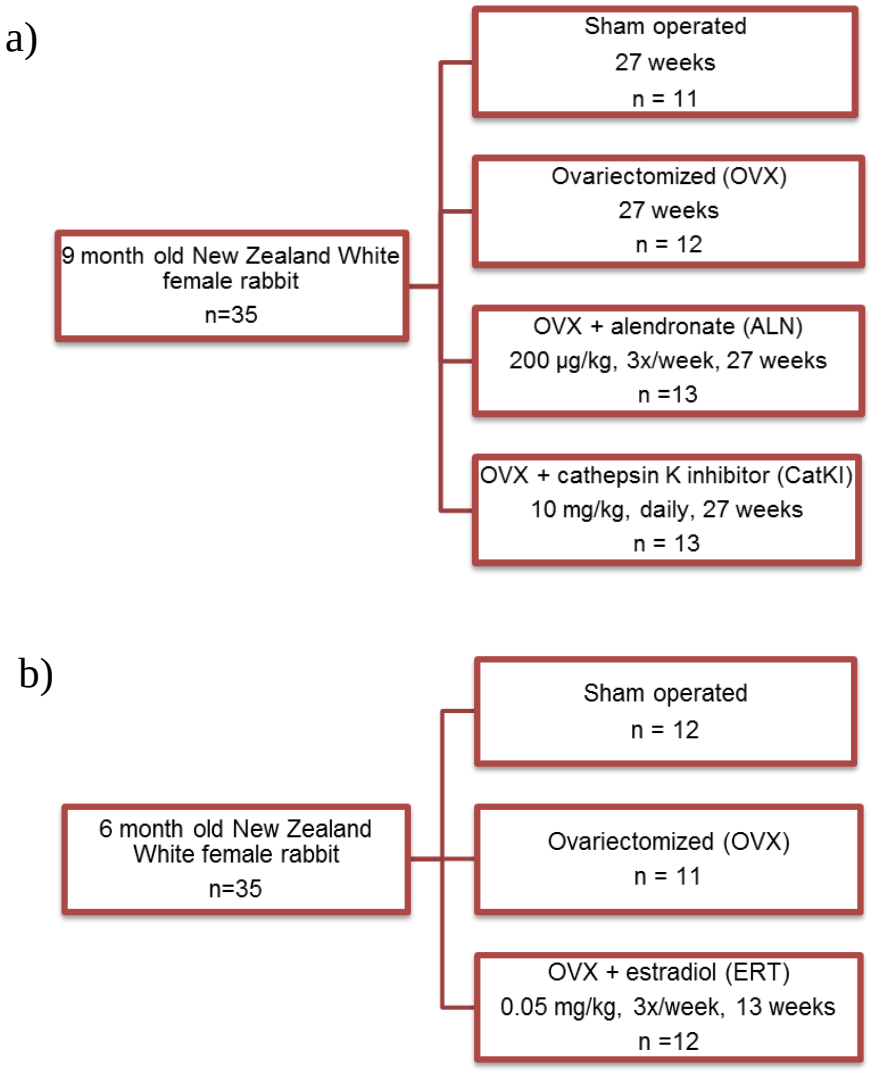

Figure 1.3 Summary of animals used to study effects of drug treatments on nano and micro structure of type I collagen in bone. a) "Data Set I" in Chapter 2, page 13; Chapter 3, page 22. b) "Data Set II" in Chapter 2, page 13.

Atomic force microscopy (AFM) was used to study the nano and micro structure changes of type I collagen[23] in response to the treatments outlined in **Figure 1.3**. Several metrics of assessing nano/micro structure were used. An analysis of D-spacing can be found in chapters 2 (page 13), 3 (page 22), and 5 (page ##). For many years, the D-spacing of type I collagen fibrils was thought to be a single value of 67 nm. The origin of D-spacing in collagen fibrils was first presented by the Hodge Petruska model[24] and is shown in Figure 1.4. In this model, 300 nm tropocollagen molecules stack in an organized fashion to produce a pattern of "gap" and "overlap" regions. These gap and overlap regions generate a single 67 nm spacing. The Orgel model for the origin of D-spacing (**Figure 1.5**) also only accounts for a single value.[25–27]

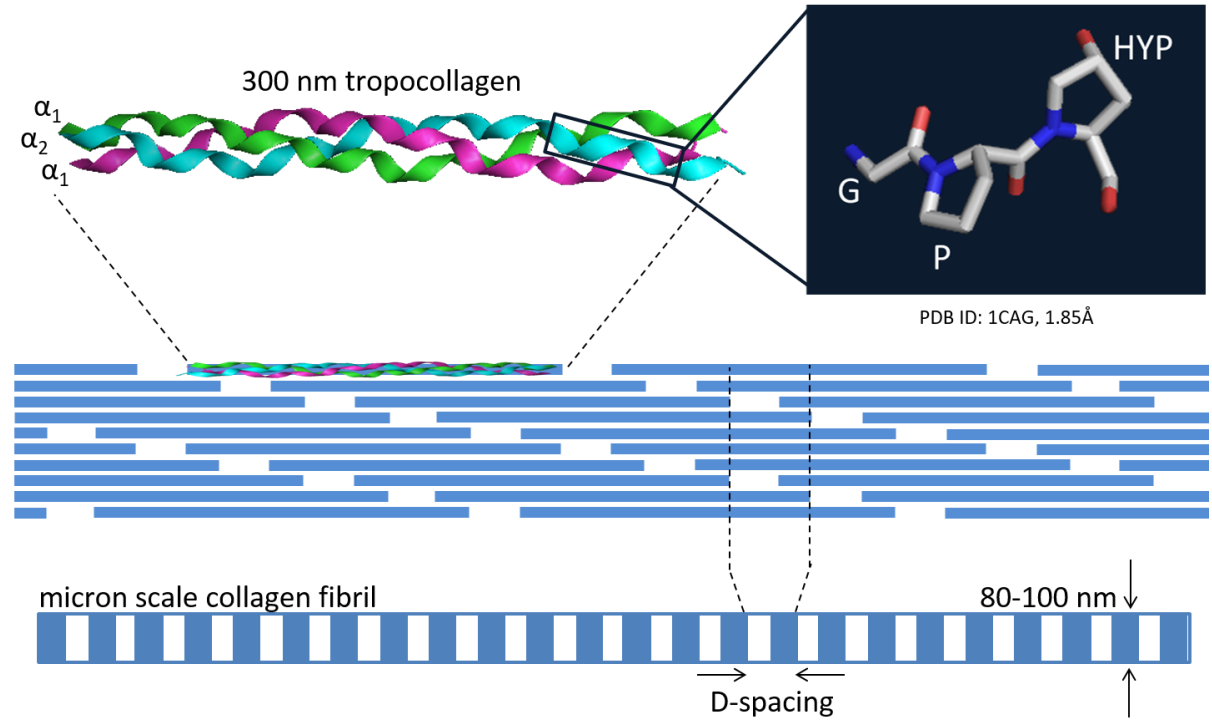

Adapted from: Hodge, A. J. and Pertruska J. A. *Aspects of Prot. Struct.* **1963** 289-300.

Figure 1.4 The Hodge Petruska model

Type I collagen peptides self-assemble into triple helical tropocollagen molecules that are 300 nm in length. The Hodge Petruska model proposes that these tropocollagen units stack to produce areas of "gap" and "overlap" that are observed as the D-spacing.

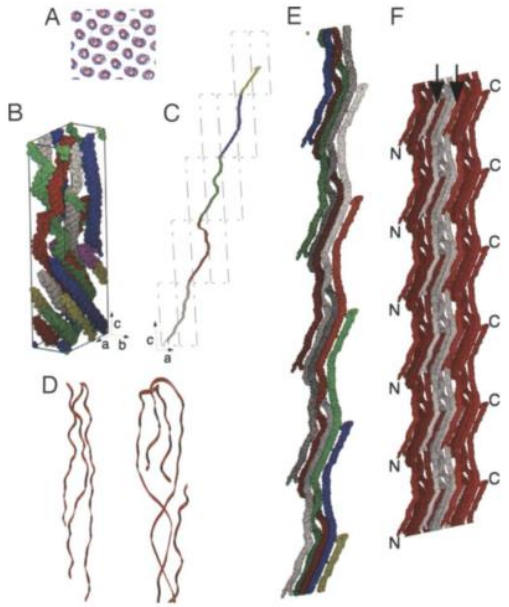

Figure 1.5 The Orgel model
Reprinted from Orgel et al. **2006** *Proc. Natl. Acad. Sci. USA* 103 (24) 9001-9005[26]

In this model, collagen molecules pack quasihexagonally to produce microfibrils. Each collagen molecule interacts with two other collagen molecules and forms an intermicrofibrillar crosslink at a C-terminal peptide.

AFM is capable of measuring the D-spacing for individual collagen fibrils.[28] This method removes averaging and generates a distribution of D-spacing values. Type I collagen exhibits a distribution of values in both mineralized and non-mineralized tissue including bone, skin, tendon, and teeth.[29] In addition, the distribution of D-spacing values can change as a function of disease.[30] These studies provided the motivation to analyze the D-spacing distributions as a function of estrogen depletion and drug treatment in the rabbit animal model (Chapters 2 and 3).

This thesis reports the development of two additional metrics to access changes in nano and microstructure of type I collagen in bone. The proportion of collagen fibrils in a *Parallel* or *Oblique* microstructure is reported in chapter 2[31] for cortical bone (page ##) and chapter 3 for trabecular bone (page ##). In this method, fibrils with a defined D-spacing were hand coded as being in a *Parallel* microstructure or *Oblique* microstructure. The *Parallel* microstructure consisted of collagen fibrils that were aligned in the same direction in bundles (3-15 fibrils associated with one another) or sheets (>20 fibrils continuous with surrounding bone). *Oblique* microstructures contained fibrils with a wide array of angles between. The proportion of fibrils in these two categories was measured for estrogen depleted and drug treated groups.

A larger scale assessment of structure was analyzed by calculating a fibril alignment parameter (chapter 3, page 22). This method considers fibril structure at the level of an entire AFM image. The *Parallel*/*Oblique* method had limitations because it is time intensive and requires measurements to be put into one of only two categories. The development of the fibril alignment parameter was an automated approach that removed the hand coding and allowed images to be given a measurement with a continuous variable.

1.6 References

1. Johnell, O. & Kanis, J. A. An estimate of the worldwide prevalence, mortality and disability associated with hip fracture. *Osteoporos. Int.* **15,** 897–902 (2004).
2. National Osteoporosis Foundation. (2016). Available at: nof.org.
3. Wright, N. C. *et al.* The recent prevalence of osteoporosis and low bone mass in the united states based on bone mineral density at the femoral neck or lumbar spine. *J. Bone Miner. Res.* **29,** 2520–2526 (2014).
4. Imel, Erik A. (Department of Medicine and Pediatrics, I. U. S. of M., DiMeglio, Linda A. (Department of Pediatrics, I. U. S. of M. & Burr, David B. (Department of Anatomy and Cell Biology, I. U. S. of M. in *Basic and Applied Bone Biology* (eds. Burr, D. (Indiana U. S. of M. and I. U.-P. U. & Allen, M. (Indiana U. S. of M.) 317–344 (Elsevier Inc., 2014).
5. Lips, P. & van Schoor, N. M. Quality of life in patients with osteoporosis. *Osteoporos. Int.* **16,** 447–455 (2005).
6. GJ, S. Decimal point - osteoporosis therapy at the 10-year mark. *N. Engl. J. Med.* **350,** 1172 (2004).
7. Sornay-Rendu, E. & Delmas, P. D. Advances in osteoporosis diagnosis: the use of clinical risk factors. *Medicographia* **30,** 350–3698 (2008).
8. Syed, F. & Khosla, S. Mechanisms of sex steroid effects on bone. *Biochem. Biophys. Res. Commun.* **328,** 688–696 (2005).
9. Wade, S. W., Strader, C., Fitzpatrick, L. A. & Anthony, M. S. Sex- and age-specific incidence of non-traumatic fractures in selected industrialized countries. *Arch. Osteoporos.* **7,** 219–227 (2012).
10. Griffith, J. F. & Genant, H. K. New advances in imaging osteoporosis and its complications. *Endocrine* **42,** 39–51 (2012).

11. Ruppel, M. E., Miller, L. M. & Burr, D. B. The effect of the microscopic and nanoscale structure on bone fragility. *Osteoporos. Int.* **19,** 1251–1265 (2008).
12. Meier, C., Nguyen, T. V, Center, J. R., Seibel, M. J. & Eisman, J. A. Bone Resorption and Osteoporotic Fractures in Elderly Men: The Dubbo Osteoporosis Epidemiology Study. *J. Bone Miner. Res.* **20,** 579–587 (2004).
13. Weitzmann, M. N. & Pacifici, R. Estrogen deficiency and bone loss: an inflammatory tale. *J. Clin. Invest.* **116,** 1186–1194 (2006).
14. Russell, R. G. G. & Rogers, M. J. Bisphosphonates: From the laboratory to the clinic and back again. *Bone* **25,** 97–106 (1999).
15. Neviaser, A. S., Lane, J. M., Lenart, B. a, Edobor-Osula, F. & Lorich, D. G. Low-energy femoral shaft fractures associated with alendronate use. *J. Orthop. Trauma* **22,** 346–350 (2008).
16. Rizzoli, R. *et al.* Osteonecrosis of the jaw and bisphosphonate treatment for osteoporosis. *Bone* **42,** 841–847 (2008).
17. Barrett, D. G. *et al.* P2-P3 conformationally constrained ketoamide-based inhibitors of cathepsin K. *Bioorganic Med. Chem. Lett.* **15,** 3540–3546 (2005).
18. Kumar, S. *et al.* A highly potent inhibitor of cathepsin K (relacatib) reduces biomarkers of bone resorption both in vitro and in an acute model of elevated bone turnover in vivo in monkeys. *Bone* **40,** 122–131 (2007).
19. Cameron Black, W. & David Percival, M. Chapter 8 Cathepsin K Inhibitors. *Annu. Rep. Med. Chem.* **42,** 111–127 (2007).
20. Gauthier, J. Y. *et al.* The discovery of odanacatib (MK-0822), a selective inhibitor of cathepsin K. *Bioorganic Med. Chem. Lett.* **18,** 923–928 (2008).
21. Isabel, E. *et al.* The discovery of MK-0674, an orally bioavailable cathepsin K inhibitor. *Bioorganic Med. Chem. Lett.* **20,** 887–892 (2010).
22. Pennypacker, B. L. *et al.* Cathepsin K inhibitors prevent bone loss in estrogen-deficient rabbits. *J. Bone Miner. Res.* **26,** 252–262 (2011).
23. Wallace, J. M. Applications of atomic force microscopy for the assessment of nanoscale morphological and mechanical properties of bone. *Bone* **50,** 420–427 (2012).
24. John A. Petruska & Hodge, A. J. A Subunit model for the Tropocollagen Macromolecule. *Proc. Natl. Acad. Sci.* **51,** 871–876 (1964).

25. Orgel, J. P. R. O. *et al.* The in situ supermolecular structure of type I collagen. *Structure* **9,** 1061–1069 (2001).
26. Orgel, J. P. R. O., Irving, T. C., Miller, A. & Wess, T. J. Microfibrillar structure of type I collagen in situ. *Proc. Natl. Acad. Sci. U. S. A.* **103,** 9001–9005 (2006).
27. Orgel, J. P. R. O., Persikov, A. V. & Antipova, O. Variation in the helical structure of native collagen. *PLoS One* **9,** 1–11 (2014).
28. Erickson, B. *et al.* Nanoscale structure of type I collagen fibrils: Quantitative measurement of D-spacing. *Biotechnol. J.* **8,** 117–126 (2013).
29. Wallace, J. M. *et al.* Type i collagen exists as a distribution of nanoscale morphologies in teeth, bones, and tendons. *Langmuir* **26,** 7349–7354 (2010).
30. Wallace, J. M., Erickson, B., Les, C. M., Orr, B. G. & Banaszak Holl, M. M. Distribution of type I collagen morphologies in bone: Relation to estrogen depletion. *Bone* **46,** 1349–1354 (2010).
31. Cauble, M. A. *et al.* Alteration of Type I collagen microstructure induced by estrogen depletion can be prevented with drug treatment. *Bonekey Rep.* **4,** 697 (2015).

Chapter 2

Alteration of Type I Collagen Microstructure Induced by Estrogen Depletion can be Prevented with Drug Treatment

Meagan A Cauble, Edward Rothman, Kathleen Welch, Ming Fang, Le T Duong, Brenda L Pennypacker, Bradford G Orr, and Mark M Banaszak Holl

Reprinted from BoneKEy Reports **4**, 697 (2015)

2.1 Introduction

Reduction of estrogen level affects over 75 million people worldwide by inducing *Osteoporosis* and *Osteopenia*, decreasing overall bone quality, and increasing susceptibility to fracture.[1,2] Clinical and scientific assessments have focused heavily on bone mineral density (BMD) as the primary assay of bone quality and drug treatment outcomes. However, BMD has demonstrated limitations for predicting bone fracture and understanding the roles of estrogen in bone quality, formation, and resorption.[3–5] In particular, BMD is unable to assess changes in Type I collagen structure that are key to understanding bone toughness. The structural changes that occur in Type I collagen matrix under conditions of estrogen depletion and drug treatment remain largely unknown. Here we show that the Type I collagen microstructure is altered by estrogen depletion and that this change is largely prevented by treatment with a Cathepsin-K inhibitor (CatKI) and partially prevented with bisphosphonate or estradiol treatment. These observations are particularly surprising for the bisphosphonate drug, which was developed to help maintain BMD, and represents a new understanding of biochemical activity for this decades-old therapeutic. The ability of an inhibitor of the collagenase cathepsin-K to prevent estrogen-induced changes in Type I collagen microstructure is also previously unknown.

2.2 Results

Changes in Type I collagen microstructure and nanomorphology are conveniently measured using atomic force microscopy (AFM).[6,7] Recent AFM studies indicated changes in the nanomorphology of the Type I collagen fibrils in ovariectomized (OVX) sheep[8–10] and rats.[11] In order to explore the effect of estrogen depletion and compare efficacy of CatKI and alendronate (ALN) drug treatments, the rabbit OVX model was developed by Merck Inc., as human CatKI's exhibit similar potency for the rabbit enzyme and the adult rabbit skeleton undergoes substantial cortical Haversian remodeling (unlike the rodent).[12] Nine-month-old New Zealand white female rabbits (Data Set I) underwent the following treatments: sham operation + vehicle (n = 11), ovariectomy + vehicle (OVX; n = 12), OVX + 200 μg/kg ALN, 3 × a week for 27 weeks (n = 12) and OVX + 10 mg/kg CatKI L-235 daily for 27 weeks (n=13). Treatments were initiated three days after surgery. Data Set II consisted of 6-month-old New Zealand white female rabbits that underwent the following treatments: sham operation + vehicle (n = 12), ovariectomy + vehicle (OVX; n = 12) and OVX + 0.05 mg/kg 17β-estradiol (ERT) 3 × a week for 13 weeks (n = 12). Treatments were initiated 17 days after surgery. Both studies were performed in prevention mode with drug dosing initiated soon after surgery. Sample sets were stored in 95% ethanol. Rabbit cortical femur samples were polished for 90 s, followed by sonication for 5 min. Demineralization was carried out for 90 min (9-month-old) or 120 min (6-month-old) using 0.5 M EDTA at pH 8.0. The samples were sonicated for 5 min before imaging. We confirmed that ethanol fixation did not change the overall distribution of collagen fibril D-spacings or microstructure by direct comparison with the analysis of fresh, frozen rabbit bone. AFM images were obtained using tapping mode in air using silicon cantilevers (tip radius 10 nm, force constant 40 N/m and resonance frequency 300 kHz). Details on sample preparation, imaging and image analysis protocols for Type I collagen in bone have been previously published.[6] Images were obtained from locations from across the full 1.00 × 0.75-cm section of the femur mid-diaphysis (Figure A.1). All images were acquired in the plane parallel to the long bone axis and obtained from polished regions 100-300 μm below the bone surface. No variation in collagen structure was noted as a function of the polishing depth employed. Image acquisition for the mid-diaphysis sections proceeded using the follow procedure. First, 30 × 30-μm scans were obtained in six regions of the 1.00 × 0.75-cm bone imaging area. These were followed by 10 × 10 μm scans, and finally the 3.5 × 3.5-μm scans employed for image analysis. This approach ensured that the nano- to micro-scale analysis of

collagen fibrils was distributed across the 1.0 × 0.75-cm imaging area. An average of six 30 × 30-μm scans and thirteen 3.5 × 3.5-μm scans were obtained per animal. From these regions, the average of 75 fibrils per animal was obtained. The local microstructure about each fibril was examined and coded as either *Parallel* or *Oblique*. In a given image area, it is thus possible for both *Parallel* and *Oblique* fibrils to be present. Furthermore, the assignment is indicative of a local order between fibrils with a length scale of a few hundred nanometers. The assessment does not provide evidence, one way or the other, of overall micron- to millimeter-scale order as typically measured using X-ray diffraction methods.

Exemplar images highlighting the features observed in the local structural organization of the fibrils are illustrated in **Figure 2.1**. We noted two major qualitative features in the images: (1) *Parallel* regions of fibrils with subclasses of bundles (3-15 fibrils aligned in parallel with defined edges) and sheets (> 20 fibrils aligned in planar, parallel manner); (2) *Oblique* regions of fibrils exhibiting an angular range of fibril orientation. For all samples, the nanomorphology of individual fibrils, as quantified using the metric of the D-spacing, was measured, and each fibril was coded (blinded of the sample origin) for its local microstructure. Fibrils coded as present in bundles or sheets (**Figure 2.1a**) were grouped together as *Parallel* regions. A number of other features were also coded including fibril pairs and individual fibrils crossing bundles or sheets (**Figure A.2**). Roughly half of the fibrils observed were present in structures without the same degree of parallel alignment, exhibited a wide range of fiber-fiber angular dispersion and were classified as being present in *Oblique* regions (**Figure 2.1b**). A total of 5673 individual fibrils were classified from 1081 3.5 × 3.5-μm images from a total of 94 animals across the seven experimental groups. The coding and frequency of *Parallel* and *Oblique* observations are summarized in **Table 2.1**. In all cases, the *Parallel* and *Oblique* codings captured

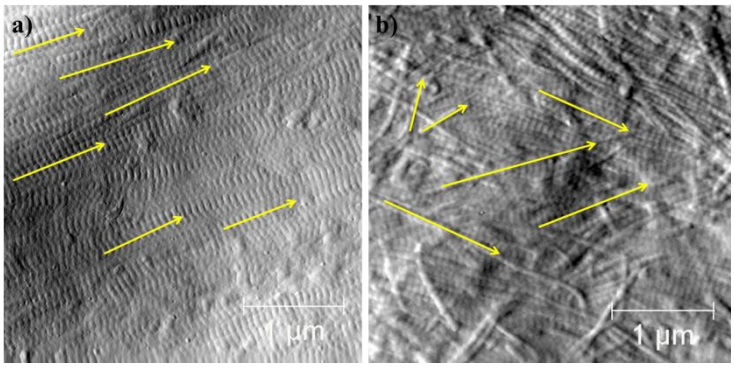

Figure 2.1 AFM images illustrating *Parallel* and *Oblique* regions of Type I collagen fibrils. a) Parallel region showing multiple aligned fibrils (yellow arrows); b) oblique region showing multiple fibrils with varying alignment (yellow arrows). 3.5 × 3.5 μm image.

≥95% of all measured fibrils. Additional exemplar images for the Sham, OVX, ALN, CatKI and ERT treatments are provided in **Figure A.4**.

To assess the significance of the differences in proportion of fibrils that are in *Parallel* and *Oblique* regions by the treatment group, we employed a logistic regression model using generalized estimating equations (GEEs),[13] with correlations between any two pairs of observations within the same animal being constant, estimated from the data. The proportion of each type of fibril was compared for each treatment versus sham using a binary outcome, Y_{ij}, where $Y_{ij} = 1$ if the fibril was in a given microenvironment (that is, *Parallel* or *Oblique*) and $Y_{ij} = 0$ if the fibril was not, with a logit link function. All s.e.'s were computed using the robust Huber-White estimates. The GEE model that was employed is shown below:

$$\mathrm{log}it(p_{\mathrm{ij}}) = \log\left(\frac{p_{\mathrm{ij}}}{1-p_{\mathrm{ij}}}\right) = \beta_0 + \sum_{t=1}^{T-1} \beta_t \,\mathrm{Treatment}_t$$

where p_{ij} = probability ($Y_{ij} = 1$) for fibril I in animal j, β_0 is the intercept, and β_t fits the effect of treatment *t*, *t* = 1 to *T*, with treatment *T* being the reference category.

Post hoc comparisons of collagen fibril orientations were then carried out between treatment groups, using a Bonferroni correction for multiple comparisons with statistical significance assigned for *P*-values below 0.05.

Compared to Sham, the OVX-treated animals in Data Set I had a 17% decrease (*P*-value = 0.0045) in the proportion of fibrils occurring in *Parallel* structures and an 18% increase (*P*-value = 0.0026) in the proportion of fibrils occurring in *Oblique* structures. ALN treatment was previously observed to function as an antiresorptive leading to a BMD higher than that in the vehicle-treated group.[12] In this study, ALN treatment resulted in a frequency of collagen fibril observations intermediate between Sham and OVX values, although the differences in proportions of fibrils in *Parallel* and *Oblique* regions in these treatments were not significant. The bone resorption inhibitor CatKI also gave intermediate values for the frequency of collagen fibril observations and showed even less shift from the initial Sham values, with none of the comparisons versus other treatments being significant. Statistically, the changes in proportion of fibrils in *Parallel* and *Oblique* regions for the drug-treated sample were not significantly different from the Sham samples. *These data indicate that the drugs prevent the OVX-induced change in collagen*

microstructure in addition to their traditionally understood roles of preventing decreases in BMD. For the OVX treatment in Data Set II, an 18% decrease (*P*-value 0.0188) was observed in the proportion of fibril occurrence in *Parallel* structures and a 20% increase (*P*-value 0.0048) was observed in the proportion of fibril occurrence in *Oblique* structures compared with Sham. ERT treatment resulted in a partial prevention of change in the collagen microstructure, although the difference in ERT versus Sham in proportion of *Parallel* region fibrils was not significant (*P*=0.0961), whereas the difference in the proportion of *Oblique* fibrils was significant (0.0185). The magnitude of observed changes was similar to ALN treatment and less effective compared with CatKI treatment in preventing microstructure change. Analysis of the D-spacing variation for all seven treatments showed a range of values between ~58 and 70 nm, consistent with previous observations of D-spacing distribution.[6,8,14] However, no shift of the D-spacing values was observed for these samples, unlike the previous comparison for Sham and OVX sheep samples (**Figure A.3**).[8,9]

Treatment		No. of fibrils	No. of animals	Frequency in *Parallel* Microstructures (%, s.e.)	Frequency in *Oblique* Microstructures (%, s.e.)	Microstructure Frequency Difference
Data Set I	Sham	825	11	52 (5)	45 (5)	7 (10)
	OVX	808	12	35 (5)	63 (5)	-28 (10)
	ALN	971	12	40 (5)	57 (5)	-17 (10)
	CatKI	1001	13	47 (5)	49 (5)	-2 (10)
Data Set II	Sham	579	12	53 (5)	42 (5)	11 (10)
	OVX	728	12	35 (5)	62 (5)	-27 (10)
	ERT	761	12	41 (4)	58 (4)	-17 (10)

Table 2.1 Frequency of Type I collagen fibrils observed in *Parallel* and *Oblique* microstructures

2.3 Discussion

OVX is a common model used to study the effects of estrogen depletion.[8,9,15–17] Pennypacker *et al.*[12] applied the OVX model to study osteopenia in rabbits using the samples described herein and demonstrated osteoclastic bone resorption resulting from estrogen depletion. On the basis of the strong positive correlations between the experimental strength parameters and the tissue bone mineral content from animals from the same study, it was demonstrated that there were no obvious treatment-related changes in the material properties of vertebrae and femurs in

the OVX rabbits treated with odanacatib or ALN for 27 weeks. Here, we directly examined the effects of estrogen deficiency and two different bone resorption inhibitors at the microfibril structure level and observed changes in the relative frequency of fibril occurrence in local *Parallel* and *Oblique* microstructures. The link between increased resorption and the changes reported here to Type I collagen fibril microstructure remains unknown; however, related studies in the literature provide clues to possible mechanisms. In the mouse model, OVX reduces proteoglycan levels.[11] Furthermore, biglycan and decorin knockout mice have abnormal collagen fibril morphologies.[12] We hypothesize that reduced proteoglycan levels perturb the interactions between adjacent fibrils, resulting in a change to the microstructure. Cathepsin-K, a collagenase secreted by osteoclasts, cleaves proteoglycans from the fibril exterior before degrading the primary fibril structure.[18] OVX results in increased osteoclast activity coupled to increased cathepsin-K activity. This is directly countered by ERT therapy resulting in partial prevention of the collagen fibril microstructure changes. Strikingly, application of CatKI, which can prevent proteoglycan cleavage directly at the level of enzyme activity, gives almost complete prevention of fibril microstructure change. By way of contrast, treatment with a bisphosphonate is known to induce a change to osteoclast cell morphology and eventual cell death.[19] Thus, ALN reduces the amount of bone resorption, but also indirectly lowers the activity of cathepsin-K enzyme, which is consistent with observation that ALN treatment partially prevents changes to Type I collagen microstructure. Recently, Reznikov *et al.*[20] reported that the human lamellar bone consists of two different materials that differ substantially in terms of collagen fibril order. The connection between our fibril-level local organization classification (*Parallel* versus *Oblique*) and their observation of 'ordered' and 'disordered' materials is not clear at this time; however, changes in the relative quantities of the 'ordered' and the 'disordered' materials as a function of estrogen depletion and drug treatment are also a possible explanation of our data. These changes could also be related to the impacts of proteoglycan levels as discussed above.

In summary, a quantitative analysis of Type I collagen fibril organization indicates a significant decrease in fibrils appearing in *Parallel* structures such as bundles and sheets (18%) and a concomitant increase in fibrils appearing in *Oblique* structures, on OVX treatment of 6- and 9-month old rabbits. ALN and ERT drug treatments partially prevent the microstructure changes (12% decrease in *Parallel* structures), and CatKI treatment almost completely prevents the structural change (5% decrease in *Parallel* structures). The change in Type I collagen

microstructure induced by OVX is a previously unrecognized aspect of the impact of estrogen depletion on bone quality. In addition, the amelioration of these microstructure changes is a previously unrecognized mechanism of drug activity.

2.4 Materials and Methods

All rabbit femur samples were obtained from Merck Research Laboratory, West Point, PA, USA, and treatment of these animals was previously described in detail.[12] Sample preparation and the AFM imaging methods employed in this work have also been described in detail.[6] All imaging was carried out in air using a PicoPlus 5500 AFM (Agilent, Santa Clara, CA, USA) employing tapping mode with VistaProbes T300R probes (NanoScience, Phoenix, AZ, USA; nominal radius 10nm, force constant 40 N/m, resonance frequency 300 kHz). Line scan rates were set at 2 Hz or lower at 512 lines per frame. Image analysis and measurements were performed using the SPIP software (Image Metrology, Horsholm, Denmark).

2.5 Conflict of Interest

LTD and BLP work for Merck Inc. The remaining authors declare no conflict of interest.

2.6 Acknowledgements

This work was supported in part by an IISP grant from Merck Inc. to MMBH. We thank MD Morris and CM Les for many fruitful discussions on the impact of estrogen depletion and bisphosphonate treatment on bone. We thank HG Bone for fruitful discussions including suggesting the CatKI experiment, bringing to the attention of the UM group the unpublished Sham, OVX, CatKI, ALN and ERT studies of Pennypacker *et al.* and introducing the UM group to the Bone Biology group at Merck Inc.

2.7 References

1. Johnell, O. & Kanis, J. A. An estimate of the worldwide prevalence, mortality and disability associated with hip fracture. *Osteoporos. Int.* **15,** 897–902 (2004).
2. Viguet-Carrin, S., Garnero, P. & Delmas, P. D. The role of collagen in bone strength. *Osteoporos. Int.* **17,** 319–336 (2006).
3. Burr, D. B. The contribution of the organic matrix to bone's material properties. *Bone* **31,**

8–11 (2002).

4. Cranney, A. *et al.* IX: Summary of meta-analyses of therapies for postmenopausal osteoporosis. *Endocr. Rev.* **23,** 570–578 (2002).
5. Sornay-Rendu, E. & Delmas, P. D. Advances in osteoporosis diagnosis: the use of clinical risk factors. *Medicographia* **30,** 350–3698 (2008).
6. Erickson, B. *et al.* Nanoscale structure of type I collagen fibrils: Quantitative measurement of D-spacing. *Biotechnol. J.* **8,** 117–126 (2013).
7. Fang, M. *et al.* Type i collagen D-spacing in fibril bundles of dermis, tendon, and bone: Bridging between nano- and micro-level tissue hierarchy. *ACS Nano* **6,** 9503–9514 (2012).
8. Wallace, J. M., Erickson, B., Les, C. M., Orr, B. G. & Banaszak Holl, M. M. Distribution of type I collagen morphologies in bone: Relation to estrogen depletion. *Bone* **46,** 1349–1354 (2010).
9. Fang, M. *et al.* Estrogen depletion results in nanoscale morphology changes in dermal collagen. *J. Invest. Dermatol.* **132,** 1791–7 (2012).
10. Fang, M. & Holl, M. M. B. Variation in type I collagen fibril nanomorphology: the significance and origin. *Bonekey Rep.* **2,** 394 (2013).
11. Kafantari, H., Kounadi, E., Fatouros, M., Milonakis, M. & Tzaphlidou, M. Structural alterations in rat skin and bone collagen fibrils induced by ovariectomy. *Bone* **26,** 349–353 (2000).
12. Pennypacker, B. L. *et al.* Cathepsin K inhibitors prevent bone loss in estrogen-deficient rabbits. *J. Bone Miner. Res.* **26,** 252–262 (2011).
13. Diggle, P., Heagerty, P., Liang, K.-Y. & Zeger, S. *Analysis of Longitudinal Data*. (Oxford University Press, 2002).
14. Wallace, J. M. *et al.* Type i collagen exists as a distribution of nanoscale morphologies in teeth, bones, and tendons. *Langmuir* **26,** 7349–7354 (2010).
15. Frost, H. M. & Jee, W. S. S. On the rat model of human osteopenias and osteoporoses. *Bone Miner.* **18,** 227–236 (1992).
16. Kalu, D. N. The ovariectomized rat model of postmenopausal bone loss. *Bone Miner.* **15,** 175–191 (1991).
17. Smith, S. Y., Jolette, J. & Turner, C. H. Skeletal health: Primate model of postmenopausal osteoporosis. *Am. J. Primatol.* **71,** 752–765 (2009).

18. Panwar, P. *et al.* Effects of cysteine proteases on the structural and mechanical properties of collagen fibers. *J. Biol. Chem.* **288,** 5940–5950 (2013).
19. Rogers, M. J., Crockett, J. C., Coxon, F. P. & Mönkkönen, J. Biochemical and molecular mechanisms of action of bisphosphonates. *Bone* **49,** 34–41 (2011).
20. Reznikov, N., Shahar, R. & Weiner, S. Three-dimensional structure of human lamellar bone: The presence of two different materials and new insights into the hierarchical organization. *Bone* **59,** 93–104 (2014).

Chapter 3.

Estrogen depletion and drug treatment alters the microstructure of type I collagen in bone

In collaboration with Matt Muckley, Dr. Ming Fang, Prof. Jeffrey A. Fessler, Dr. Kathleen Welch, Prof. Edward D. Rothman, Prof. Bradford G. Orr, Dr. Le T. Duong, and Prof. Mark M. Banaszak Holl

3.1 Introduction

Reduction of estrogen levels is known to negatively impact bone quality and increase the likelihood of fracture for over 75 million people worldwide including 54 million people and 1.5 million fractures per year in the United States.[1–4] The widespread prevalence of Osteoporosis induced by the estrogen reduction in postmenopausal women has spurred a search for quantitative measures that can serve to probe the changes in bone structure and predict fracture. Bone mineral density (BMD) measurements have proven useful as a primary assay but are only indirectly sensitive to changes in collagen matrix structure and have limited predictive ability for bone fracture.[5] For these reasons, analytical tools that can assess changes in the collagen matrix as a function of estrogen reduction and drug treatment are highly desired.[6,7]

In our previous work, we characterized the effect of ovariectomy-induced estrogen depletion (OVX) and long-term treatment with alendronate (ALN), a cathepsin-K inhibitor L-006235 (CatKI), and 17β-estradiol (ERT) administered in prevention-mode on collagen fibril organization in rabbit cortical bone by classification of fibrils as existing in *Parallel* regions (bundles and sheets) or *Oblique* regions.[8] When analyzed by this method, OVX treatment resulted in a decrease in the percentage of collagen fibrils in the *Parallel* orientation. This microstructural change was partially prevented by treatment with ALN and fully prevented by treatment with CatKI. We now extend the *Parallel*/*Oblique* analysis to rabbit trabecular bone and introduce a new, fully automated method to characterize an image-level fibril alignment parameter (FAP) for

type I collagen fibrils in cortical femur and trabecular lumbar vertebrae. The addition of trabecular bone is important to this study because it is remodeled faster than cortical bone and changes in bone mass due to estrogen reduction are more pronounced. For this reason, many studies focus on the trabecular bone as a key metric for developing biological and structural understanding of osteoporosis.[9]

In this study, we first focus on a comparison of the collagen fibril structure between the cortical and trabecular bone and then extend the comparison to include OVX, OVX + ALN, and OVX + CatKI treatments. Surgical ovariectomy (OVX) is a common model used to induce estrogen depletion.[10–14] ALN is an orally available bisphosphonate developed by Merck and marketed as Fosamax. Although the bisphosphonates are effective in the clinic, similar to other potent antiresorptives, long term therapy have been associated with the increased incidences of several rare conditions including osteonecrosis of the jawbone and atypical fractures of the femur.[1,15–17] Bisphosphonates work by binding to bone mineral and then inducing apoptosis after being taken in by osteoclasts.[18] This mechanism of action is problematic because eliminating osteoclasts alters cell signaling between osteoclasts and osteoblasts that is critical to maintaining bone mass homeostasis. Recently, Merck Research Laboratories has developed a novel cathepsin K inhibitor (odanacatib) that inhibits cathepsin K, a collagenase secreted by osteoclasts, without killing the cell.[9] This drug is effective because cathepsin K is the primary collagenase in bone and plays an important role in osteoclast mediated bone resorption.[19] The animal model used in this study consists of 9 month old female New Zealand white rabbits chosen because of their similarities to humans with respect to the cathepsin K enzyme and Haversian remodeling in cortical bone.[8,9] The treatment groups included Sham-operated + vehicle (n = 11), OVX + vehicle (n = 12), OVX + alendronate (ALN, 600 µg/kg/wk, s.c.) (n = 12) and OVX + L-235 (CatKI, 10 mg/kg, daily, p.o.) (n = 13) in prevention mode for 27 weeks. Note, L-006235 (L-235) is structurally related and displays similar potency and selectivity as odanacatib in preclinical models of osteoporosis.[9]

We have imaged both cortical femur and trabecular lumbar vertebrae rabbit bone using atomic force microscopy (AFM). The image sets were analyzed using two approaches. First, individual fibrils with a measurable D-spacing in the images were coded as being present in local *Parallel* or *Oblique* arrangements using the method described previously.[8] For the first time, we have extended the imaging and the *Parallel*/*Oblique* analysis to trabecular bone with OVX and

drug treatments. This analysis approach relies on hand coding of the images, is very time consuming, omits fibrils without a measurable D-spacing, and is limited to the approximation of assigning fibrils with just two classifications. An automated image analysis that could function at the level of the entire image and provide a continuous variable characterizing the extent of fibril organization was highly desired. To achieve this goal, we developed a second analysis approach that employs autocorrelation of image patches to compute a vector field that approximates fibril alignment. We then used that vector field to generate a fibril alignment parameter (FAP) based on an information-theoretic entropy calculation for each image as well as to form maps indicating the spatial alignment within a given image. We applied this approach to both the cortical and trabecular sample sets.

Comparing the cortical to trabecular collagen structure, the frequency of fibrils in the *Parallel* microstructure decreased and the frequency of *Oblique* microstructures increased. The cortical and trabecular bone resulted in the same average FAP value; however, the distribution of FAP values derived from the individual regions contained more high FAP values (low alignment) for the trabecular case and low FAP value (high alignment) for the cortical case. Both observations are consistent with our qualitative assessment of the relative amount of fibril alignment observed for the two bone types. Treatment with ALN resulted in a shift towards lower FAP values for cortical bone and a partial prevention of the increase in the frequency of *Oblique* fibrils; however, for trabecular bone higher FAP values were obtained coupled to an increase in the frequency of *Parallel* coded microstructure. Treatment with CatKI resulted in a shift towards higher FAP values for cortical bone, with no change in the *Parallel*/*Oblique* frequencies, and no change in FAP values for trabecular bone although the frequency of *Parallel* coded microstructure increased similar to the ALN treatment. In summary, both image analysis approaches indicate: 1) cortical collagen and trabecular collagen alignment differs significantly; 2) OVX and drug treatment can impact the alignment of the collagen fibrils in both cortical and trabecular bone; 3) the impact of OVX, OVX + ALN, and OVX + CatKI treatment on collagen fibril alignment differs between the cortical and trabecular bone.

3.2 Methods

3.2.1 Bone Preparation and AFM Imaging

All samples were obtained from Merck Research laboratories and stored in 95% ethanol.[8,9] Rabbit cortical femur images analyzed were from our previously published data set.[8] There were a total of 663 images (3.5 μm^2) for cortical femur samples taken from 48 animals (11 Sham, 12 OVX, 12 OVX + ALN, and 13 OVX + CatKI). Trabecular bone from the lumbar vertebrae of the same animals was added to the current study. All images were obtained blind to treatment type. AFM imaging of the lumbar trabecular samples was quite challenging due to the heterogeneous organization of trabecular spicules and the fragility of the trabeculi. Methods development required an extended period and resulted in the loss of 1 Sham, 1 OVX, 0 ALN, and 1 CatKI samples from the data set. The final animal counts for the lumbar vertebrae are as follows: Sham + vehicle (n = 10), OVX (n = 11), OVX + ALN (n = 12), and OVX + CatKI (n = 12). The lumbar vertebrae samples were prepared by sectioning a region of the caudal end and mounting onto a steel AFM puck. Bone marrow was mechanically removed using forceps followed by polishing the sample on a wheel for 2-4 minutes using a 3-micron diamond suspension and sonication in nanopure water for five minutes to remove the polishing solution. The surface collagen was demineralized by shaking in 0.5 M EDTA pH = 8.0 for 30 minutes at room temperature. Sonication was repeated for five minutes prior to air drying before imaging in tapping mode. All imaging was performed in air at room temperature with a conical AFM probe (nanoScience Instruments; Aspire conical tapping mode AFM probes; 300 kHz, 40 N/m, radius 8 nm). Initial scans for trabecular lumbar vertebrae images where acquired using a 10 µm x 10 µm image area on a trabecular rod structure. A set of 3.5 µm x 3.5 µm images were acquired for each region with a total of 526 images (3.5 µm x 3.5 µm) available for the calculation of the fibril alignment parameters from the 45 animals. 2,187 and 3,605 fibrils were identified for D-spacing measurement and coding as being in a *Parallel* microstructure (bundle or sheet) or *Oblique* microstructure for the trabecular lumbar vertebrae and cortical femur, respectively.

3.2.2 Analysis of D-spacing

The D-periodic axial/gap overlap spacing (D-spacing) was measured for the blinded lumbar trabecular bone samples. A total of 511 fibrils were measured for Sham, 662 for OVX, 533 for OVX + ALN, and 654 for OVX + CatKI. Full details on the instrument calibration, controls for instrument thermal drift, and the use of 2D-Fourier transforms to accurately measure the fibril D-spacing have been previously published.[14,20,21] We note that thermal instrument drift, instrument

calibration and tilt angles in the D-spacing must be properly accounted for to obtain accurate distributions.[20,22]

3.2.3 *Parallel* and *Oblique* Fibril Classification

Each fibril was coded as either *Parallel* or *Oblique* to assess the local microstructure surrounding individual collagen fibrils. This hand-coding was performed while blinded to treatment group. The *Parallel/Oblique* classification has been presented in detail previously.[8] Briefly, fibrils were given the *parallel* classification if they existed in a bundle of 3-15 fibrils aligned in parallel with defined edges or in a sheet of > 20 parallel, aligned fibrils that are continuous with adjacent bone. An *Oblique* classification was given when fibrils were in a microstructure with a wide range of fibril-fibril angular dispersion. Topography and amplitude images were both used for making this classification. The results of this analysis for the cortical femur have been previously reported.[8] This fibril-by-fibril analysis was implemented for the trabecular lumbar vertebrae in the same way it was for the cortical femur.

3.2.4 Fibril Alignment Parameter (FAP) Calculation and Analysis

To quantitatively assess the degree of fibril alignment in the AFM images, we developed and employed an autocorrelation approach and an information-theoretic entropy metric to determine a fibril alignment parameter (FAP). The FAP provides reproducible and quantitative image-to-image and sample-to-sample comparisons of the collagen fibril alignment. This autocorrelation approach was developed after the sample blinding had been removed. Amplitude images were employed for this analysis since this image mode highlights D-spacing and fibril-to-fibril features as opposed to overall topographic slope. A high pass FFT-based filter with a square-shaped frequency response of width 8000 nm^{-1} (i.e., excluding frequencies below 0.004 nm^{-1}) was applied to the images to prevent artifacts in the autocorrelation resulting from local variation in the amplitude gray scale within an image. A patch size of 64 x 64 pixels (439 x 439 nm) was selected, corresponding to a region containing six to seven D-spacings along a fibril length and about six to seven fibrils in width. An array of patches across the 3500 x 3500 nm image was created by shifts of 4 pixels in the x and y directions. Each patch in the array was then correlated with neighboring patches. The analysis performed a restricted search to obtain the maximum autocorrelation from patches in a shift range between 7 and 14 pixel shifts (corresponding to 48

nm to 96 nm; this is within the ~60-70 nm range of the repeated structures present from D-spacing and individual fibril widths). Each patch orientation was represented by a vector that indicates the angle and magnitude of the highest neighboring patch correlation. The result of this process is illustrated by the quiver plot overlaid on the AFM image in Supplemental **Figure B.3 and B.4**.

We used the information theoretic entropy as a summary statistic of the patch alignment vectors. The information theoretic entropy is defined for a probability density function as follows (eq 1):

$$\varepsilon = -\sum_{j=1} p(x_j)\ln(p(x_j)) \quad (1)$$

where x_j represents a possible local alignment angle and $p(x_j)$ is the "probability" of that angle occurring. This parameter quantifies the degree of fibril alignment in the distribution. An empirical probability distribution was created based on the angles and lengths of the alignment vectors. The entropy of this empirical distribution yields a parameter that captures the extent of collagen fibril alignments due to the properties of the entropy function. For these entropy calculations, instead of using the exact empirical probability, we weighted the probability of an angle by the confidence in that alignment angle (eq. 2),

$$p(x_j) \approx \frac{K_j}{\sum_j K_j} \quad (2)$$

where K_j corresponds to the arrow scaling for the direction at location j. This is the FAP that is on a scale of 0 to 1 with 0 resulting from vectors that are completely aligned or parallel (angle of 0°) and 1 resulting from vectors with no dominant alignment. The approach has the advantage of also being able to quantify a full range of oblique angles from parallel to perpendicular. Heat maps were produced from the vector fields with areas of high fibril alignment shown in red and areas of low alignment shown in blue (**Figure B.5**, **B.6**, **B.7**, and **B.8**).

3.3 Results and Discussion

Trabecular bone in the vertebrae is a complex tissue composed of a bi-continuous network of mineralized collagen trabeculae interspersed with marrow.[25] Previous AFM studies on trabecular bone have noted the complexity of the woven collagen fibrils do not seem to match a simple twisted plywood model of fibril orientation and alignment.[26] AFM images of human osteoporotic trabecular bone from a fractured femoral head have been reported; however, the medication history of the individual is not known.[27] In order to gain a greater understanding of the

differences between the collagen structure in cortical and trabecular bone, and between normal tissue and tissue affected by OVX, OXV + ALN, and OVX + CatKI treatments, we have examined a group of 48 rabbits including sham-operated (Sham), ovariectomized (OVX), OVX + ALN, and OVX + CatKI treatments. Imaging the trabecular bone in the rabbit lumbar vertebrae was substantially more challenging than the imaging of the cortical femur bone. For the cortical femur region, the bone itself is robust and after polishing and demineralizing a large, continuous field of collagen is available for study. As illustrated in **Figure 3.1**, the center region of a lumbar vertebrae contains trabecular spicules separated by large gaps that had been filled with marrow. Imaging regions were selected on the trabeculae, which even after polishing remained rough on the micron scale as compared to similarly prepared cortical femur bone. Exemplar pictures of both the cortical femur and lumbar vertebrae are provided in **Figure B.1**. The following discussion of the changes in collagen fibril structure is organized in terms of increasing hierarchical structural scale. We first focus on changes in the D-spacing values within fibrils. The discussion then turns to a hand coded analysis of the local fibril organization for each of the fibrils assessed for its D-spacing value. Finally, we present a newly developed analysis were we quantify the fibril alignments in a 3.5 × 3.5 μm image field. Thus, our structural analysis starts on a ~50-100 nm scale, progresses to a ~70-700 nm scale, and ends assessing alignment over a 3,500 nm region.

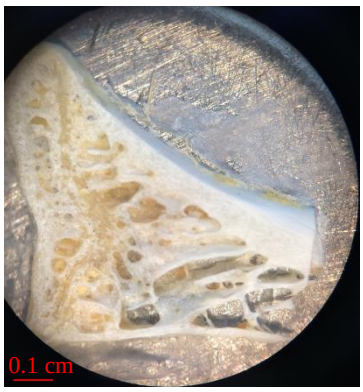

Figure 3.1 Optical image of rabbit lumbar vertebrae section. Images were obtained at the polished top face of the trabeculai.

3.3.1 Analysis of D-spacing Variation

The measurements of 2,187 trabecular lumbar vertebrae and 3,605 cortical femur fibril D-periodic axial/gap overlap spacing (D-spacing) values distributed across the Sham, OVX, OVX + ALN, and OVX + CatKI treatments are summarized in **Figure B.2**. Neither the average D-spacing values nor the distribution of the values revealed significant differences between Sham, OVX, OVX + ALN, and OVX + CatKI treatments for either the cortical femur sample[7] or the lumbar vertebrae data sets when considered as a whole.

In five-year-old Columbia-Rambouliet cross sheep, ovariectomy-induced estrogen depletion induces changes in type I collagen D-spacing distributions.[14] Wallace *et al.* concluded that OVX (3 animals; 182 fibrils) resulted in a decrease in the mean D-spacing and a shift in the overall D-spacing distribution towards lower values in ovine bone ($p < 0.001$) when compared to the Sham treatment group (3 animals; 168 fibrils).[14] As discussed, there are no changes observed in the overall D-spacing distributions for either the rabbit cortical or trabecular samples. The rabbits used in the current animal model are skeletally mature (rabbits reach skeletal maturity by eight months).[28] In addition, the rabbits were sacrificed 27 weeks after ovariectomy which is sufficient time to observe changes induced by estrogen depletion[9] In the ovine study, the animals used by Wallace *et al.*[14] were also skeletally mature and allowed to reach peak bone remodeling rates post-OVX. Markers for bone remodeling in sheep peak after 3-4 months.[29] It is not clear if the varying effects estrogen depletion are species dependent or if the changes observed by Wallace *et al*. in ovine bone would be minimized with a larger sample size. In cynomolgus monkeys, a sample size of 15-20 animals is required to provide statistical power when comparing Sham and OVX treatment groups.[13]

3.3.2 Analysis of Animal-to-Animal Variability in Bundle D-Spacing

We examined the distribution in D-spacing that exists for fibrils coded as existing in bundles only and in this way excluded the very disperse 50% or so of measurements arising from the more heterogeneous *Oblique* fibrils as well as fibrils coded as existing in a sheet microstructure (**Figure 3.2**). The D-spacing distribution for bundle collagen fibrils for the trabecular vertebrae of Sham animals is illustrated in **Figure 3.2a**. The average D-spacing value for the Sham animals is 65.9 nm (0.5, standard error) whereas the average value for the OXV, OVX + ALN, and OVX + CatKI animals is 65.4 nm (0.5), 64.9 nm (0.5), and 64.8 nm (0.5), respectively. While there were no significant differences among the means across treatments ($p = 0.4573$) there were significant differences in the degree of animal-to-animal variability across treatments ($p = 0.02$ by likelihood ratio test). Fitting a variance components model within each treatment, including a random effect for animal, there is zero variability estimated between animals in the Sham treatment. The OVX treatment exhibited a non-significant animal to animal variability in the D-spacing of trabecular fibrils coded as being in a bundle microstructure ($p = 0.074$; likelihood ratio chi-square test). Significant between animal variability was observed in both the OVX + ALN and OVX + CatKI

treatment groups ($p < 0.0001$ in each treatment). This analysis of bundle D-spacing was also performed for the cortical femurs, as shown in **Figure 3.3**. A likelihood ratio test for the equality of the variances showed that there were no significant differences in animal to animal variability across the four treatments for the cortical femurs ($p = 0.64$).

Treatment with ALN or CatKI introduced animal-to-animal variability in the bundle D-spacing values for trabecular bone and not cortical bone. The faster remodeling rate of trabecular bone is one possible source of this observed difference between the two types of bone.

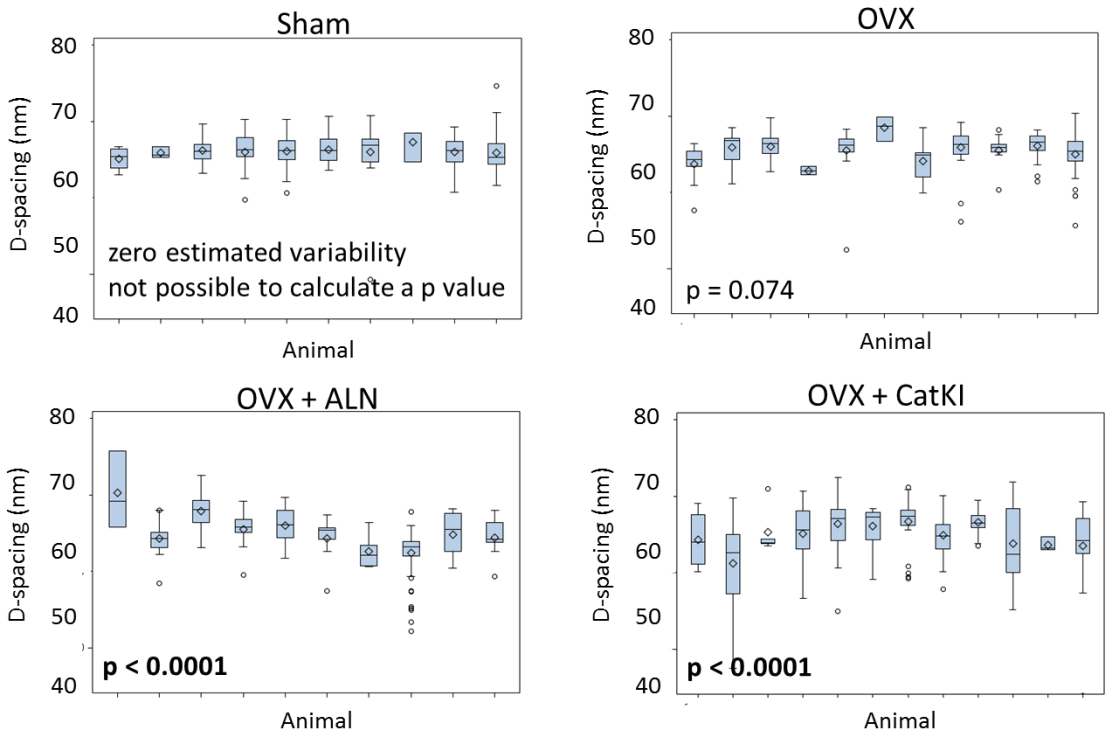

Figure 3.2 Boxplots of the D-spacing distribution of the collagen fibrils located in trabecular bundles obtained for Sham, OVX, OVX + ALN, and OVX + CatKI treatment groups. Both of the drug treatments introduced significant animal-to-animal variability in the bundle D-spacing ($p < 0.0001$ by likelihood ratio Chi square test). There were two ALN animals that did not contain any fibrils that were coded as being in a bundle. One of those two animals had both sheet and *Oblique* microstructures and the other animal only had *Oblique* microstructures.

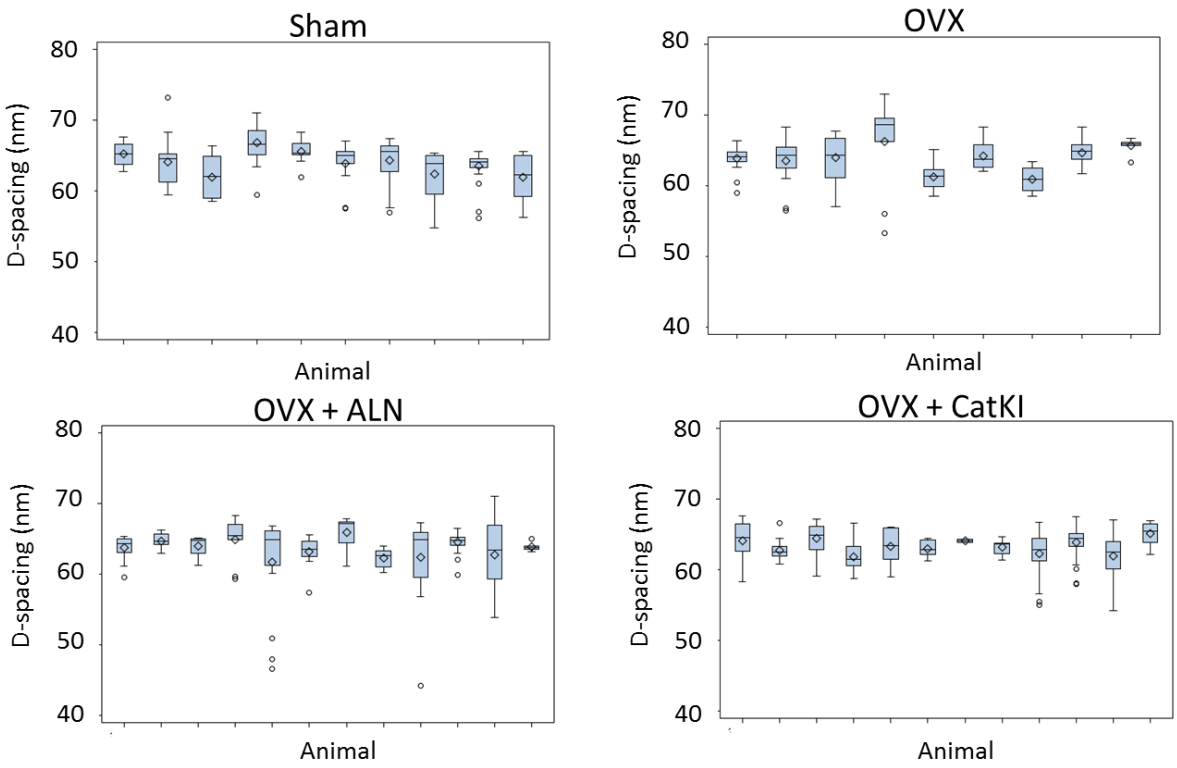

Figure 3.3 Boxplots of the D-spacing distribution of collagen fibrils located in cortical femur bundles obtained for Sham, OVX, OVX + ALN, and OVX + CatKI treatment groups. There were no significant differences in the animal-to-animal variability across the four treatment groups (p = 0.64, likelihood ratio test).

3.3.3 *Parallel* and *Oblique* Fibril Classification

All fibrils quantified in terms of D-spacing values were hand-coded as existing in either *Parallel* or *Oblique* microstructures. The percentage of *Oblique* or *Parallel* fibrils was examined using a Generalized Estimating Equation (GEE) approach[30] that takes into account the correlation among observations in the same animal (**Table 3.1**). As previously described,[8] the percentage of *Oblique* fibrils in rabbit cortical femur was estimated to be 18% greater in the OVX group than in the Sham group (p = 0.0026). However, the percentage of *Oblique* fibrils in rabbit trabecular lumbar vertebrae was 4% lower in the OVX group than in the Sham group and this difference was non-significant (p = 0.6415). The full statistical analysis is described in chapter 2.[8] All differences in the percentage of fibrils in a given microstructure for trabecular bone were non-significant (p >

0.05). The OVX + CatKI has 13% more fibrils coded as *parallel* than the Sham group and this was the largest difference observed in the trabecular bone (p = 0.1084).

Treatment		# of fibrils	# of animals	Frequency in Parallel Microstructures (%, std error)	Frequency in Oblique Microstructures (%, std error)
Cortical Femur	Sham	825	11	52 (5)	45 (5)
	OVX	808	12	35 (5)	63 (5)
	ALN	971	12	40 (5)	57 (5)
	CatKI	1001	13	47 (5)	49 (5)
Trabecular Lumbar Vertebrae	Sham	511	10	44 (7)	56 (7)
	OVX	662	11	47 (5)	52 (5)
	ALN	532	12	46 (6)	53 (6)
	CatKI	654	12	57 (5)	43 (5)

Table 3.1 Frequency of Type I Collagen Fibrils Observed in *Parallel* and *Oblique* Microstructures

We also compared the percentage of fibrils coded as *Parallel* in trabecular versus cortical bone within each treatment group using the GEE model described above. The cortical OVX group had a percentage of *Parallel* fibrils that was 12% lower than the trabecular OVX group and this difference was marginally significant (p = 0.0596). All other comparisons for the percentage of *Parallel* fibrils were non-significant (p > 0.05). The same comparisons for the percentage of *Oblique* fibrils were also non-significant (p > 0.05). All comparisons with their p-values can be found in **Tables 3.2** and **3.3.**

Comparison	p-value
Cortical Sham and Trabecular Sham	0.2971
Cortical OVX and Trabecular OVX	0.0596
Cortical OVX + ALN and Trabecular OVX + ALN	0.4684
Cortical OVX + CatKI and Trabecular OVX + CatKI	0.1315

Table 3.2 Comparisons of the percentage of fibrils coded as *Parallel* in cortical versus trabecular bone in each treatment group

Comparison	p-value
Cortical Sham and Trabecular Sham	0.1958
Cortical OVX and Trabecular OVX	0.9684
Cortical OVX + ALN and Trabecular OVX + ALN	0.7866
Cortical OVX + CatKI and Trabecular OVX + CatKI	0.8118

Table 3.3 Comparisons of the percentage of fibrils coded as *oblique* in cortical versus trabecular bone in each treatment group

3.3.4 Fibril alignment parameter analysis of AFM images from cortical femur and trabecular lumbar bone

Our previous observations that OVX and drug treatment impact collagen structure in bone,[8] and that the dispersion of D-spacing values was affected by the collagen packing microstructure,[23] drove our interest in developing quantitative approaches to the analysis of the fibril packing on a multi-micron scale. The new approach presented here has the advantages of being fully automated, avoiding the tedious nature of the blinded hand coding, and generates average alignment parameter values that vary continuously from 0 (fibrils aligned in parallel) to 1 (fibrils exhibit no dominant alignment) for each image. This quantitative output allows ready comparison of images both within and between sample sets.

Fibril alignment parameter (FAP) calculations were performed for a total of 663 images (3.5 μm^2) for cortical femur samples and 526 images (3.5 μm^2) for trabecular lumbar vertebrae samples across 48 animals. The average FAP values for sham femur and sham lumbar vertebrae were the same (0.9 ± 0.1); however, the distributions of the FAPs differed with the cortical femur

having more images in the 0.4 to 0.8 parameter range (more alignment) and fewer images in the 0.9 to 1.0 range (less alignment) (**Figure 3.4**). The histograms are not Gaussian distributions and were plotted as cumulative density functions to perform statistical comparisons. Exemplar images are provided in **Figure 3.4b** along with the CDF to illustrate how changes in image-level fibril alignment correspond to the changes in FAP. A Kolmogorov-Smirnov (K-S) test indicated the cortical and trabecular distributions for Sham tissue were significantly different (p = 0.000).

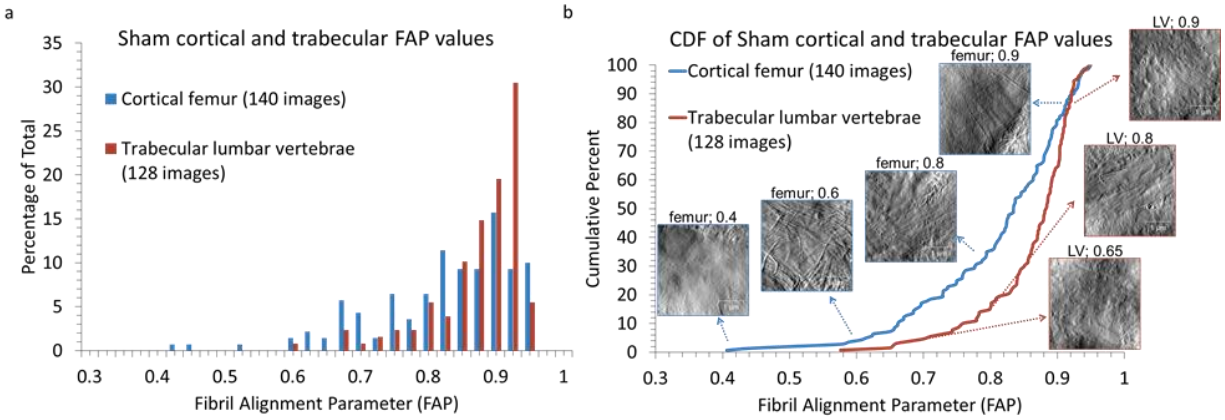

Figure 3.4 Distribution of FAP values in cortical and trabecular bone. a) The sham cortical femurs and trabecular lumbar vertebrae exhibit a non-Gaussian distribution of FAP values with an average value of 0.8 ± 0.1. b) Cumulative density functions of FAP values for Sham cortical femurs and trabecular lumbar vertebrae. The sham lumbar vertebrae were shifted towards higher FAP values (less collagen alignment) with statistical significance (p = 0.000).

3.3.5 Effect of OVX on FAP distributions in cortical femur and trabecular lumbar bone

OVX and Sham animals showed no difference in their average FAP (0.8 ± 0.1) or distribution of values (p = 0.481 for cortical femur; p = 0.067 for trabecular vertebrae) (**Figures 3.5a** and **3.5b**). Although Sham cortical and Sham trabecular bone exhibit significantly different FAP distributions (p = 0.000), under OVX treatment the lumbar vertebrae FAP distribution moves toward that of the OVX cortical femur distribution and the two CDFs are no longer statistically different (p = 0.153) (**Figure 3.6a**). In other words, for the case of cortical femur bone, the OVX CDF distribution does not differ from Sham (p = 0.481); however, the lumbar trabecular FAP distribution for OVX treatment is no longer significantly different from that for OVX cortical bone (p = 0.153). Recall that the comparison between OVX and Sham animals did show a statistically

significant difference in microstructure when considering the classification into *Parallel* and *Oblique* structures (**Table 3.1**).[8] The FAP values for the lumbar trabecular bone were 0.9 ± 0.1 for Sham and 0.8 ± 0.1 for OVX. The distribution of OVX values shifted slightly to higher alignment; however, the shift is not significant as assessed by the K-S statistic (p = 0.067) (**Figure 3.5b**).

3.3.6 Effects of ALN and CatKI Drug Treatments on FAP distributions in cortical femur and trabecular lumbar bone

Drug treatments did not change the average FAP values of 0.8 ± 0.1 and 0.9 ± 0.1, respectively, for the cortical femur and trabecular lumbar bone, but they did affect the distributions (**Figure 3.5**). For the cortical femur data set, OVX + ALN treatment resulted in a significant increase in the number of regions of parallel alignment (decrease in FAP) as compared to OVX (p = 0.012). Treatment with OVX + CatKI resulted in a significant decrease in the number of regions of parallel alignment (increase in FAP) as compared to Sham (p = 0.007) and OVX + ALN (p = 0.000) but not to OVX (p = 0.078). For the lumbar vertebrae data, the OVX + ALN treatment resulted in a significant decrease in the numbers of regions of parallel alignment (increase in FAP) as compared to OVX (p = 0.000). It is notable that the shift direction is opposite direction than that observed for cortical bone. Treatment with OVX + CatKI also resulted in a significant decrease in the numbers of regions of parallel alignment (increase in FAP) as compared to OVX (p = 0.010).

The change in FAP distribution as a function of bone type and drug treatment is summarized in **Figure 3.5c**. For any given treatment, the change in FAP distribution relative to Sham is different for cortical and trabecular bone. One possible origin for this difference is the faster remodeling rate of trabecular bone relative to cortical bone. This difference in remodeling rate could alter the relative amounts of aligned/unaligned collagen and this would produce a difference FAP value distribution. When considering only one type of bone at a time (cortical or trabecular), the drug treatment (ALN or CatKI) induces a different change in the FAP distribution relative to Sham. ALN and CatKI have different mechanisms of action that could potentially explain these differences. ALN binds to bone mineral and is taken into the osteoclast during bone resorption and induces apoptosis of the osteoclast.[18] In contrast, CatKI inhibits cathepsin K, the primary collagenase responsible for osteoclast-mediated bone resorption, and bone resorption is prevented without a decrease in bone formation.[9]

a

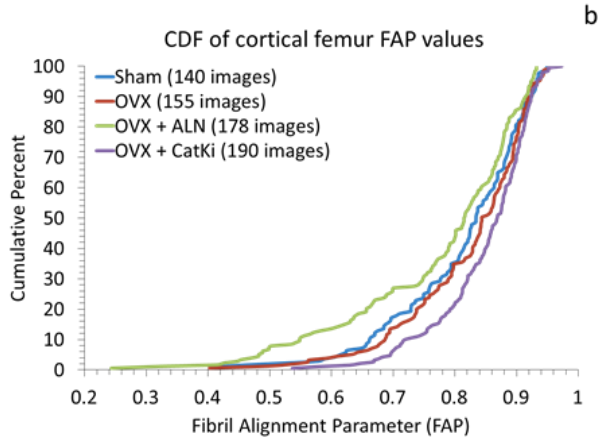

b

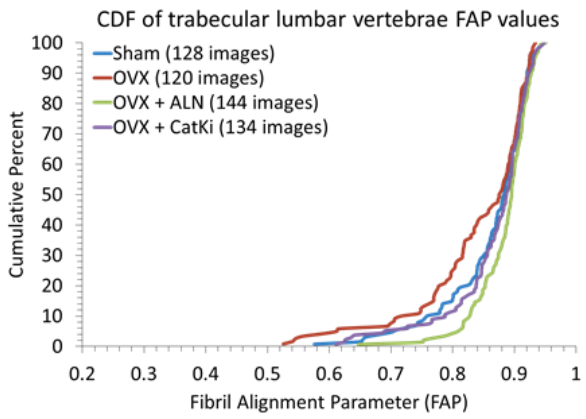

c

	Cortical femur	Trabecular lumbar vertebrae
OVX	no change in FAP	shift FAP to lower values
OVX + ALN	shift FAP to lower values	shift FAP to higher values
OVX + CatKI	shift FAP to higher values	no change in FAP

Figure 3.5 Distribution of FAP values for Sham, OVX, and drug treated bone in cortical femur (a) and trabecular lumbar vertebrae (b). All eight groups had the same average FAP value (0.8 ± 0.1 for cortical Sham, cortical OVX, cortical OVX + ALN, and trabecular OVX and 0.9 ± 0.1 for cortical OVX + CatKI, trabecular Sham, trabecular OVX + ALN, and trabecular OVX + CatKI). (a) For cortical bone, the distribution of FAP values did not change after ovariectomy ($p = 0.481$). In comparison to Sham, drug treatment after ovariectomy resulted in a shift towards more order ($p = 0.201$) with ALN treatment and more disorder (0.007) with CatKI treatment. (b) In comparison to Sham, the distribution of FAP values for OVX is shifted towards more order ($p = 0.067$), treatment with alendronate shifts towards more disorder ($p = 0.054$), and treatment with CatKI has little effect ($p = 0.889$). (c) A summary of these changes in comparison to Sham.

3.3.7 Summary of FAP distribution observations

Sham animals have significantly different FAP distributions for cortical and trabecular bone with cortical femur having lower FAP values (more aligned) and trabecular lumbar vertebrae having higher FAP values (less aligned). OVX treatment shifts the trabecular distribution towards lower FAP values and the cortical and trabecular distributions are no longer significantly different from one another. Treatment with ALN following ovariectomy impacts both cortical and trabecular bone with cortical bone shifting towards lower FAP values and trabecular bone shifting towards higher FAP values. Treatment with CatKI only impacts cortical bone and shifts the distribution towards the trabecular distribution with higher FAP values.

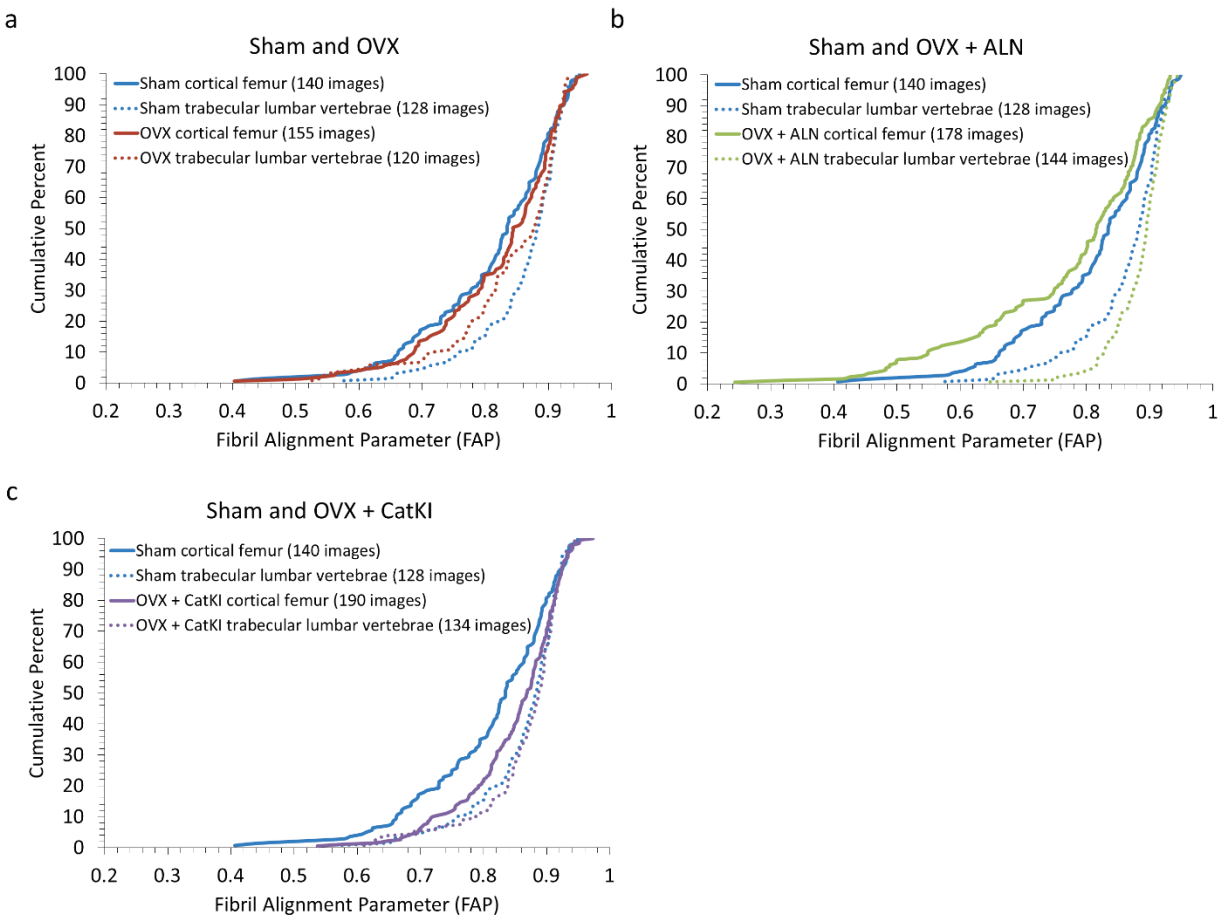

Figure 3.6 Cumulative density function of FAP values for estrogen depleted and drug treated animals in data sets I and III. Ovariectomy resulted in no change to the FAP distribution for cortical bone (0.481) and a shift towards lower FAP (more order) in the trabecular bone ($p = 0.067$). Treatment with alendronate resulted in the trabecular bone becoming less aligned ($p = 0.054$) and the cortical bone becoming more ordered ($p = 0.201$). In contrast, treatment with CatKI did not alter the extent of order/disorder for trabecular bone ($p = 0.889$) but did shift the cortical bone towards more disorder ($p = 0.007$). When comparing the distributions between femur and lumbar vertebrae within a treatment group, OVX is the only group that does not have a significant difference (Sham, $p = 0.000$; OVX, $p = 0.153$; OVX + ALN, $p = 0.000$; OVX + CatKI, $p = 0.016$).

3.3.8 Relationship between FAP distributions and BMD

The bone mineral density (BMD) data for trabecular lumbar vertebrae samples in this animal study is published in Pennypacker et al. and a summary of the results are shown in **Figure**

3.7.[9] The Sham and OVX + drug treatment samples all have the same BMD within error. The estrogen depleted animals had a statistically significant lower BMD, as expected.

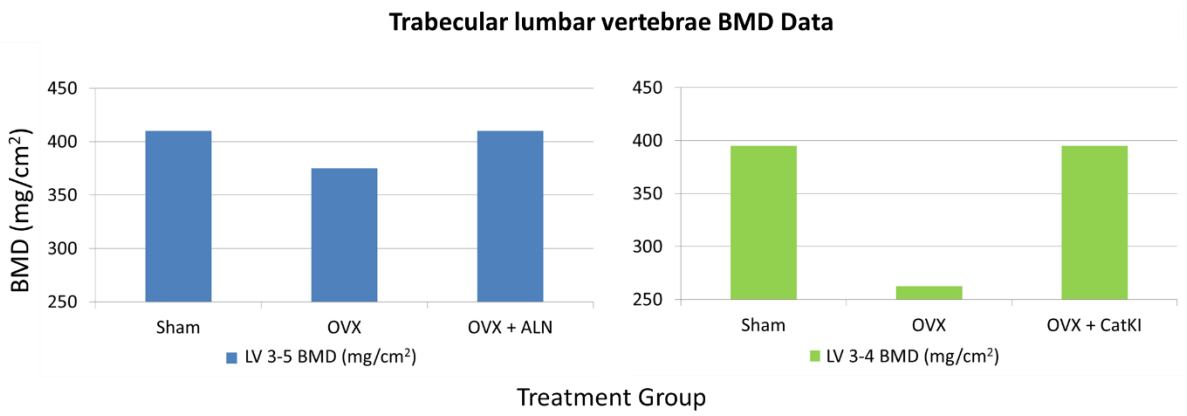

Figure 3.7 Bone mineral density (BMD) for LV 3-5 (blue) and LV 3-4 (green). OVX rabbits had a significantly lower BMD compared with Sham ($p < 0.01$ for LV 3-5, $p < 0.05$ for LV3-4). Treatment with OVX + ALN and OVX + CatKI fully prevented BMD loss ($p < 0.01$). Data adapted from Pennypacker et al. 2011.

The lumbar vertebrae samples imaged for the AFM analysis used lumbar vertebrae 4. Recall that the distributions of FAP values in trabecular bone showed a marginally significant shift towards lower values ($p=0.067$), or more alignment, under the OVX treatment condition (**Figure 3.6a**). Under the OVX + CatKI treatment condition, both BMD and FAP values ($p=0.889$) do not differ from Sham. Interestingly, under the OVX + ALN treatment condition (Figure 3.6b), the BMD did not differ from Sham but the FAP values exhibited an increase (less alignment) that was marginally significant ($p = 0.054$). Additional work is needed to understand how these changes in BMD and FAP relate to bone quality and mechanical properties.

3.3.9 Relationship of D-spacing, parallel/oblique coding, and FAP to biological mechanism and structure.

An important biological action of estrogen in bone is to induce apoptosis of osteoclasts.[31,32] Estrogen depletion leads to the prolonged life of those cells and increased bone resorption. Increased bone formation simultaneously develops and an overall high-turnover state develops which leads to changes in bone quality and/or bone loss. Estrogen depletion led to changes in the distribution of FAP values for trabecular lumbar vertebrae but not cortical femur. Although the

mechanism for this change is unknown, it could be related to the differences in estrogen receptors (ER). Trabecular bone primarily has the ERβ isoform and cortical bone primarily has the ERα isoform. If estrogen signaling for apoptosis is selective for one isoform over the other, then this could potentially explain the FAP changes observed. In addition, treatment with ALN after OVX resulted in changes to the FAP values for both cortical and trabecular bone. ALN does not use the estrogen receptor to kill the osteoclast so it makes sense that ALN is altering both cortical and trabecular bone.

3.4 Conclusions

As expected, trabecular lumbar vertebrae had less aligned collagen than cortical femur in the Sham animals. The fibril alignment parameter applied to the AFM data in this study showed that ovariectomy induced estrogen depletion results in trabecular lumbar vertebrae and cortical femur having the same degree of alignment. Furthermore, drug treatments impact cortical femur and trabecular lumbar vertebrae differently. OVX followed by treatment with alendronate resulted in a change in the order for both cortical femur and trabecular lumbar vertebrae. The cortical femur became more aligned and the trabecular lumbar vertebrae became more less aligned. In contrast, treatment with the cathepsin K inhibitor prevented changes in the distribution of alignment in trabecular lumbar vertebrae from occurring. The cortical femur, however, was shifted towards less alignment.

Ovariectomy induced estrogen depletion alters microstructure at different hierarchical levels for cortical and trabecular bone in rabbits. In rabbit cortical femur, OVX altered microstructure at the individual fibril level. In trabecular lumbar vertebrae, OVX altered microstructure at a scale that is relevant at the micron level, as evidenced by the change in FAP value distribution. In order to effectively treat post-menopausal osteoporosis, it will be important for drug treatments to target the appropriate level of hierarchical structure being affected by the disease.

3.5 References

1. Black, D. M. & Rosen, C. Postmenopausal Osteoporosis. *N. Engl. J. Med.* **374,** 254–262 (2016).
2. Johnell, O. & Kanis, J. A. An estimate of the worldwide prevalence, mortality and disability

associated with hip fracture. *Osteoporos. Int.* **15,** 897–902 (2004).

3. Viguet-Carrin, S., Garnero, P. & Delmas, P. D. The role of collagen in bone strength. *Osteoporos. Int.* **17,** 319–336 (2006).
4. Wright, N. C. *et al.* The recent prevalence of osteoporosis and low bone mass in the united states based on bone mineral density at the femoral neck or lumbar spine. *J. Bone Miner. Res.* **29,** 2520–2526 (2014).
5. Burr, D. B. The contribution of the organic matrix to bone's material properties. *Bone* **31,** 8–11 (2002).
6. Fang, M. & Holl, M. M. B. Variation in type I collagen fibril nanomorphology: the significance and origin. *Bonekey Rep.* **2,** 394 (2013).
7. Wallace, J. M. Applications of atomic force microscopy for the assessment of nanoscale morphological and mechanical properties of bone. *Bone* **50,** 420–427 (2012).
8. Cauble, M. A. *et al.* Alteration of Type I collagen microstructure induced by estrogen depletion can be prevented with drug treatment. *Bonekey Rep.* **4,** 697 (2015).
9. Pennypacker, B. L. *et al.* Cathepsin K inhibitors prevent bone loss in estrogen-deficient rabbits. *J. Bone Miner. Res.* **26,** 252–262 (2011).
10. Fang, M. *et al.* Estrogen depletion results in nanoscale morphology changes in dermal collagen. *J. Invest. Dermatol.* **132,** 1791–7 (2012).
11. Frost, H. M. & Jee, W. S. S. On the rat model of human osteopenias and osteoporoses. *Bone Miner.* **18,** 227–236 (1992).
12. Kalu, D. N. The ovariectomized rat model of postmenopausal bone loss. *Bone Miner.* **15,** 175–191 (1991).
13. Smith, S. Y., Jolette, J. & Turner, C. H. Skeletal health: Primate model of postmenopausal osteoporosis. *Am. J. Primatol.* **71,** 752–765 (2009).
14. Wallace, J. M., Erickson, B., Les, C. M., Orr, B. G. & Banaszak Holl, M. M. Distribution of type I collagen morphologies in bone: Relation to estrogen depletion. *Bone* **46,** 1349–1354 (2010).
15. Khan, A. A. *et al.* Diagnosis and management of osteonecrosis of the jaw: A systematic review and international consensus. *J. Bone Miner. Res.* **30,** 3–23 (2015).
16. Shane, E. *et al.* Atypical subtrochanteric and diaphyseal femoral fractures: Second report of a task force of the American society for bone and mineral research. *J. Bone Miner. Res.* **29,**

1–23 (2014).

17. Khan, A. A. *et al.* Bisphosphonate associated osteonecrosis of the jaw. *J. Rheumatol.* **36,** 478–490 (2009).
18. Drake, M. T., Clarke, B. L. & Khosla, S. Bisphosphonates: Mechanism of action and role in clinical practice. *Mayo Clin. Proc.* **83,** 1032–1045 (2008).
19. Troen, B. The role of cathepsin K in normal bone resorption. *Drug News Perspect.* **17,** 19–28 (2004).
20. Erickson, B. *et al.* Nanoscale structure of type I collagen fibrils: Quantitative measurement of D-spacing. *Biotechnol. J.* **8,** 117–126 (2013).
21. Wallace, J. M. *et al.* Type i collagen exists as a distribution of nanoscale morphologies in teeth, bones, and tendons. *Langmuir* **26,** 7349–7354 (2010).
22. Fang, M., Goldstein, E. L., Matich, E. K., Orr, B. G. & Holl, M. M. B. Type I Collagen Self-Assembly: The Roles of Substrate and Concentration. *Langmuir* **29,** 2330–2338 (2013).
23. Fang, M. *et al.* Type i collagen D-spacing in fibril bundles of dermis, tendon, and bone: Bridging between nano- and micro-level tissue hierarchy. *ACS Nano* **6,** 9503–9514 (2012).
24. Su, H.-N. *et al.* The ultrastructure of type I collagen at nanoscale: large or small D-spacing distribution? *Nanoscale* **6,** 8134–9 (2014).
25. Fantner, G. E. *et al.* Hierarchical interconnections in the nano-composite material bone: Fibrillar cross-links resist fracture on several length scales. *Compos. Sci. Technol.* **66,** 1202–1208 (2006).
26. Hassenkam, T. *et al.* High-resolution AFM imaging of intact and fractured trabecular bone. *Bone* **35,** 4–10 (2004).
27. Hassenkam, T. *et al.* Atomic force microscopy on human trabecular bone from an old woman with osteoporotic fractures. *Micron* **36,** 681–687 (2005).
28. Castaneda, S. *et al.* Characterization of a new experimental model of osteoporosis in rabbits. *J. Bone Miner. Metab.* **26,** 53–59 (2008).
29. Komori, T. Animal models for osteoporosis. *Eur. J. Pharmacol.* **759,** 287–294 (2015).
30. Diggle, P., Heagerty, P., Liang, K.-Y. & Zeger, S. *Analysis of Longitudinal Data*. (Oxford University Press, 2002).
31. Weitzmann, M. N. & Pacifici, R. Estrogen deficiency and bone loss: an inflammatory tale.

J. Clin. Invest. **116,** 1186–1194 (2006).

32. S., K. *et al*. Estrogen and the skeleton. *Trends Endocrinol.Metab* **23,** 576–581 (2012).

Chapter 4.

Binding of pigment epithelium derived factor (PEDF) in rabbit femur is dependent on type I collagen microstructure

In collaboration with: Phillip Yang, Rachel Merzel, Prof. Bradford G. Orr, and Prof. Mark M. Banaszak Holl

4.1 Introduction

Pigment epithelial derived factor (PEDF) is a non-inhibitory member of the serpin class of proteins with various biological functions including anti-angiogenesis, anti-vasopermeability, anti-tumor, and neurotrophic activities.[1] This 50 kDa protein is expressed ubiquitously in humans.[2,3] In bone, PEDF is primarily expressed and secreted by osteoblasts and is highly expressed at areas of active bone formation.[4] Direct binding of PEDF to type I collagen has been characterized and the binding consists of ionic interactions between a negatively charged area on the surface of PEDF and positively charged residues in collagen.[5] As seen in **Figure 4.1**, the aspartic acid and glutamic acid residues highlighted in red make up a negatively charged region on PEDF that is thought to interact with positively charged residues in type I collagen. This proposed binding site is comprised of the following residues on PEDF: E^{41}, E^{42}, E^{43}, D^{44}, D^{64}, D^{256}, D^{258}, E^{290}, E^{291}, E^{296}, E^{300}, and E^{304}.[5] On type I collagen, PEDF binds with high affinity to KG*X*RGF*X*GL sequences in the triple helix. There are two binding sites on the human α1(I) chain that bind PEDF with high affinity: KGHRGFSGL at residues 87-95 and IKGHRGFSGL at residues 929-938.[6] There is a large amount of overlap between the binding motifs for PEDF and

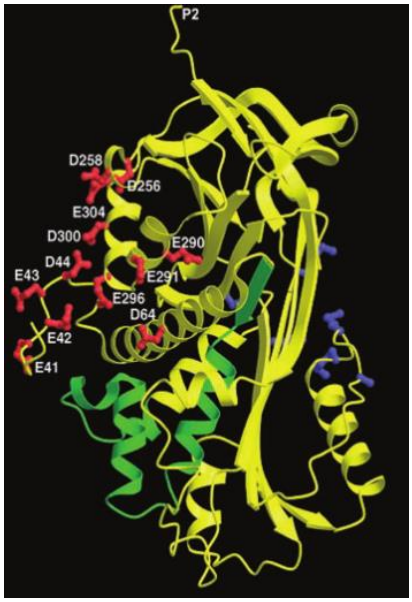

Figure 4.1 3D structure of human PEDF (PDB ID 1IMV) with proposed collagen binding site highlighted in red. Reprinted from Meyer et al.[5]

heparin/heparin sulfate proteoglycans (HSPG) on type I collagen.[5,6] The heparin/HSPG binding motif is KGHRG(F/Y). The sequence-specific interaction between PEDF and collagen suggests that binding is a highly regulated process.[6]

We have used atomic force microscopy to characterize binding patterns of PEDF in cortical rabbit femur. The microstructure of collagen fibrils in this tissue is heterogeneous. On average, 52% of fibrils that have a defined D-spacing are aligned *Parallel* to adjacent fibrils and are part of a larger structure (collagen bundle or sheet). 45% of fibrils are *Oblique* to surrounding fibrils. The remaining 3% are in rare microstructures such as fibril pairs or fibrils perpendicular to a bundle. This method for analysis of microstructure in bone (*Parallel/Oblique* fibrils) has been fully described.[7] We have successfully imaged the binding locations of PEDF with respect to collagen microstructure. Our findings demonstrate that PEDF does not bind homogeneously in cortical rabbit femur. PEDF binding is concentrated at areas between microstructures with highly aligned collagen fibrils or between collagen fibrils. Binding is rarely observed on or within the collagen fibrils themselves.

4.2 Methods

4.2.1 Sample Preparation and Initial AFM Imaging

Nine month old New Zealand white rabbit bones were obtained from Merck Research laboratories and stored in 95% ethanol.[7,8] Sections of the cortical femur were polished with a polishing wheel using a 3 μm diamond suspension in preparation for imaging with atomic force microscopy (AFM). Demineralization was achieved by suspending the samples in 0.5 M EDTA pH = 8.0 for 90 minutes while shaking at room temperature. The sample was sonicated for 5 minutes in nanopure water both before and after demineralization. After the sample was allowed to air dry, AFM imaging was performed in air at room temperature in tapping mode (Nanoscience Instruments; Aspire conical tapping mode AFM probes; 300 kHz, 40 N/m, radius 8 nm). Initial scans were 30 μm × 30 μm in area. Subsequent images were areas within the initial scan area and were 10 μm × 10 μm and 3.5 μm × 3.5 μm. The 3.5 μm^2 images are the size scale that qualitative comparisons will be made after binding with PEDF. In some instances, a series of 50 μm × 50 μm scans were obtained with varying offset values to assist in locating the same 3.5 μm^2 imaging area after PEDF binding.

4.2.2 Preparation of Solutions

Stock solutions of 25-50 nM PEDF were prepared in the following buffer: 20 mM Tris pH 7.5 and 150 mM NaCl. The stock solutions were aliquoted and then frozen at -80ºC until ready for use in an experiment. The day of an experiment, a solution of 0.1 M DTT was prepared. Immediately before the experiment, DTT was added to the PEDF aliquots so that the final solution used for the experiment was either 25 or 50 nM PEDF, 20 mM Tris pH 7.5, 150 mM NaCl, and 2 mM DTT.

The stock solution of streptavidin-Au nanoparticles were stored at 4ºC. The day of an experiment, an aliquot of the stock solution was diluted with buffer (5 mM sodium azide, 0.1% BSA, and 5 mM Tris pH 7.5) so that there would be an equimolar ratio of streptavidin and PEDF (i.e. 50 nM PEDF and 50 nM streptavidin-Au).

4.2.3 AFM imaging of Rabbit Femur Exposed to PEDF (Schemes 4.1 and 4.2)

4.2.3.1 Binding PEDF and Attaching Secondary Tag in Separate Steps (Scheme 4.1)

Following the initial imaging procedure (described in 4.2.1), the sample was removed from the AFM and 30 µL of solution containing PEDF was deposited as a droplet onto the polished bone surface. The solution remained as a droplet on the polished surface for 10 minutes at room temperature. After the incubation period, the liquid was wicked away from the surface with a Kimwipe. Then, 30 µL of the streptavidin-Au solution was deposited as a droplet and remained for ten minutes prior to wicking. The surface was gently rinsed with additional buffer (5 mM sodium azide, 0.1% BSA, and 5 mM Tris pH 7.5). The rinsing procedure involved depositing the buffer and wicking it away multiple times.

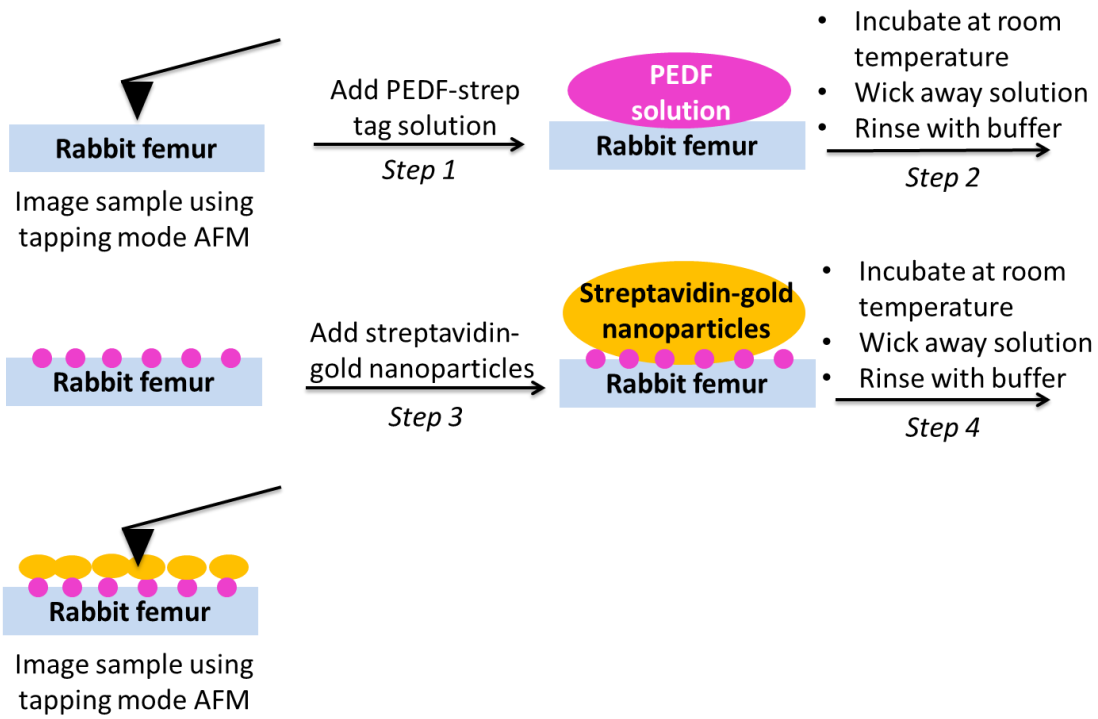

Scheme 4.1 Method 1 of exposing the rabbit femur to PEDF for binding experiments.

- *Step 1*: Concentration of PEDF-strep tag solution was either 25 nM or 50 nM; 30 µL of solution was deposited onto the surface
- *Step 2*: Rinsing buffer: 20 mM Tris pH 7.5, 150 mM NaCl, and 2 mM DTT; Incubation time was 10 minutes
- *Step 3*: 30 µL of solution was deposited onto the surface. The concentration of streptavidin-gold nanoparticles (Step 3): 25 nM or 50 nM; The concentration for this solution is referring to the concentration of streptavidin protein. The gold nanoparticles are 10 nm and are attached to the streptavidin protein. The concentration of streptavidin was always the same as the concentration of PEDF used in Step 1.
- *Step 4*: Rinsing buffer: 5 mM sodium azide, 0.1% BSA, and 5 mM Tris pH 7.5.

4.2.3.2 Pre-Mixing PEDF/streptavidin-Au before PEDF Binding to Bone (Scheme 2)

15 µL of the PEDF solution (25 or 50 nM) and 15 µL of the streptavidin-Au nanoparticle solution (25 or 50 nM) were combined and mixed for 5-10 minutes. All 30 µL of the mixed solution were deposited as a droplet and the allowed to incubate at room temperature for 10 minutes. The liquid was wicked away with a Kimwipe and the surface was gently rinsed with buffer (5 mM sodium azide, 0.1% BSA, and 5 mM Tris pH 7.5).

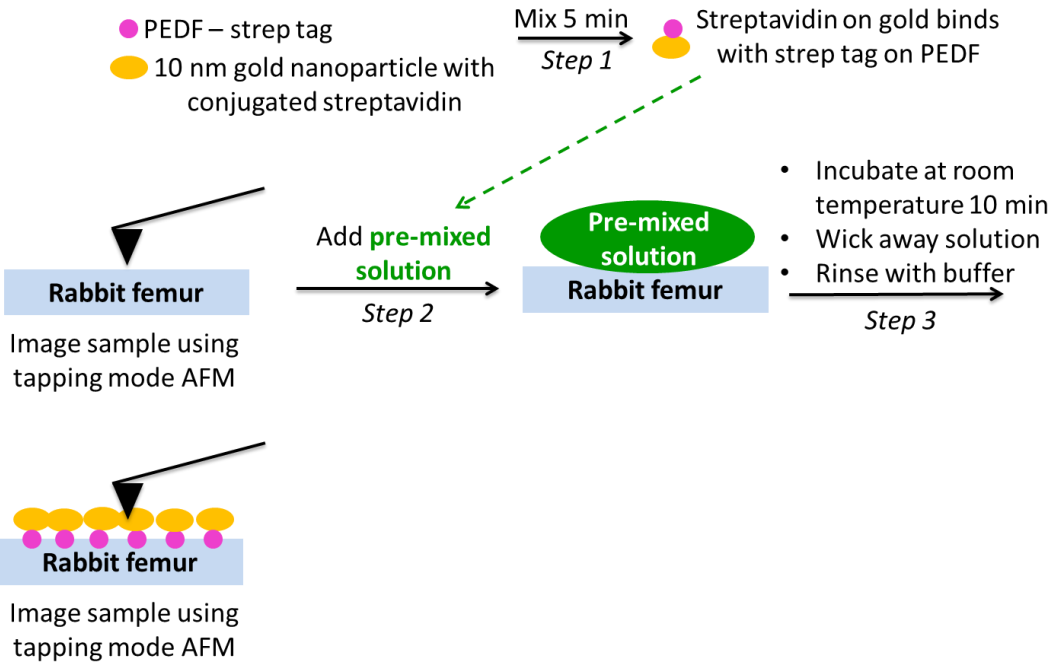

Scheme 4.2 Method 2 of exposing the rabbit femur to PEDF for binding experiments.

- *Step 1*: Concentration of PEDF-strep tag solution was 25 or 50 nM*;* Concentration of streptavidin-gold nanoparticles was 25 nM or 50 nM*;* 5-10 min incubation time
- *Step 3*: Rinsing buffer 5 mM sodium azide, 0.1% BSA, and 5 mM Tris pH 7.5; 5-10 min incubation time

4.2.3.3 Streptavidin-Gold Exposure as a Control Experiment (Scheme 4.3)

Control experiments were performed without exposing the bone to PEDF. This allowed us to interpret our data without mistakenly identifying non-specific binding of gold nanoparticles as a PEDF binding event. It also allowed us to make sure that our rinsing procedure was removing all unbound gold nanoparticles. If the control experiment showed no gold nanoparticles, then the

gold nanoparticles in experiments from Schemes 4.1 and 4.2 must be a result of PEDF binding. For these experiments, 30 µL of a streptavidin-gold nanoparticle solution that was either 25 or 50 nM was deposited onto the surface of the bone. The concentration was calculated for the streptavidin protein. After incubating for 10 minutes at room temperature, the solution was wicked away with a Kimwipe and rinsed with buffer (5 mM sodium azide, 0.1% BSA, and 5 mM Tris pH 7.5).

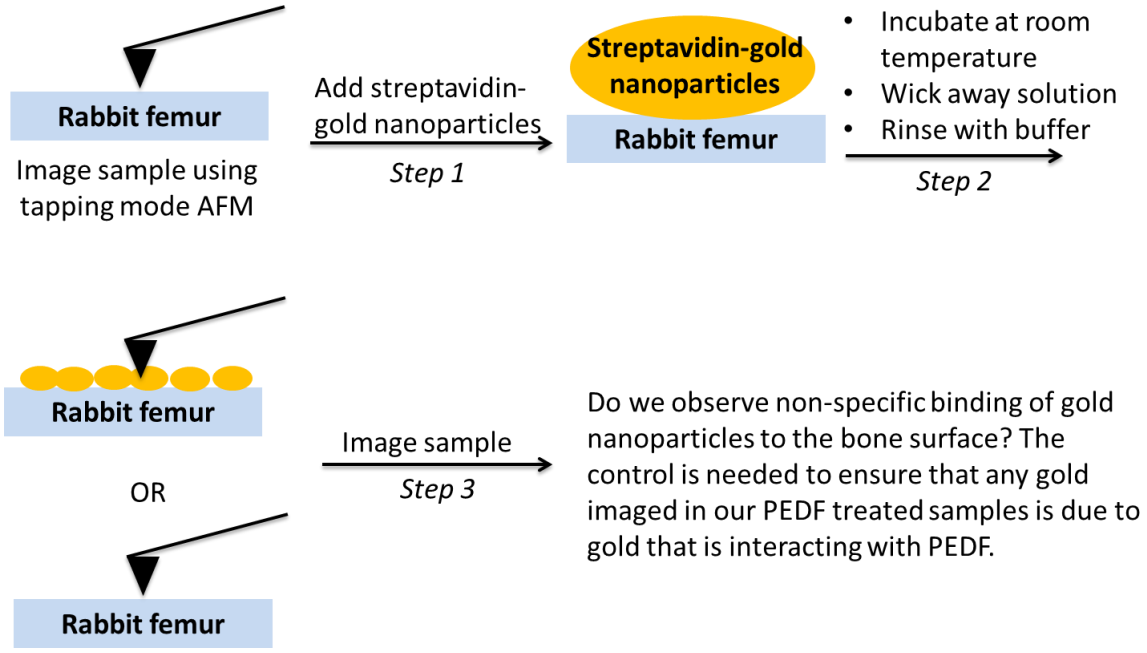

Scheme 4.3 Control Experiment

Step 1: 25 nM or 50 nM streptavidin-gold solution (concentration refers to the concentration of streptavidin)

Step 2 Rinsing buffer: 5 mM sodium azide, 0.1% BSA, and 5 mM Tris pH 7.5; incubation time of 10 minutes

4.2.4 Infrared Spectra using combined AFM-IR

Additional imaging was done with nanoIR2 by Anasys Instruments (Santa Barbara, California). First, a tapping mode image was taken to identify the gold nanoparticles in the phase contrast image (Tapping Mode NIR2Probes for nanoIR2, 75 kHz, 107 N/m, Anasys Instruments). Images taken on the nanoIR2 were comparable to the images obtained using the Agilent 5500 AFM. This similarity was necessary so that features being identified by IR in the nanoIR2 were

the same features that were detected using the Agilent 5500 AFM. Then, the tip was engaged in contact mode and an IR spectrum was obtained. The Au nanoparticles did not have a peak in the IR spectrum that the instrument can measure. However, when the laser shines on gold, there will be a greater intensity in the absorbance than when the laser shines on the bone or bone mineral. This phenomenon, called signal enhancement, was used to identify the presence of gold nanoparticles. IR spectra were obtained at various locations in the 3.5 μm^2 image using the same laser power. These locations were hand-selected based on the features observed in the phase image. IR spectra were obtained both at these sites of phase contrast as well as varying distances from those features. The absorbance intensity for the amide I and amide II peaks (approximately 1690 and 1580 cm^{-1} for these samples) were compared for all locations measured. Gold nanoparticles were identified when phase contrast was coupled with an increase in IR absorbance at 1690 and 1580 cm^{-1} relative to surrounding collagen without phase contrast.

4.3 Results and Discussion

The PEDF protein is too small to be resolved in the context of the Type I collagen fibrils unless tagged with something that is both larger and has substantially different physical characteristics. We tagged our PEDF protein with 10 nm gold nanoparticles. Our motivation for tagging with gold was to utilize the phase image capability of tapping mode AFM. The phase image is a measurement of the phase shift of the oscillating cantilever. Variations in sample hardness, adhesion, and viscoelasticity alter sample-tip interactions and lead to a phase shift. By recording changes in the phase signal, materials with different properties can be distinguished from one another.

Gold is much harder than collagen and was detectable in the phase image. In order to tag the PEDF protein, we used a recombinantly made protein with a streptavidin tag provided by Jan Gebauer and Ulrich Baumann (Universitat Zu Koln, Cologne, Germany). We purchased 10nm gold nanoparticles that were conjugated to streptavidin. The streptavidin tag binds to streptavidin on the gold nanoparticle and this binding event attaches the gold nanoparticle to the PEDF protein.

Samples of rabbit femur exposed to PEDF through schemes 1 and 2 produced phase images with dark circular features. These same features were also detected in the topography and amplitude images. We believe the dark areas in the phase image after binding to PEDF in **Figure 4.2** indicate areas where PEDF-streptavidin gold is interacting with collagen. The gold

nanoparticles should be distinct from surrounding collagen in phase imaging because gold is much harder than collagen. The dark area in the phase image before exposure to PEDF is likely due to bone mineral. This issue is addressed in the discussion for **Figure 4.3**.

The size of the features in the phase image after PEDF exposure provides additional evidence that these features are the gold nanoparticles. The size of the smaller dark features in the phase image are consistent with the size of the nanoparticles (10 nm, about 1/6 or 1/7 of the collagen fibril width). The PEDF appears to interact with the surface at the edges of collagen fibrils.

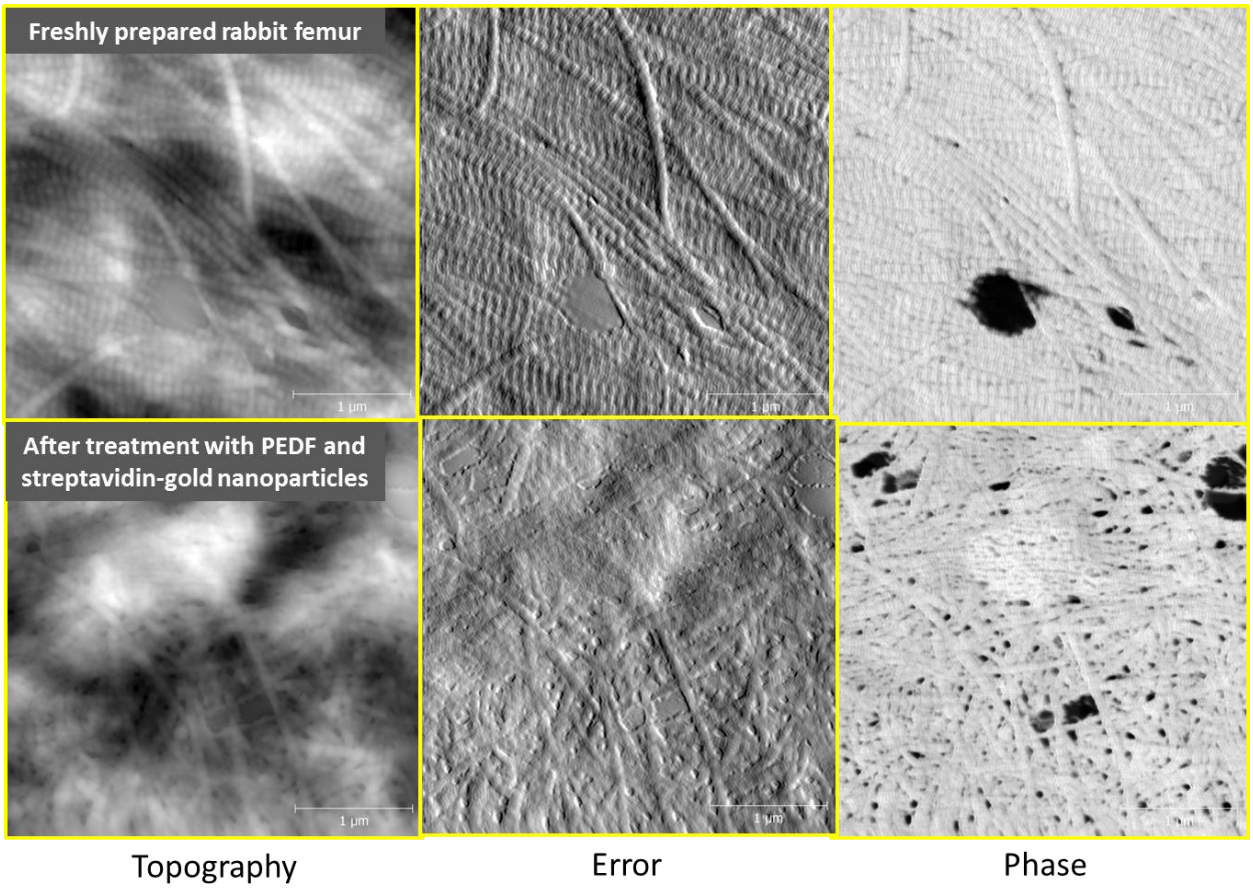

Figure 4.2 AFM image before and after exposure to PEDF using Scheme 1. The dark area in the "before" image is likely due to mineral. The smaller dark areas in the "after" images are being interpreted as gold nanoparticles and PEDF binding events.

As mentioned previously, bone mineral is also much harder than collagen and will look similar to gold in AFM phase images. One way to address this issue was to image at the same location before and after exposing the bone to PEDF solutions. **Figure 4.3** is a representative set of images showing the results of this type of experiment. This experiments were carried out using the pre-mixing method described in **Scheme 4.2**. Before exposure to PEDF, no dark areas are seen in the phase image, meaning that no mineral is detected in the phase image. After exposure to the PEDF/streptavidin-Au solution, dark areas appear that were not present before. These areas are being interpreted as areas with gold nanoparticles and areas where PEDF is interacting with collagen. The gold nanoparticles bound primarily in between collagen bundles and collagen fibrils. The PEDF was not observed to bind on the collagen fibrils themselves.

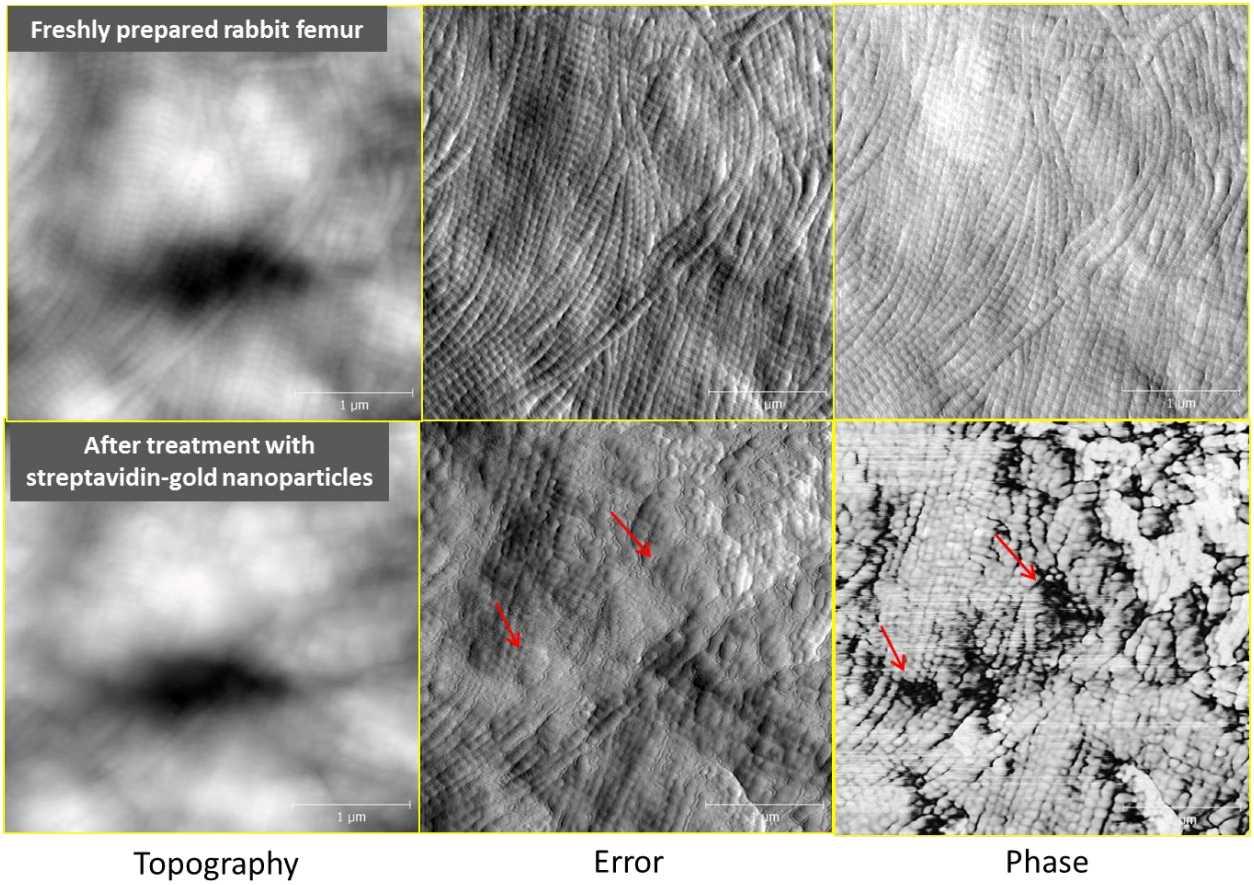

Figure 4.3 AFM image of the same location in rabbit femur before (top row) and after (bottom row) exposure to PEDF-Au nanoparticles. The dark areas in the phase image are PEDF-Au binding events.

A control experiment was important to ensure that any gold identified on the bone surface is a result of PEDF/collagen interactions and not a result of non-specific binding of gold nanoparticles on the surface. The control experiment is described in **Scheme 4.3** and the results are shown in **Figure 4.4**. Non-specific binding of gold nanoparticles to the bone surface was not observed. The features present in these images are likely mineral. The gold nanoparticles in **Figures 4.2** and **4.3** were seen as dark circular features in the phase image. The features seen here are irregularly shaped and often brighter than surrounding bone.

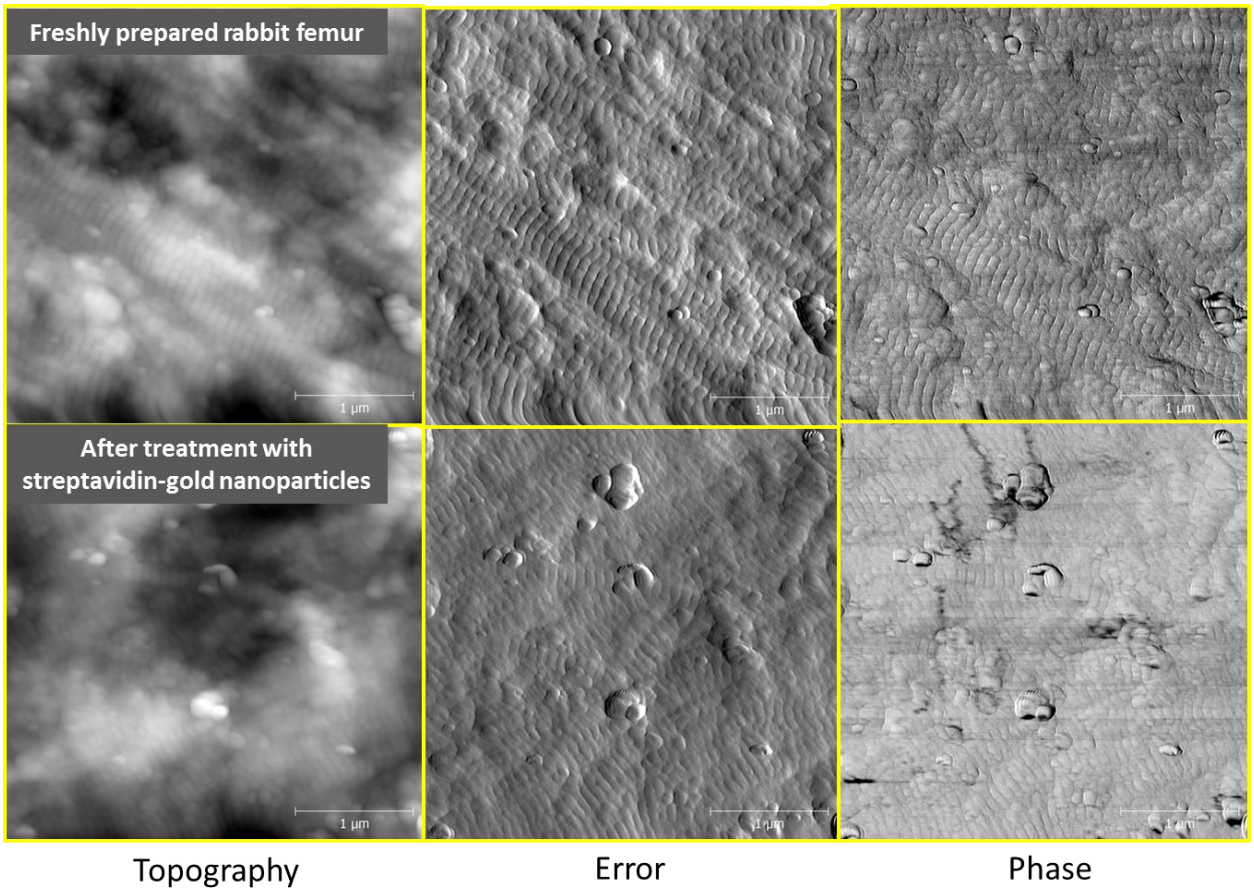

Figure 4.4 Exposure to streptavidin-Au nanoparticles in the absence of PEDF acts as a control experiment to observe non-specific binding events.

IR spectroscopy was used for further evidence on the identification of the gold nanoparticles in the phase contrast image. For these experiments, the nanoIR2 by Anasys instruments was used. After we reproduced a phase contrast image that we believed to see gold nanoparticles, we obtained

IR spectra at the particles and at varying distances from the particles. Signal enhancement near the particles indicated that the particles were gold. Bone mineral does not cause signal enhancement. In addition to enhancement, we observed the introduction of a wave pattern when near a particle (**Figure 4.5**).

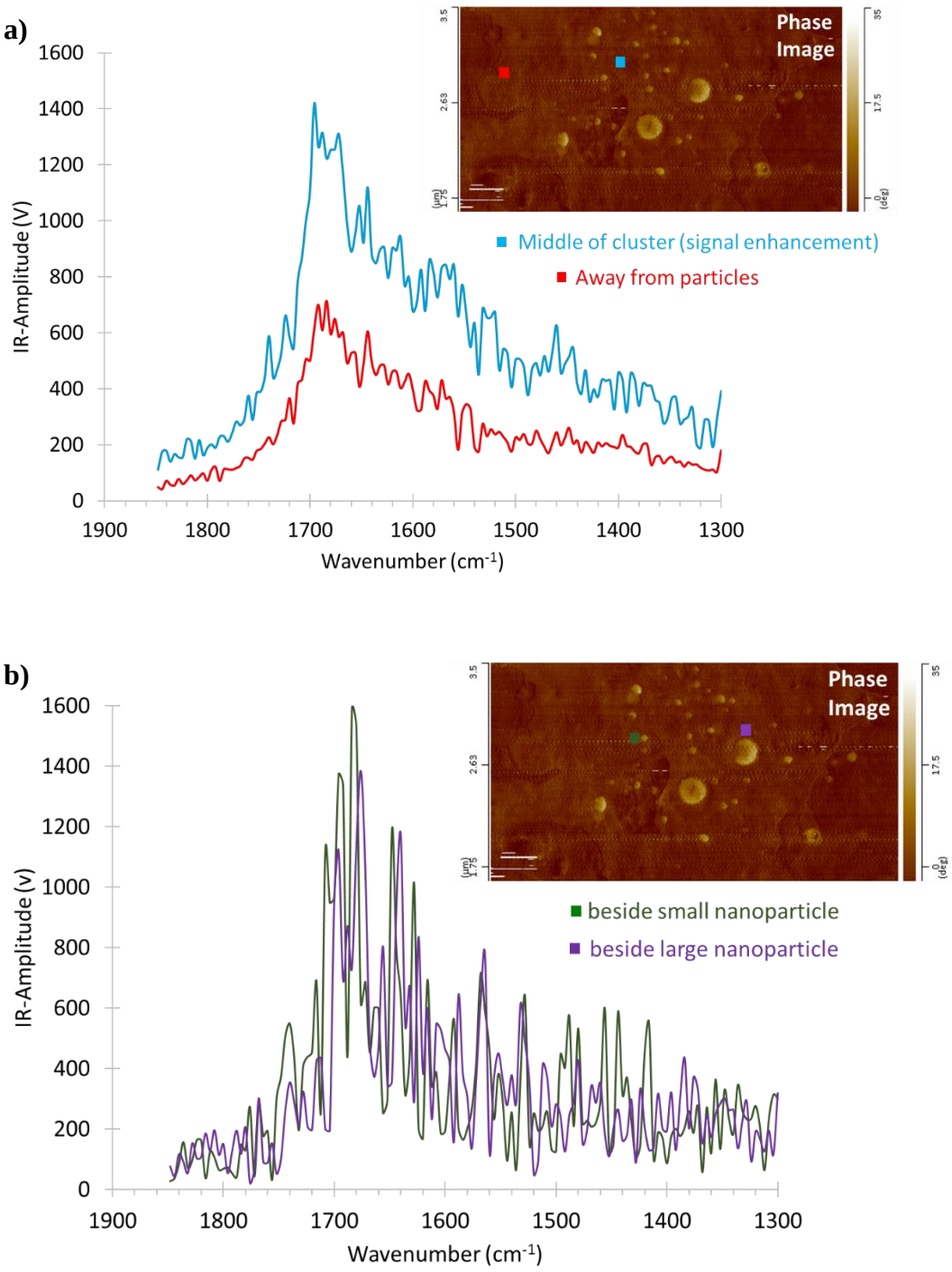

Figure 4.5 Signal enhancement suggests the presence of gold nanoparticles in the phase image. a) Signal enhancement is observed by an increase in absorbance for the location closer to the gold nanoparticles. b) Spectra obtained adjacent to a particle showed signal enhancement in addition to the presence of a wave pattern.

A loss of function mutation in the gene for PEDF, SERPINF1, results in the recessive bone disease osteogenesis imperfecta (OI) type VI.[2,3] This type of OI is unique because collagen synthesis is not impaired and there are no amino acid mutations resulting in alterations in collagen structure.[9] In OI type VI, there is an increase in osteoid tissue and an increase in the time it takes to mineralized newly formed bone. This phenotype is not observed for other types of OI.[9] The bone matrix of patients with OI type VI has been characterized by Fratzl et al.[9] and three nano/micro structural changes were reported with the diseased tissue: (1) mixture of highly mineralized bone matrix with areas of bone with low mineral content, (2) low mineralization around the boarder of lacunae with "heterogeneous and abnormally elongated fibrillary features," and (3) more heterogeneity in mineral particle size, shape, and arrangement.[9] In is interesting to note that a mutation in SERPINF1 changes the microstructure of bone matrix and binding of PEDF in healthy tissue is heterogeneous.

4.4 Conclusions

Protein interactions between PEDF and collagen were detected in tissue using AFM with a gold nanoparticle as a secondary tag. The gold nanoparticles were also identified using IR spectroscopy. There was IR signal enhancement near the gold nanoparticles as well as the introduction of a wave pattern. The location of gold nanoparticles reflects the location of PEDF binding and the binding locations were identified with respect to collagen microstructure. PEDF binding was heterogeneous and observed to bind in between areas with highly aligned collagen fibrils and between collagen fibrils. Binding was not observed within the bundles or within the collagen fibril.

4.5 Acknowledgements

The authors thank Jan Gebauer and Ulrich Baumann for providing the streptavidin tagged PEDF.

4.6 References

(1) Kawaguchi, T.; Yamagishi, S.; Sata, M. Structure-Function Relationships of PEDF. *Curr. Mol. Med.* **2010**, *10*, 302–311.

(2) Homan, E. P.; Rauch, F.; Grafe, I.; Lietman, C.; Doll, J. A.; Dawson, B.; Bertin, T.;

Napierala, D.; Morello, R.; Gibbs, R.; *et al.* Mutations in SERPINF1 Cause Osteogenesis Imperfecta Type VI. *J. Bone Miner. Res.* **2011**, *26*, 2798–2803.

(3) Venturi, G.; Gandini, A.; Monti, E.; Carbonare, L. D.; Corradi, M.; Vincenzi, M.; Valenti, M. T.; Valli, M.; Pelilli, E.; Boner, A.; *et al.* Lack of Expression of SERPINF1, the Gene Coding for Pigment Epithelium-Derived Factor, Causes Progressively Deforming Osteogenesis Imperfecta with Normal Type I Collagen. *J. Bone Miner. Res.* **2012**, *27*, 723–728.

(4) Broadhead, M.; Akiyama, T.; Choong, P.; Dass, C. The Pathophysiological Role of PEDF in Bone Diseases. *Curr. Mol. Med.* **2010**, *10*, 296–301.

(5) Meyer, C.; Notari, L.; Becerra, S. P. Mapping the Type I Collagen-Binding Site on Pigment Epithelium-Derived Factor: Implications for Its Antiangiogenic Activity. *J. Biol. Chem.* **2002**, *277*, 45400–45407.

(6) Sekiya, A.; Okano-Kosugi, H.; Yamazaki, C. M.; Koide, T. Pigment Epithelium-Derived Factor (PEDF) Shares Binding Sites in Collagen with Heparin/heparan Sulfate Proteoglycans. *J. Biol. Chem.* **2011**, *286*, 26364–26374.

(7) Cauble, M. A.; Rothman, E.; Welch, K.; Fang, M.; Duong, L. T.; Pennypacker, B. L.; Orr, B. G.; Banaszak Holl, M. M. Alteration of Type I Collagen Microstructure Induced by Estrogen Depletion Can Be Prevented with Drug Treatment. *Bonekey Rep.* **2015**, *4*, 697.

(8) Pennypacker, B. L.; Duong, L. T.; Cusick, T. E.; Masarachia, P. J.; Gentile, M. A.; Gauthier, J. Y.; Black, W. C.; Scott, B. B.; Samadfam, R.; Smith, S. Y.; *et al.* Cathepsin K Inhibitors Prevent Bone Loss in Estrogen-Deficient Rabbits. *J. Bone Miner. Res.* **2011**, *26*, 252–262.

(9) Fratzl-Zelman, N.; Schmidt, I.; Roschger, P.; Roschger, A.; Glorieux, F. H.; Klaushofer, K.; Wagermaier, W.; Rauch, F.; Fratzl, P. Unique Micro- and Nano-Scale Mineralization Pattern of Human Osteogenesis Imperfecta Type VI Bone. *Bone* **2015**, *73*, 233–241.

Chapter 5

Type I Collagen Fibril Nanomorphology: D-spacing, Persistence Length, and the Microfibril to Fibril Transition

In collaboration with Chelsea Finkbeiner, Phillip Yang, Dalia Antebi-Lerman, Prof. Bradford G. Orr and Prof. Mark M. Banaszak Holl

Submitted to *Langmuir*

5.1 Introduction

Type I collagen molecules assemble to form the protein scaffold for bone, dentin, skin, and tendon.[1-6] In addition to Type I collagen, these tissues contain other types of collagen, additional proteins, and, in the case of bone and dentin, hydroxyapatite mineral. The Type I collagen molecules, which are on the order of 1.5 nm in diameter and 300 nm in length, assemble with these additional components into complex hierarchical structures including microfibrils, fibrils, and fibers to form tissue structures that vary in size from microns to meters. The structural complexity and compositional heterogeneity of these materials has led to the use of simpler model systems for the exploration of Type I collagen structure and properties. The model systems allow study of structural properties in the absence of biological processing events including mineralization, cross-linking, and protein chaperones.

The assembly of collagen molecules into microfibrils and fibrils and elucidation of the details of the structure remains a challenging problem. Major techniques employed to shed light on these structures include electron microscopy (EM), X-ray diffraction (XRD), and atomic force microscopy (AFM). When comparing results between the different techniques, it is important to keep in mind the key advantages, limitations, and idiosyncrasies of each method. EM, the first method used to characterize collagen fibrils, evaluates modulation of electron density in space. EM provides structural data on the level of the individual fibril; however, it is important to keep in mind that the electron density patterns reported are typically not of the Type I collagen fibril

directly, but rather reflect the electron density of a negative or positive stain.[7,8] EM data has also been acquired on polymer casts of Type I collagen fibrils.[9] XRD is similar to EM in that it measures the spatial electron density of the sample; however, XRD is an ensemble method that averages over micron to millimeter spatial dimensions and does not provide data on the structure of individual Type I collagen microfibrils or fibrils. AFM is distinct from both EM and XRD in that it measures surface topography and is not a measure of internal fibril electron density. AFM is able to provide data on the level of the individual collagen molecule, microfibril, and fibril and does not require staining for image contrast.[10]

Previous reports have described the use of reconstituted rat tail collagen self-assembled onto a mica substrate to form microfibril and fibril microribbons[11,12] that retain key nano- to micro-scale features of tissue-based collagen fibrils. AFM imaging provides a convenient, label-free method for the analysis of the resulting structures and provides quantitative, topographical information. We employed conventional silicon AFM probes with a nominal 10 nm tip diameter as well as carbon-nanotube (CNT) probes with a nominal 1 nm tip diameter in order to provide a new level of resolution of microfibril structure within the self-assembled fibril microribbons. Using these approaches, we have been able to estimate the number of collagen molecules present in the microfibrils and fibrils, the numbers of collagen molecules/microfibrils needed to generate a fibril with a multimicron persistence length, and the number of collagen molecules required to generate an AFM observable topographical D-spacing. The CNT probe also provided a high degree of resolution of the microfibrils making up large fibrils including the development of nanoscale banding perpendicular to the fibril axis. The nanoscale axial banding was evaluated using line scans to evaluate the distribution of dimensions observed and using Fourier transforms to assess the average dimensions of the repeating structure.

These studies examining self-assembly of rat tail collagen on mica lead to several new quantitative conclusions regarding the relationship of Type I collagen microfibrils and fibrils. Consistent with the proposals of previous structural models,[5,6,13-15] the smallest microfibrils were measured with cross-sectional areas consistent with the presence of five collagen molecules. These microfibrils, as well as larger structures consisting of ~5-8 of these microfibrils or about 40 collagen molecules in cross-section, did not exhibit detectable axial spacings or a substantial persistence length. By way of contrast, fibrils containing greater than 10 microfibrils and about 90

collagen molecules in cross-section exhibited both axial spacing and micron scale persistence lengths.

5.2 Experimental Section

5.2.1 Type I Collagen Self-Assembly

All samples were prepared from Type I collagen derived from rat-tail tendon (4.0 mg/mL, >90% purity by SDS-PAGE; BD Biosciences; Franklin Lakes, NJ). A collagen stock solution to be used for experiments was prepared by diluting the purchased 4.0 mg/mL collagen solution to 1.65 mg/mL with 0.1% acetic acid. All solutions were stored at 4˚C. The mica substrate was glued onto steel atomic force microscopy pucks (SPI supplies; West Chester, PA). Mica was freshly cleaved by removing top layers with adhesive tape. A 25 μg/mL solution of collagen in buffer (30 mM Na_2HPO_4, 10 mM KH_2PO_4, 200 mM KCl) was prepared from the 1.65 mg/mL collagen stock solution and 30 μL was deposited onto freshly cleaved mica. Samples were incubated at room temperature in a moist chamber for varying times from 20 to 120 minutes. The surface was rinsed with nanopure water followed by wicking the water from the surface with a paper towel to prevent drying artifacts. The sample was further dried under weak nitrogen flow for 5-10 minutes.

5.2.2 AFM Imaging and Image Analysis.

Samples were imaged in air using PicoPlus 5500 Atomic Force Microscopy (Agilent) in tapping mode. Two types of probes were employed: Silicon cantilevers (VistaProbes T300R, tip radius < 10 nm, force constant 40 N/m, resonance frequency 300 kHz; nanoScience Instruments; Phoenix, AZ) and Carbon Nanotube (CNT) containing cantilevers (FN-1 CNT tip, tip radius ~0.5 nm, force constant 3 N/m, resonance frequency 60 kHz; K-Tek, Wilsonville, OR). The microscope was calibrated using a 100 nm pitch grid (2D-100; NANOSENSORS, Switzerland) using the methods previously described.[16] Image analysis was carried out using SPIP and Gwyddion software using approaches described in previous publications.[16,17] For Table 1, average values and standard deviations of full-width-at-half-maximum (FWHM), height, width, and cross-sectional area were generated from a minimum of 10 separate measurements. The number of collagen molecules for each microfibril or fibril bundle was estimated by dividing the measured cross-sectional area by the cross-sectional area for a collagen molecule (1.46 nm^2).

5.3 Results and Discussion

Collagens are based on trimeric polypeptide chains, each of which includes a repeating Gly-X-Y triplet region where X and Y are often proline and hydroxyproline.[1-3] The fibrillar-forming class (types I, II, III, V, and XI) has an approximately 300 nm long, uninterrupted molecular triple helix with type I accounting for 70% of all collagens. The fibrils formed from packing and cross-linking of the molecular triple helix are found throughout the body in the extracellular matrices (ECMs) of teeth, bones, tendons, skin, arterial walls and cornea.[18] The type I collagen fibrils exhibit a prominent axial spacing that has elicited substantial interest since the dawn of electron microscopy (EM). The axial spacing was first reported with measurements resolved at the level of the individual fibril in 1942 by Schmitt et al.[19,20] A distribution of axial spacings centered at ~64 nm was observed for rat tail collagen. Cognizant that drying the tissue for EM studies could introduce artifacts into the measurements, Gross and Schmitt made plastic imprints of moist fibrils obtained from human skin in formvar and collodion and measured the structures of the plastic replicas.[9] They obtained a slightly narrower distribution of axial spacings that ranged from 50 to 80 nm and was centered at 64 nm, but were able to rule out dehydration of the collagen fibril as the source of the dispersion in the axial spacings. Contemporaneous with these studies, the first X-ray diffraction measurements of type I collagen fibrils consistent with the EM results identified the presence of an axial spacing of ~64 nm.[21,22] In 1963, the first model explaining how collagen molecules could pack to yield the observed fibrillar structure was developed by Hodge and Petruska.[23] They proposed that molecules within a fibril are arranged in a staggered parallel alignment, resulting in “gap” and “overlap” regions to give a D-periodic axial gap/overlap spacing (D-spacing) that generates the axial electron density waves observed by the electron microscopy[19,20] and X-ray studies.[21,22] Single crystal X-ray diffraction studies have subsequently allowed the generation of a more sophisticated three-dimensional model of the *average* fibril structure consistent with five-stranded microfibrils that are supertwisted in the axial direction and quasi-hexagonally packed in the equatorial plane.[13,24-26]

Although much of the field has focused on improving knowledge of the average structure of collagen fibrils and how it can be used to understand mechanical properties and disease,[1,27] numerous studies have appeared examining the structure at the level of the individual fibril. In these studies, distributions of D-spacings have been observed for healthy tissue,[28] diseased and drug treated tissue[10,16,29-41] and for self-assemblies of collagen fibrils on surfaces.[17] Despite the

observation of the D-spacing distribution for a wide variety of tissues types (bone, teeth, tendon, skin) the structural origin of the distribution and the relationship of the distribution to the average fibril models built with a single D-spacing value (Hodge-Petruska and Orgel) has remained unclear.

5.3.1 AFM Measurements on Self-Assembled Type I Collagen Microribbons on Mica

In order to gain a greater understanding of the structural origin of D-banding we explored AFM imaging of self-assembled rat tail Type I collagen on mica in order to look at the transition between microfibril[42] and fibril structures.[17,43] The structures formed in this fashion are best described as collagen microribbons,[11,12] as opposed to the cylindrical fibrils found in nature; however, the microribbons do exhibit the same D-spacing pattern. Samples for imaging were generated following the general approach of Leow et al. employing collagen molecules from rat-tail tendon suspended in phosphate buffer.[43] The collagen in buffer was incubated on a freshly cleaved mica surface followed by rapid wicking away of the buffer solution. Images were obtained using either nominal 10 nm conical silicon tips or nominal 1 nm CNT tips.

A region of self-assembled collagen on mica illustrating the presence of microfibril and fibril microribbons is illustrated in **Figures 5.1**. Three domains are present in the 10 × 10 μm region shown in panel A. Domain I consists primarily of microfibrils with widths of ~20-40 nm and heights of 0.3 to 2 nm. Domain II consists of fibril microribbons that are ~50-60 nm wide and ~2-3 nm in height. Domain III highlights a micron-sized region where the Domain II fibril microribbons come apart into microfibrils and then reassemble. Line profiles of the fibril and microfibril microribbons are provided in panels D and E. Metrical parameters from multiple measurements of fibrils and microfibrils are summarized in **Table 5.1**. A previous study by Raspanti et al. highlighted similar fibril (Domain II) to microfibril (Domain I) transition by electron microscopy.[44]

The field of microfibril microribbons illustrated in Domain I of **Figures 5.1a** and **5.1b** can be grouped roughly into two sizes. Microfibril bundle A (mfA) (the smallest individual features observed in panel b) has an average height of 0.5 ± 0.2 nm, width of 44 ± 13 nm, and cross-sectional area of 11 ± 5 nm^2. Assuming a cross-sectional area of about 1.46 nm^2 for a collagen molecule, this corresponds to 8 ± 4 collagen molecules per mfA. This corresponds well with the average number of five collagen molecules per microfibril bundle obtained from X-ray

diffraction.[5,6,13-15] About five mfA can be seen to merge to form larger microfibril bundles in Domain I, assigned as mfB, which have an average height of 1.6 ± 0.3 nm, width of 70 ± 10 nm, and cross-sectional area of 58 ± 16 nm^2. This area corresponds to 40 ± 11 nm collagen molecules per mfB tape. Neither mfA nor mfB exhibit the classic axial periodicity of Type I collagen fibrils and they exhibit dramatically shorter persistence lengths of < 60 nm and < 400 nm, respectively. The lack of axial periodicity for both mfA and mfB is interesting because AFM is particularly sensitive to measuring changes in height with an ability to discern changes on the order of tenths of a nanometer. It is possible that the collagen molecules are already ordering with the gap/overlap structure and we are unable to detect the overall impact on topography. Alternatively, given the high degree of sensitivity of AFM towards this topographical feature, this data suggests that these self-assembled microfibrils of < ~40 collagen molecules have not reached the critical size needed to generate the higher-order gap/overlap structure. A requirement for a critical number of microfibrils is consistent with the proposal of Bozec et al. that rope structures consisting of microfibrils are responsible for the axial spacings observed by AFM.[45] The rope model does provide a ready explanation for axial D-spacing variation.

The field of fibril microribbons illustrated in Domain II of **Figures 5.1a** and **5.1b**, defined as fibril bundle C (fC) are clearly made up of microfibrils from Domain I and consist of many mfA and mfB. The fC have an average height of 2.5 ± 0.2 nm, width of 96 ± 11 nm, cross-sectional area of 134 ± 15 nm^2, and average number of collagen molecules of 92 ± 10. The fC exhibit a distinct axial periodicity reminiscent of the D-spacing observed for collagen fibrils in tissue (Panel E). Multiple measurements using 2D-FFTs at multiple locations in Domain II gave a D-spacing value of 72 ± 29 nm. The disorder present in these microribbons appears to give a large variation in the topographical spacing measured. These data indicate that ~90 collagen molecules in cross-section are sufficient to generate the classic axial periodicity of collagen fibrils. In addition, these larger microribbons now exhibit a persistence length of up to 8000 nm.

Panel C highlights Domain III where mfA can be seen crossing between two different fC (yellow ellipses). The cross-links between fC are shorter than a single collagen molecule and demonstrating a potential form of fibril-fibril cross-linking based on collagen molecule packing as opposed to chemical modification of amino acids. Interestingly, the mfA of collagen molecules accomplishes the cross-linking with no apparent disruption to the nanoscale structure, including axial periodicity, of the fC. In addition, fC can be seen breaking up into regions of mfbB. In this

region, mfB interconnect between multiple fbC sources and ultimately reconnect into new set of fC. Panels B and C also highlight a number of fibril microribbons of ~80 nm width that interconnect between larger microribbons ~120 nm width while maintaining the D-periodic registration with *both* of the larger fibrils. The fibril structures also provide an interesting cross-linking mechanism independent of chemical modification and highly conserved in terms of maintaining the axial periodicity of the fibril field.

In order to get a better understanding of the microfibril structure within the fibril microribbons (fC) we employed a carbon nanotube (CNT) modified cantilever. These tips have a nominal 1 nm diameter with the potential for a perfectly symmetrical tip shape. Collagen fibril microribbons imaged in this fashion are illustrated in **Figure 5.2** with metrical parameters summarized in **Table 5.1**. The parameters for the microfibrils were obtained by measuring individual microfibrils present at the frayed ends of the larger fibril microribbons. These microfibrils have an average height of 0.6 ± 0.2 nm, width of 32 ± 6 nm, a cross-sectional area of 10 ± 4 nm^2, and an average number of collagen molecules of 7 ± 3. This somewhat smaller set of values may result from a change in tip convolution between the ~10 nm and ~1 nm diameter tip. These fibrils, within error the same size as those in **Figure 5.1**, were also classified as microfibril A (mfA). Again, no axial periodicity was observed for these fibrils in isolation; however, as they aggregate into the large microribbons shown in **Figure 5.2** a very clear axial repeat pattern can be observed. The axial spacings show a wide range of values with median of ~80 nm as determined by line scans and an average of ~70 nm as determined by 2D-FFTs. There is no systematic evidence of the collagen sub-band spacings of ~25, ~23 and ~18 nm in these images. The larger microribbons in **Figure 5.2** (fibril E, fE) have an average height of 1.5 ± 0.3 nm, width of 240 ± 40 nm, a cross-sectional area of 200 ± 75 nm^2, and an average number of collagen molecules of 140 ± 50. The center-to-center distance between the microfibrils show regular values of ~24 and ~32 nm.

Figure 5.1 AFM Images of Microfibril and Fibril Domains in Self-Assembled Type I Collagen Microribbons on Mica (~10 nm nominal diameter probe). A) Three domains in a 10 x 10 μm image: I) microfibrils exhibiting short persistence length and no axial repeat spacing II) fibrils exhibiting >> 1 μm persistence length and the formation of an axial nanoscale repeat structure III) fibril/microfibril/fibril transition region. B) Enlargement of the border between Domains I and II where fibrils convert into microfibrils. C) Enlargement of domain III highlighting line scans employed for quantitative analysis. Yellow ellipses highlight regions were microfibrils cross-between adjacent fibrils. D) Widths and heights of collagen microribbons from panel C. Microribbons 1, 2, and 3 were 47 (1.8), 78 (2.3), and 126 (2.5) nm. E) The axial D-spacing of line scans microribbons 4, 5, 6, and 7. The average D-spacing obtained for domain II in Panel A was 72 (± 29). The nm/pixel ratios are 19.5 in Panel A and 2.0 in Panels B and C.

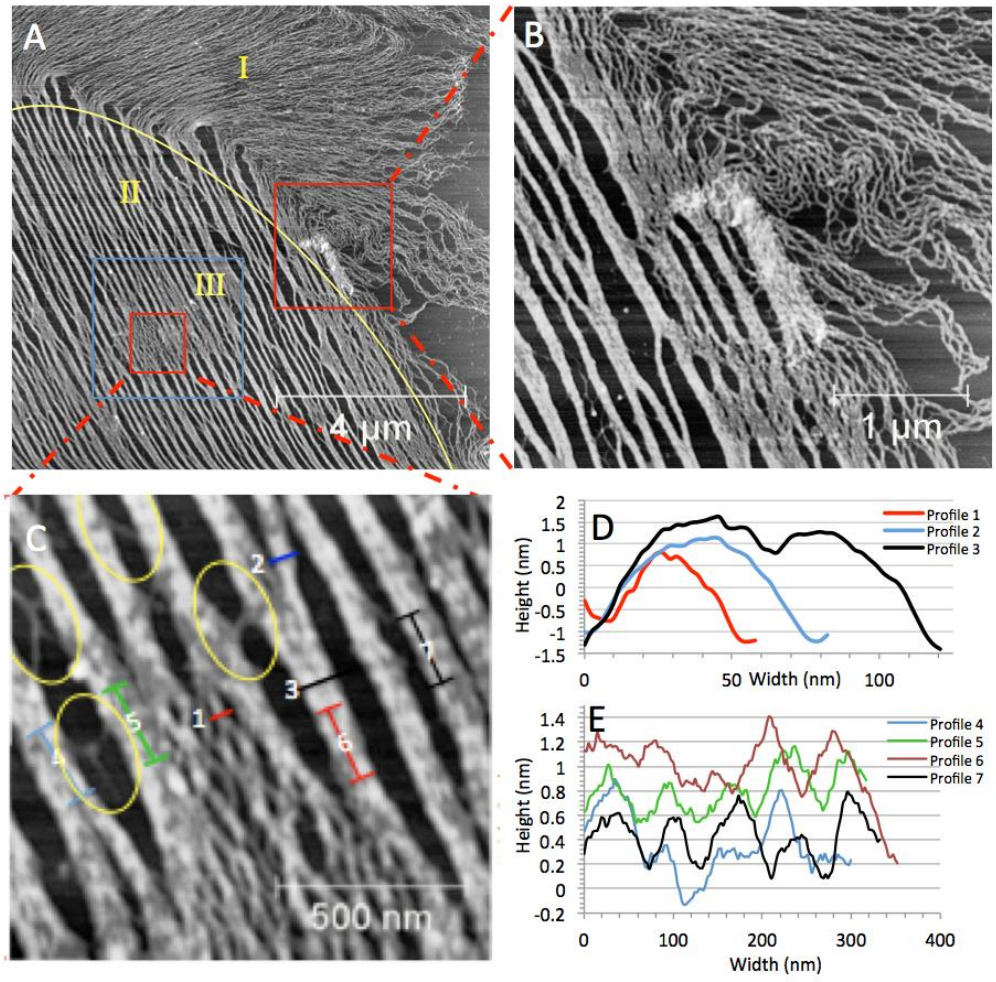

Probe Type	Tape FWHM (nm)	Tape Height (nm)	Tape Width (nm)	Tape Cross-sectional Area (nm^2)	Number of collagen molecules
Silicon 10 nm radius tip					
Microfibril A	20 (4)	0.5 (0.2)	40 (13)	11 (5)	8 (4)
Microfibril B	40 (8)	1.6 (0.3)	70 (10)	60 (15)	40 (10)
Fibril C	60 (7)	2.5 (0.2)	100 (10)	134 (15)	90 (10)
CNT 1 nm radius tip					
Microfibril A	20 (4)	0.6 (0.2)	32 (6)	10 (4)	7 (3)
Fibril E	160 (40)	1.5 (0.3)	240 (4)	200 (75)	140 (50)

Table 5.1 Quantitative Analysis of Self-Assembled Type I Collagen Microfibril Microribbons on Mica. Microfibril bundle A, the smallest fibrils observed in the images, exhibit a smooth morphology devoid of nanoscale substructure including axial D-spacing. Microfibril B is a larger sized microfibril bundle apparent in the images that also lacks additional nanoscale substructure. Fibril C exhibits nanoscale substructure including a regular axial pattern. The silicon 10 nm radius tip data were measured on **Figure 5.1**. The CNT 1 nm radius tip data were measured on **Figure 5.2**.

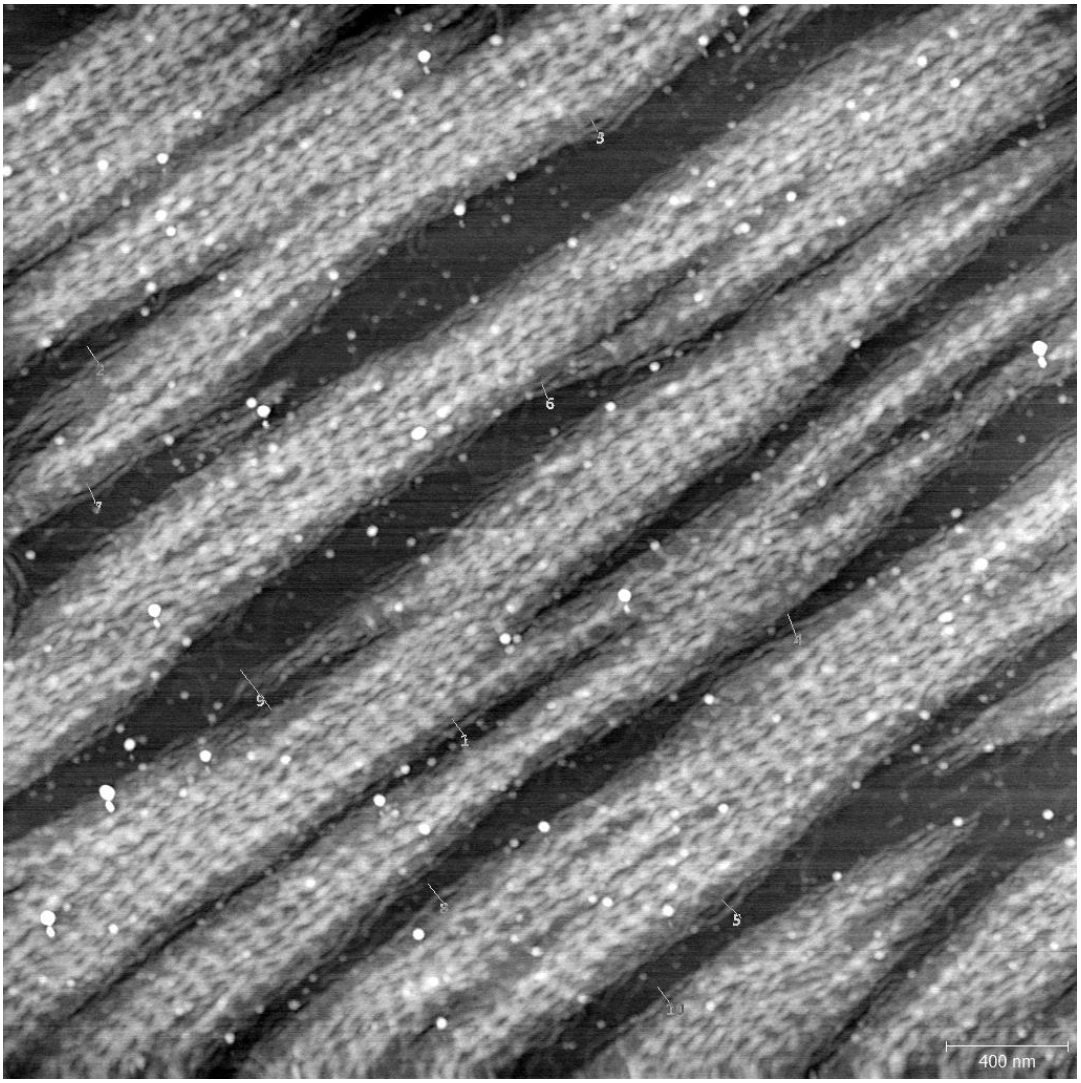

Figure 5.2 AFM Image of Fibril Domains in Self-Assembled Type I Collagen Microribbons on Mica (~1 nm nominal diameter CNT probe). Microfibrils are apparent in the fibril structure in additional to a regular axial repeat spacing that ranges from 50-80 nm as measured using 2D-FFTs. The microfibrils appear packed next to each other with the smallest center-to-center separations showing regular values of ~24 and 32 nm. Based on fibril width (~20-30 nm) and height (~0.5 nm) the individual microfibrils observed in this image are consistent with the microfibril bundle A structures.

5.4 Conclusions

Consistent with the proposals from previous structural models,[5,6,13-15] microfibrils were measured with cross-sectional areas consistent with the presence of five collagen molecules. These

smallest microfibrils, as well as larger fibrils consisting of ~5-8 of these microfibrils or about 40 collagen molecules in cross-section, did not exhibit detectable axial spacings or a substantial persistence length. By way of contrast, when the fibrils contained greater than 10 microfibrils and about 90 collagen molecules in cross-section, both axial spacing and micron scale persistence length were detected. These studies of self-assembled microfibril tapes on mica suggest there may be size threshold required before collagen microfibrils attain the persistence length and nanoscale morphology, as characterized by axial D-spacing, that is characteristic of collagen fibrils. The presence of the mica surface is a substantial perturbation[43] and additional efforts are required to understand the relationship of this size threshold to tissue self-assembly.

5.5 Acknowledgements.

MMBH is grateful for partial support from an MISP grant from Merck, Inc.

5.6 References

(1) *Collagen: Structure and Mechanics*; Fratzl, P., Ed.; Springer: New York, 2008.

(2) Kadler, K. E.; Baldock, C.; Bella, J.; Boot-Hanford, R. P. Collagens at a glance. *J. Cell Sci.* **2007**, *120*, 1955-1958.

(3) Kadler, K. E.; Holmes, D. F.; Trotter, J. A.; Chapman, J. A. Collagen fibril formation. *Biochemical Journal* **1996**, *316*, 1-11.

(4) Shoulders, M. D.; Raines, R. T.: Collagen Structure and Stability. In *Annual Review of Biochemistry*; Annual Review of Biochemistry, 2009; Vol. 78; pp 929-958.

(5) Hulmes, D. J. S. Building collagen molecules, fibrils, and suprafibrillar structures. *Journal of Structural Biology* **2002**, *137*, 2-10.

(6) Ottani, V.; Martini, D.; Franchi, M.; Ruggeri, A.; Raspanti, M. Hierarchical structures in fibrillar collagens. *Micron* **2002**, *33*, 587-596.

(7) Kadler, K. E.; Holmes, D. F.; Graham, H.; Starborg, T. Tip-mediated fusion involving unipolar collagen fibrils accounts for rapid fibril elongation, the occurrence of fibrillar branched networks in skin and the paucity of collagen fibril ends in vertebrates. *Matrix Biology* **2000**, *19*, 359-365.

(8) Holmes, D. F.; Kadler, K. E. The precision of lateral size control in the assembly of corneal collagen fibrils. *J. Mol. Biol.* **2005**, *345*, 773-784.

(9) Gross, J.; Schmitt, F. O. The Structure Of Human Skin Collagen As Studied With The Electron Microscope. *Journal of Experimental Medicine* **1948**, *88*, 555-568.

(10) Wallace, J. M. Applications of atomic force microscopy for the assessment of nanoscale morphological and mechanical properties of bone. *Bone* **2012**, *50*, 420-427.

(11) Jiang, F. Z.; Horber, H.; Howard, J.; Muller, D. J. Assembly of collagen into microribbons: effects of pH and electrolytes. *Journal of Structural Biology* **2004**, *148*, 268-278.

(12) Cisneros, D. A.; Hung, C.; Franz, C. A.; Muller, D. J. Observing growth steps of collagen self-assembly by time-lapse high-resolution atomic force microscopy. *Journal of Structural Biology* **2006**, *154*, 232-245.

(13) Orgel, J.; Irving, T. C.; Miller, A.; Wess, T. J. Microfibrillar structure of type I collagen in situ. *Proc. Natl. Acad. Sci. U. S. A.* **2006**, *103*, 9001-9005.

(14) Piez, K. A.; Trus, B. L. A New Model for Packing of Type-I Collagen Molecules in the Native Fibril. *Bioscience Reports* **1981**, *1*, 801-810.

(15) Smith, J. W. Molecular Pattern in Native Collagen. *Nature* **1968**, *219*, 157-&.

(16) Erickson, B.; Fang, M.; Wallace, J. M.; Orr, B. G.; Les, C. M.; Banaszak Holl, M. M. Nanoscale structure of type I collagen fibrils: Quantitative measurement of D-spacing. *Biotechnology Journal* **2013**, *8*, 117-126.

(17) Fang, M.; Goldstein, E. L.; Matich, E. K.; Orr, B. G.; Banaszak Holl, M. M. Type I Collagen Self-Assembly: The Roles of Substrate and Concentration. *Langmuir* **2013**, *29*, 2330-2338.

(18) Canty, E. G.; Kadler, K. E. Procollagen trafficking, processing and fibrillogenesis. *J. Cell Sci.* **2005**, *118*, 1341-1353.

(19) Schmitt, F. O.; Hall, C. E.; Jakus, M. A. Electron microscope investigations of the structure of collagen. *J. Cell. Comp. Phys.* **1942**, *20*, 11-33.

(20) Hall, C. E.; Jakus, M. A.; Schmitt, F. O. Electron microscope observations of collagen. *J. Am. Chem. Soc.* **1942**, *64*, 1234.

(21) Bear, R. S. Long x-ray diffraction spacing of collagen. *J. Am. Chem. Soc.* **1942**, *64*, 727.

(22) Bear, R. S. X-ray, diffraction studies on protein fibers I The large fiber-axis period of collagen. *Journal of the American Chemical Society* **1944**, *66*, 1297-1305.

(23) Hodge, A. J.; Petruska, J. A.: Recent Studies with the Electron Microscope on Ordered Aggregates of the Tropocollagen Molecule. In *Aspects of Protein Structure*; Ramachandran, G. N., Ed.; Academic Press: New York, 1963; pp 289.

(24) Orgel, J.; Antonio, J. D. S.; Antipova, O. Molecular and structural mapping of collagen fibril interactions. *Connective Tissue Research* **2011**, *52*, 2-17.

(25) Hulmes, D. J. S.; Wess, T. J.; Prockop, D. J.; Fratzl, P. Radial packing, order, and disorder in collagen fibrils. *Biophys. J.* **1995**, *68*, 1661-1670.

(26) Gautieri, A.; Vesentini, S.; Redaelli, A.; Buehler, M. J. Hierarchical Structure and Nanomechanics of Collagen Microfibrils from the Atomistic Scale Up. *Nano Lett.* **2011**, *11*, 757-766.

(27) Varma, S.; Botlani, M.; Hammond, J. R.; Scott, H. L.; Orgel, J. P. R. O.; Schieber, J. D. Effect of intrinsic and extrinsic factors on the simulated D-band length of type I collagen. *Proteins-Structure Function and Bioinformatics* **2015**, *83*, 1800-1812.

(28) Habelitz, S.; Balooch, M.; Marshall, S. J.; Balooch, G.; Marshall, G. W. In situ atomic force microscopy of partially demineralized human dentin collagen fibrils. *Journal of Structural Biology* **2002**, *138*, 227-236.

(29) Wallace, J. M.; Chen, Q.; Fang, M.; Erickson, B.; Orr, B. G.; Banaszak Holl, M. M. Type I Collagen Exists as a Distribution of Nanoscale Morphologies in Teeth, Bones, and Tendons. *Langmuir* **2010**, *26*, 7349-7354.

(30) Wallace, J. M.; Erickson, B.; Les, C. M.; Orr, B. G.; Banaszak Holl, M. M. Distribution of Type I Collagen Morphologies in Bone: Relation to Estrogen Depletion in Bone. *Bone* **2010**, *46*, 1349-1354.

(31) Wallace, J. M.; Orr, B. G.; Marini, J. C.; Banaszak Holl, M. M. Nanoscale Morphology of Type I Collagen is Altered in the Brtl Mouse Model of Osteogenesis Imperfecta. *J. Struct. Biology* **2011**, *173*, 146-152.

(32) Fang, M.; Banaszak Holl, M. M. Variation in Type I Collagen Fibril Nanomorphology: The Significance and Origin. *BoneKey* **2013**, *2*, 394.

(33) Fang, M.; Goldstein, E. L.; Turner, A. S.; Les, C. M.; Orr, B. G.; Fisher, G. J.; Welch, K. B.; Rothman, E. D.; Banaszak Holl, M. M. Type I Collagen D-Spacing in Fibril Bundles of Dermis, Tendon, and Bone: Bridging between Nano- and Micro-Level Tissue Hierarchy. *ACS Nano* **2012**, *6*, 9503-9514.

(34) Fang, M.; Liroff, K. G.; Turner, A. S.; Les, C. M.; Orr, B. G.; Banaszak Holl, M. M. Estrogen Depletion Results in Nanoscale Morphology Changes in Dermal Collagen. *J. Invest. Dermatol.* **2012**, *132*, 1791-1797.

(35) Bart, Z. R.; Hammond, M. A.; Wallace, J. M. Multi-scale analysis of bone chemistry, morphology and mechanics in the oim model of osteogenesis imperfecta. *Connective Tissue Research* **2014**, *55*, 4-8.

(36) Gallant, M. A.; Brown, D. M.; Hammond, M.; Wallace, J. M.; Du, J.; Deymier-Black, A. C.; Almer, J. D.; Stock, S. R.; Allen, M. R.; Burr, D. B. Bone cell-independent benefits of raloxifene on the skeleton: A novel mechanism for improving bone material properties. *Bone* **2014**, *61*, 191-200.

(37) Hammond, M. A.; Gallant, M. A.; Burr, D. B.; Wallace, J. M. Nanoscale changes in collagen are reflected in physical and mechanical properties of bone at the microscale in diabetic rats. *Bone* **2014**, *60*, 26-32.

(38) Gonzalez, A. D.; Gallant, M. A.; Burr, D. B.; Wallace, J. M. Multiscale analysis of morphology and mechanics in tail tendon from the ZDSD rat model of type 2 diabetes. *Journal of Biomechanics* **2014**, *47*, 681-686.

(39) Kemp, A. D.; Harding, C. C.; Cabral, W. A.; Marini, J. C.; Wallace, J. M. Effects of tissue hydration on nanoscale structural morphology and mechanics of individual Type I collagen fibrils in the Brtl mouse model of Osteogenesis Imperfecta. *Journal of Structural Biology* **2012**, *180*, 428-438.

(40) Warden, S. J.; Galley, M. R.; Hurd, A. L.; Wallace, J. M.; Gallant, M. A.; Richard, J. S.; George, L. A. Elevated Mechanical Loading When Young Provides Lifelong Benefits to Cortical Bone Properties in Female Rats Independent of a Surgically Induced Menopause. *Endocrinology* **2013**, *154*, 3178-3187.

(41) Odetti, P.; Aragno, I.; Rolandi, R.; Garibaldi, S.; Valentini, S.; Cosso, L.; Traverso, N.; Cottalasso, D.; Pronzato, M. A.; Marinari, U. M. Scanning force microscopy reveals structural alterations in diabetic rat collagen fibrils: role of protein glycation. *Diabetes-Metabolism Research and Reviews* **2000**, *16*, 74-81.

(42) Loo, R. W.; Goh, M. C. Potassium Ion Mediated Collagen Microfibril Assembly on Mica. *Langmuir* **2008**, *24*, 13276-13278.

(43) Leow, W. W.; Hwang, W. Epitaxially Guided Assembly of Collagen Layers on Mica Surfaces. *Langmuir* **2011**, *27*, 10907-10913.

(44) Raspanti, M.; Viola, M.; Sonaggere, M.; Tira, M. E.; Tenni, R. Collagen fibril structure is affected by collagen concentration and decorin. *Biomacromolecules* **2007**, *8*, 2087-2091.

(45) Bozec, L.; van der Heijden, G.; Horton, M. Collagen fibrils: Nanoscale ropes. *Biophys. J.* **2007**, *92*, 70-75.

Chapter 6
Conclusions and Future Outlook

6.1 Summary of Key Findings

6.1.1 Estrogen Depletion and Drug Treatments Alter Nano and Microstructure at Multiple Hierarchical Levels

The structure of type I collagen was assessed at multiple hierarchical levels. The nanostructure was studied at the level of D-spacing and microstructure was studied at the level of individual fibrils as well as fibril alignment over a 3.5 μm^2 area. The effect of estrogen depletion and drug treatment was dependent on the hierarchical level being considered. D-spacing was only altered for fibrils in bundles in trabecular bone. In this case, the drug treatment groups exhibited statistically significant animal-to-animal variability in the D-spacing. Individual fibrils and their association with bundles or sheets was described in chapters 2[1] and 3[2] using the *Parallel/Oblique* hand-coding method. In this analysis, estrogen depletion and drug treatment only altered cortical bone. The trabecular bone was altered at the larger scale analysis using a fibril alignment parameter (FAP), Chapter 3.[2]

The work reported in Chapters 2 and 3 is unique from other work in this field. There were a total of 84 animals across five different treatment groups and 8,032 individual collagen fibrils measured. This is a much larger sample size relative to similar studies in the literature.[3] Additionally, there is a full and independent biological replicate in Chapter 2.

6.1.2 Pigment Epithelium Derived Factor Binds Heterogeneously in Rabbit Femur

Pigment epithelium derived factor (PEDF) was conjugated to 10 nm gold nanoparticles through a streptavidin/streptavidin-tag system. The gold nanoparticles were detected with phase images from tapping mode AFM as well as combined AFM-IR. Gold is harder than collagen and is expected to have a different phase lag than collagen in the phase image when imaging in tapping mode. The phase contrast of the phase images provided evidence that PEDF interacts with collagen

at the interfaces of bundles and sheets and not within the bundles or sheets. Additionally, in areas of high fibril disorder, PEDF interactions were observed along fibril edges and not on top of the fibrils. These observations suggest that PEDF binds heterogeneously in rabbit femur.

6.1.3 Type I Collagen Nanomorphology

Collagen molecules were self-assembled into collagen microfibrils and fibril tapes on mica and imaged with AFM. Imaging included the transition between microfibrils and fibril tapes as well as high resolution images of microfibrils within a fibril using a Carbon Nanotube tip that had a diameter of ~1 nm. Measurements of height, width, and D-spacing (when present) revealed that there is a size threshold that must be reached before a fibril has the persistence length to have a D-spacing. This threshold is estimated to be about 10 microfibrils or 90 collagen molecules in cross-section.

These conclusions are inconsistent with published models for the origin of D-spacing.[4,5] The Hodge-Petruska model proposes as two-dimensional stacking of collagen microfibrils in a regular pattern to produce one value for D-spacing (67 nm).[4] The Orgel model for the origin of D-spacing is an extension of the Hodge-Petruska model in three dimensions. This model requires collagen to be crystalline and only have one possible value for D-spacing. Additionally, D-spacing is present at the level of microfibrils in this model.[5] Chapter 5 presents data that is not consistent with these models. The Hodge-Petruska and Orgel models need to be refined in order to explain a distribution of D-spacings as well as a critical threshold of collagen microfibrils that must be reached before D-spacing is observed.

6.2 Future Directions

6.2.1 Detecting endogenous PEDF in rabbit femur

In Chapter 4, PEDF binding sites were detected using gold nanoparticles as a secondary tag and detecting the gold nanoparticles with AFM phase imaging and IR. However, it is unclear if the observed binding sites represent all PEDF binding sites or if they represent sites where PEDF can bind but didn't bind in the animal. These two possibilities are outlined in **Figure 6.1**. If there is no endogenous PEDF remaining on the sample, then the PEDF-Au nanoparticles are able to bind to any PEDF binding site on the bone surface (**Figure 6.1a**). As shown in **Figure 6.1b**, if endogenous PEDF is still present in the sample, then those binding sites would not be available

for binding with exogenous PEDF (containing the gold nanoparticles). In this case, any gold nanoparticles detected with AFM would represent sites on the bone surface that are available for PEDF binding but were not bound by PEDF in the animal.

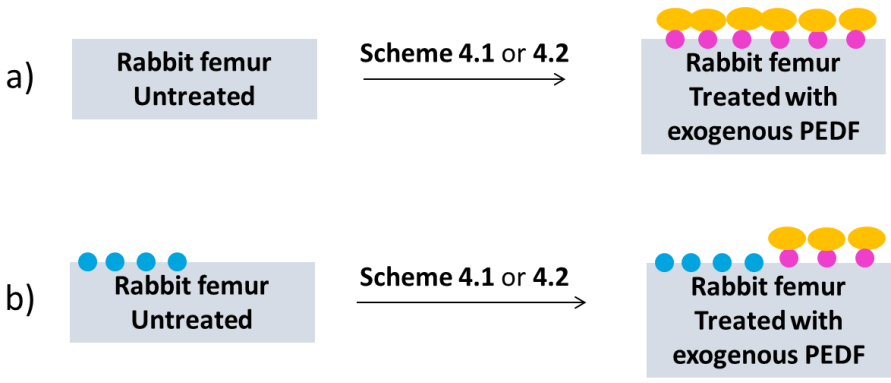

Figure 6.1 a) The freshly prepared (untreated) rabbit femur does not contain any endogenous PEDF from the animal. Upon exposure to exogenous PEDF (via PEDF-Au nanoparticles) using **Scheme 4.1** of **Scheme 4.2** (Chapter 4), PEDF will bind to any possible PEDF binding site on the surface of the femur sample. b) The freshly prepared (untreated) rabbit femur contains endogenous PEDF from the animal. These PEDF binding sites are not available for binding by exogenous PEDF. **Scheme 4.1** of **Scheme 4.2** will produce a sample in which the exogenous PEDF (PEDF-Au nanoparticles) binds to the femur surface at sites where PEDF can bind but didn't bind in the animal.

In order to test this, endogenous PEDF on the untreated femur samples will be stained and then detected by AFM phase imaging and IR. The procedures and possible outcomes are outlined in **Figure 6.2**. First, a freshly prepared rabbit femur will be exposed to a primary antibody (anti-PEDF antibody, Abcam ab14993, IgG, polyclonal). Then, the sample will be exposed to a secondary antibody (Goat Anti-Rabbit IgG, Abcam ab6720) that reacts with the primary antibody and is conjugated to biotin. The streptavidin protein binds with high affinity to biotin and can be used to attach a tag with gold nanoparticles. The same streptavidin-gold nanoparticles used in Chapter 4 (**Schemes 4.1, 4.2,** and **4.3**) will be used tag the secondary antibody. The gold nanoparticles will be detected using the same methods discussed in Chapter 4 (AFM phase imaging and AFM-IR). In the absence of endogenous PEDF, all antibodies and the streptavidin-Au nanoparticles will be washed away with buffer (**Figure 6.2a**). In the presence of endogenous

PEDF, the antibodies and streptavidin-Au nanoparticles will stain the surface at endogenous PEDF binding sites. In this case, it is expected that AFM phase imaging and AFM-IR would detect the presence of the gold nanoparticles (**Figure 6.2b**).

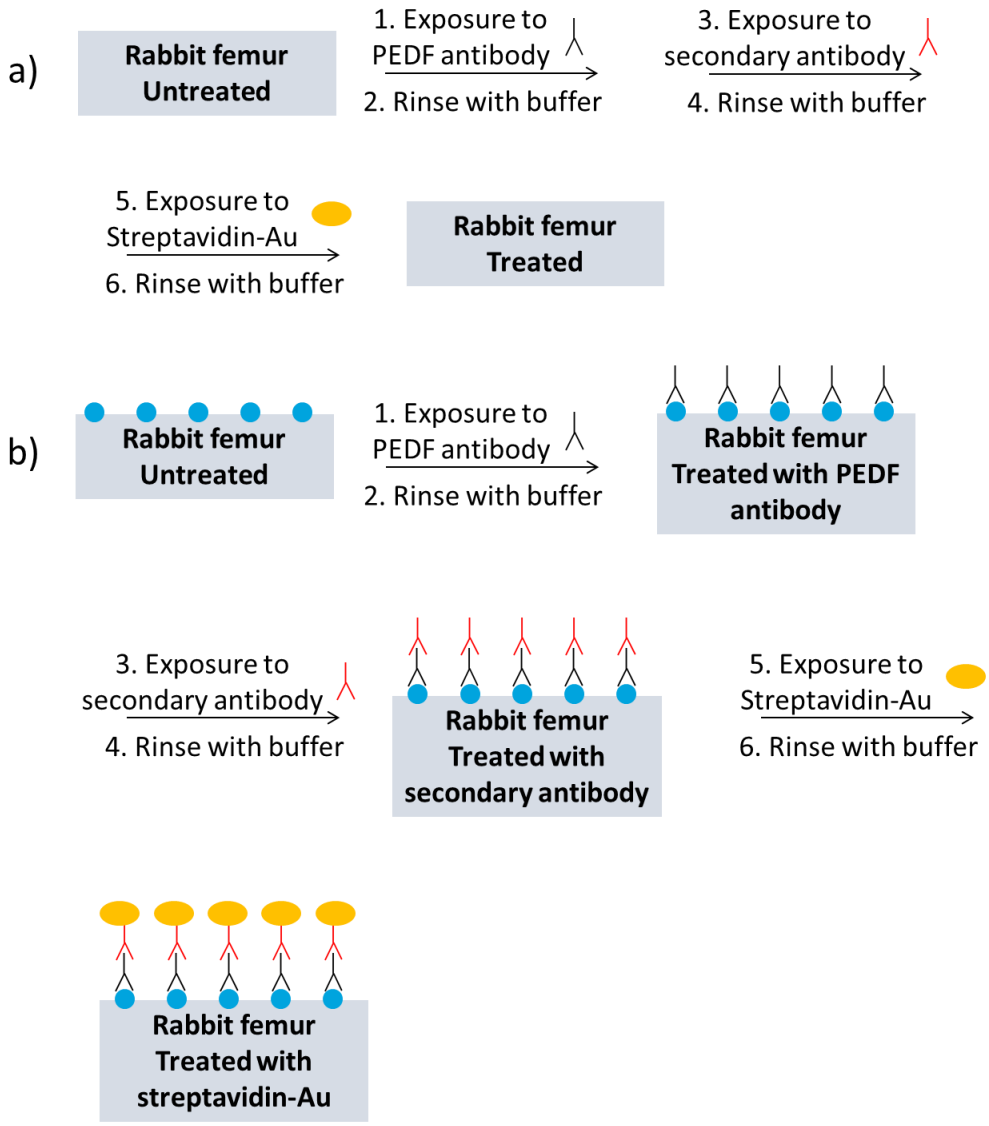

Figure 6.2 Endogenous PEDF will be detected using antibodies and streptavidin-Au nanoparticles. The primary antibody will be an antibody for rabbit PEDF. The secondary antibody will be a polyclonal IgG antibody that reacts with the primary antibody and is tagged with biotin. Streptavidin-Au will bind to biotin. a) Without endogenous PEDF, staining with antibodies and streptavidin-Au will result in a surface without gold nanoparticles on the surface. b) In the presence

of endogenous PEDF, staining with antibodies and streptavidin-Au will result in a surface with a gold nanoparticle at sites where endogenous PEDF is bound to the surface of the femur sample.

In Chapter 4, PEDF binding was heterogenous in rabbit femur. Due to this heterogeneity of binding and the heterogeneity of bone, it will be important to image many locations. Initial AFM scans are 10 x 10 μm and the polished surface of the femur is 1 cm x 0.75 cm on average. One 10 x 10 μm scan is only 0.00013% of the total polished surface available for imaging. If gold nanoparticles are present (there is endogenous PEDF), imaging many locations will increase the probability of randomly choosing a location with gold nanoparticles. The absence of gold nanoparticles in the AFM image could be attributed to the lack of endogenous PEDF or imaging a location that does not contain endogenous PEDF even if it is present elsewhere on the sample. In Chapter 2, six imaging locations were required to obtain data that was representative of the entire sample.[1] Imaging in a similar manner (six locations distributed evenly across the sample) should result in the detection of endogenous PEDF if it is present.

6.2.2 Comparing PEDF Binding Sites to Type I Collagen Microstructure

Chapter 3 described an automated image analysis that generated a fibril alignment parameter and associated heat map.[2] The heat maps provide a color scale that indicate areas or high collagen fibril alignment and low fibril alignment on an image. Using this analysis for the images of PEDF bound to bone could potentially allow us to observe relationships between collagen microstructure and PEDF binding events. The heat map could be overlaid on top of an image that showed gold nanoparticles. If the nanoparticles bind preferentially at certain areas of the color scale, this would be additional evidence that PEDF binding is heterogeneous in bone.

6.2.3 Detecting PEDF Binding Sites in Self-Assembled Collagen

Imaging locations of PEDF binding on self-assembled collagen microfibrils and fibrils will provide information to help explain the heterogeneity of binding observed in Chapter 4. In **Figure 6.3**, self-assembled collagen on mica from a 25 μg/mL collagen solution was exposed to 0.4 nM PEDF and 0.4 nM streptavidin-Au using **Scheme 4.1**. The microfibrils and fibril tapes on mica are small enough that the gold nanoparticles can be detected by height in the topography AFM image. For this sample, collagen microfibrils and fibril tapes were 2-5 nm in height (**Figure 6.3a**). Upon exposure to PEDF and streptavidin-Au, features with heights of 6-10 nm were present (**Figure**

6.3b). These features are likely the gold nanoparticles but the sample needs to be measured with AFM-IR to confirm the identity of the particles. **Figure 6.3c** displays a line scan along the fibril axis. The height of the particle is 7 nm with respect to the fibril. Height variation along the fibril due to D-spacing is much smaller than 7 nm. The PEDF/streptavidin-Au nanoparticles interact with the collagen fibril along the fibril axis (**Figure 6.3d**). Areas of the fibril tape without binding can be detected between the particles and this indicates that individual binding events are being detected.

The presence of the gold nanoparticles indicate that PEDF binding can occur in the absence of post-translational modifications that would occur in the animal. Additionally, there were no binding events observed between the nanoparticles and microfibrils. In Chapter 5, D-spacing was not observed in microfibrils but was observed for fibrils with greater than 90 collagen molecules. PEDF is a collagen chaperone protein and its inability to bind to microfibrils could be a biochemical explanation for the lack of D-spacing in microfibrils.

For this self-assembled sample, PEDF binding was detected along the fibril. This is inconsistent with binding observed in tissue (Chapter 4). PEDF finding is not observed on all fibril tapes or along an entire fibril. It is unclear if PEDF binds heterogeneously to a single fibril or if the PEDF/streptavidin-Au concentration was too low to observe all binding sites that are present. This experiment needs to be repeated at multiple concentrations of PEDF/streptavidin-Au to make the assessment. This type of experiment will provide information about the source of heterogeneous binding seen in tissue (Chapter 4). If PEDF binds homogenously along a fibril, then the heterogeneity of binding observed in bone is due to the heterogeneity of collagen microstructures. If PEDF binding is heterogeneous along the fibril, this could potentially explain the pattern of binding seen in bone.

I hypothesize that the heterogeneity seen in bone is both at the fibril level and at the level of microstructure. PEDF/collagen binding is sequence dependent[6,7] which explains heterogeneous binding along the fibril. Binding was not observed at areas of high collagen alignment in Chapter 4. Thus, the binding of PEDF in tissue is likely heterogeneous at both the fibril and microstructure level.

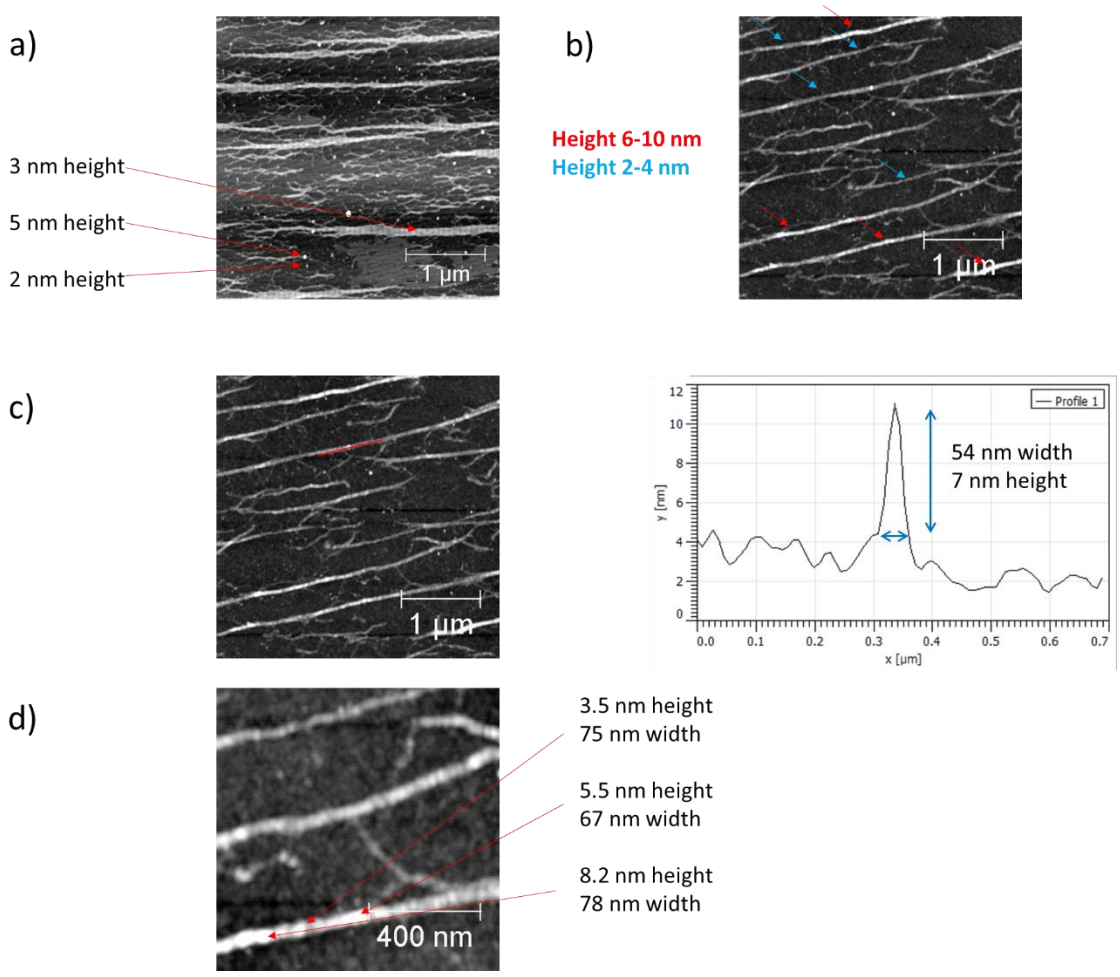

Figure 6.3 PEDF binding in self assembled microfibrils and fibril tapes. a) Self assembled collagen without exposure to PEDF, b) After exposure to PEDF, binding was detected along the axis of fibril tapes but not on microfibrils, c) Line scan along a fibril tape with one binding event detected, d) Individual binding events are detected along the fibril tape.

6.2.4 Nano and Micro Structural Changes with OI Type VI

Binding of pigment epithelium derived factor (PEDF) is dependent upon the microstructure of type I collagen in bone (Chapter 4). A loss of function mutation in the gene encoding PEDF results in osteogenesis imperfecta (OI) type VI[8,9] with a nano and microstructural defect in bone mineralization patterns.[10] Work still needs to be done to determine if collagen nano and microstructural changes are occurring with OI type VI. This is a likely hypothesis because mineralization occurs after collagen has been synthesized and the collagen fibrils template mineral formation.

The combined AFM-IR technique could potentially be useful in these experiments. The mineral component of bone also has a strong absorbance in the IR spectra. This technique has also been used to assess the mineral content (1030/1660 cm^{-1}) and crystallinity (1030/1020 cm^{-1}) of bone as well as the acid phosphate content (1128/1096 cm^{-1}).[11] This technique can be used to study the role of mineral in collagen microstructure.

6.2.5 Relating Nano and Microstructure Changes to Bone Remodeling Rates

In Chapters 2 and 3, the microstructure of type I collagen in bone was altered by estrogen depletion and drug treatment. The biochemical process that leads to various collagen microstructures is unknown but collagen microstructure must be determined during collagen synthesis (bone remodeling) or after synthesis (post-translational modifications). Bone remodeling rates for both cortical femur and trabecular lumbar vertebrae have been measured for the animals used throughout this thesis.[12] In this animal study, estrogen depletion resulted in cortical and trabecular bone loss. Treatment with either ALN or CatKI prevented OVX induced bone loss in both cases, demonstrating that both drugs are effective antiresorptives. Additionally, there was an increase in the bone formation rate with OVX treatment in both cortical and trabecular bone. OVX + ALN and OVX + ERT treated animals had bone formation rates that were not different from the Sham animals. This suggests that ALN and ERT cause a decrease in bone resorption and bone formation. Treatment with CatKI had no effect on bone formation rates in either cortical or trabecular bone. Bone resorption and formation are uncoupled under CatKI treatment.[12]

Due to the altered rates of bone formation, I hypothesize that microstructure is determined as the osteoblast is forming new bone during remodeling. Additional work is needed to test this hypothesis. One method could be to tag bone as it is being formed in the animal. Comparing collagen microstructure at sites of bone formation at the same point in time after OVX surgery (or Sham surgery) would provide information on how collagen microstructure is being altered with remodeling.

6.3 References

(1) Cauble, M. A.; Rothman, E.; Welch, K.; Fang, M.; Duong, L. T.; Pennypacker, B. L.; Orr, B. G.; Banaszak Holl, M. M. Alteration of Type I Collagen Microstructure Induced by Estrogen Depletion Can Be Prevented with Drug Treatment. *Bonekey Rep.* **2015**, *4*, 697.

(2) Cauble, M. A.; Muckley, M.; Fang, M.; Fessler, J.; Welch, K.; Rothman, E.; Orr, B. G.; Duong, L. T.; Banaszak Holl, M. M. Estrogen Depletion and Drug Treatment Alters the Microstructure of Type I Collagen in Bone. *Prep.* **2016**.

(3) Wallace, J. M.; Erickson, B.; Les, C. M.; Orr, B. G.; Banaszak Holl, M. M. Distribution of Type I Collagen Morphologies in Bone: Relation to Estrogen Depletion. *Bone* **2010**, *46*, 1349–1354.

(4) John A. Petruska; Hodge, A. J. A Subunit Model for the Tropocollagen Macromolecule. *Proc. Natl. Acad. Sci.* **1964**, *51*, 871–876.

(5) Orgel, J. P. R. O.; Irving, T. C.; Miller, A.; Wess, T. J. Microfibrillar Structure of Type I Collagen in Situ. *Proc. Natl. Acad. Sci. U. S. A.* **2006**, *103*, 9001–9005.

(6) Meyer, C.; Notari, L.; Becerra, S. P. Mapping the Type I Collagen-Binding Site on Pigment Epithelium-Derived Factor: Implications for Its Antiangiogenic Activity. *J. Biol. Chem.* **2002**, *277*, 45400–45407.

(7) Sekiya, A.; Okano-Kosugi, H.; Yamazaki, C. M.; Koide, T. Pigment Epithelium-Derived Factor (PEDF) Shares Binding Sites in Collagen with Heparin/heparan Sulfate Proteoglycans. *J. Biol. Chem.* **2011**, *286*, 26364–26374.

(8) Venturi, G.; Gandini, A.; Monti, E.; Carbonare, L. D.; Corradi, M.; Vincenzi, M.; Valenti, M. T.; Valli, M.; Pelilli, E.; Boner, A.; *et al.* Lack of Expression of SERPINF1, the Gene Coding for Pigment Epithelium-Derived Factor, Causes Progressively Deforming Osteogenesis Imperfecta with Normal Type I Collagen. *J. Bone Miner. Res.* **2012**, *27*, 723–728.

(9) Homan, E. P.; Rauch, F.; Grafe, I.; Lietman, C.; Doll, J. A.; Dawson, B.; Bertin, T.; Napierala, D.; Morello, R.; Gibbs, R.; *et al.* Mutations in SERPINF1 Cause Osteogenesis Imperfecta Type VI. *J. Bone Miner. Res.* **2011**, *26*, 2798–2803.

(10) Fratzl-Zelman, N.; Schmidt, I.; Roschger, P.; Roschger, A.; Glorieux, F. H.; Klaushofer, K.; Wagermaier, W.; Rauch, F.; Fratzl, P. Unique Micro- and Nano-Scale Mineralization Pattern of Human Osteogenesis Imperfecta Type VI Bone. *Bone* **2015**, *73*, 233–241.

(11) Gourion-Arsiquaud, S.; Marcott, C.; Hu, Q.; Boskey, A. L. Studying Variations in Bone Composition at Nano-Scale Resolution: A Preliminary Report. *Calcif. Tissue Int.* **2014**, *95*, 413–418.

(12) Pennypacker, B. L.; Duong, L. T.; Cusick, T. E.; Masarachia, P. J.; Gentile, M. A.; Gauthier,

J. Y.; Black, W. C.; Scott, B. B.; Samadfam, R.; Smith, S. Y.; *et al.* Cathepsin K Inhibitors Prevent Bone Loss in Estrogen-Deficient Rabbits. *J. Bone Miner. Res.* **2011**, *26*, 252–262.

Appendix A

Alteration of Type I Collagen Microstructure Induced by Estrogen Depletion can be Prevented with Drug Treatment Supplementary Information

Meagan A Cauble, Edward Rothman, Kathleen Welch, Ming Fang, Le T Duong, Brenda L Pennypacker, Bradford G Orr, and Mark M Banaszak Holl

Reprinted from BoneKEy Reports **4**, 697 (2015)

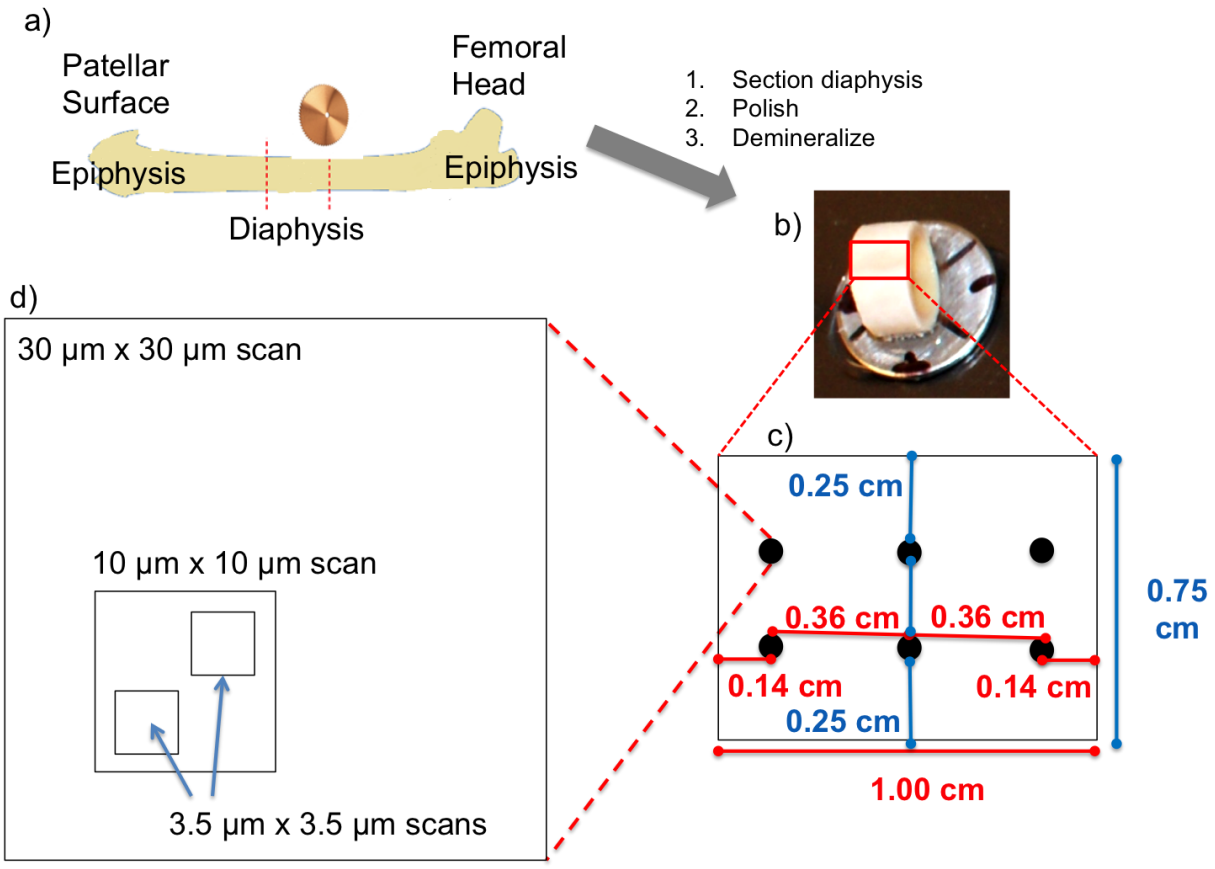

Figure A.1 Summary of sample treatment prior or imaging, imaging locations, and sampling with each location.

Approximately 1.0 cm of rabbit femur mid-diaphysis was sectioned and mounted onto an AFM puck (**Figure A.1b**). The sample area of 1.0 × 0.75 cm was polished 100-300 μm below the bone surface and demineralized for 90 minutes using EDTA. All images were acquired in the plane parallel to the long bone axis. No variation in collagen structure was noted as a function of the polishing depth employed. Image acquisition for the mid-diaphysis sections proceeded using the follow procedure. First, 30 × 30 μm scans were obtained in six regions of the 1.0 × 0.75 cm bone imaging area (**Figure A.1c**). These were followed by 10 × 10 μm scans and finally the 3.5 × 3.5 μm scans employed for image analysis (**Figure A.1d**). This approach ensured that the nano to micro scale analysis of collagen fibrils was distributed across the 0.75 × 1.0 cm imaging area. An average of six 30 × 30 μm scans and thirteen 3.5 × 3.5 μm scans were obtained per animal. From these regions, the average of 75 fibrils per animal was obtained around which the *Parallel* and *Oblique* microstructures were observed.

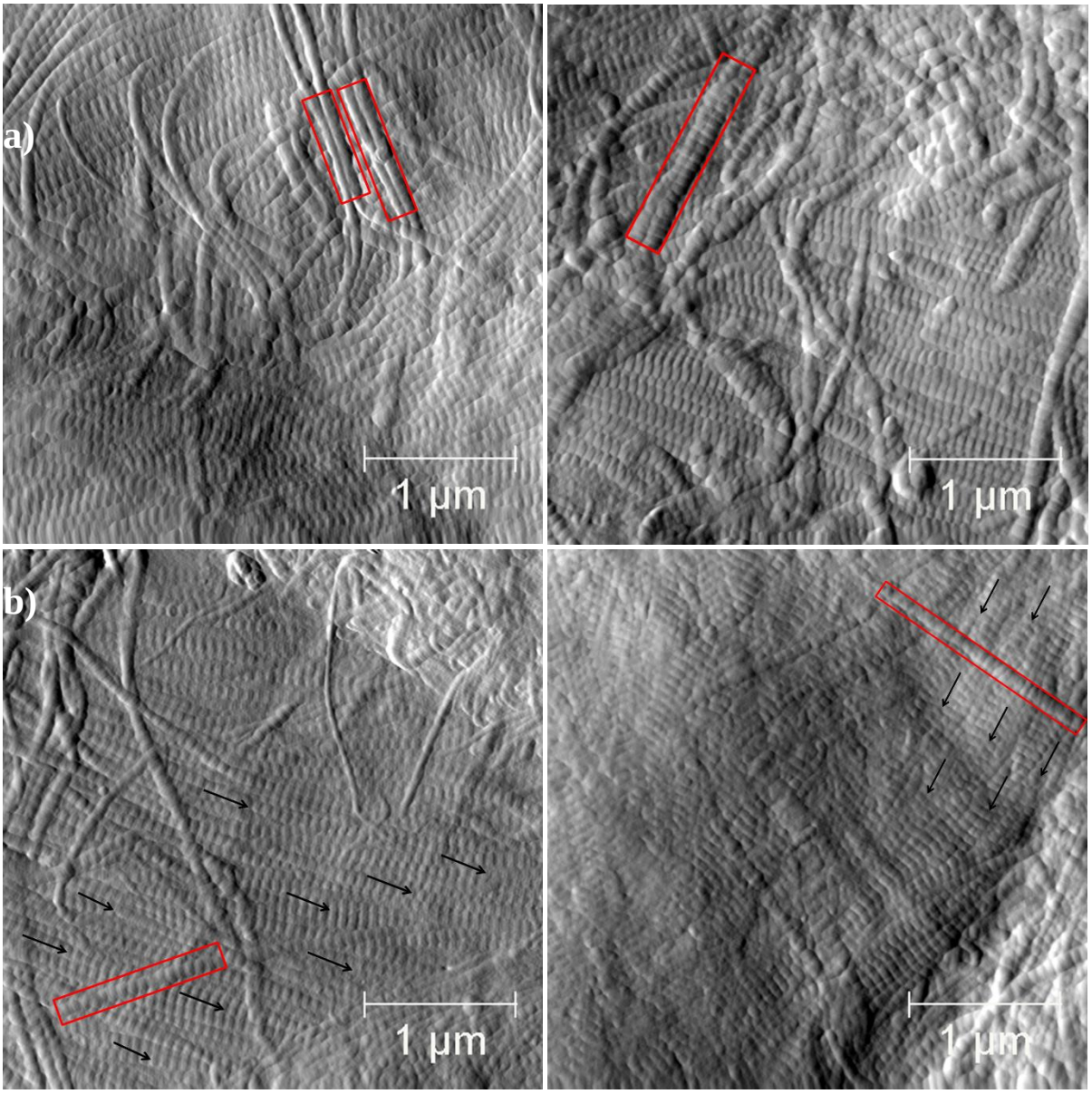

Figure A.2 Representative images of additional microarchitectures coded in both Data Sets I and II: a) fibril pair; b) fibril across bundle or sheet.

Statistical Analysis

D-spacing analysis employed a linear mixed ANOVA model with a random effect per animal and per index (bundles and sheets i.e. *Parallel* microstructure and *Oblique* microstructure). Mean D-spacings for fibrils in bundles were determined as a function of treatment group and were found to be 63.6, 64.0, 63.2, and 63.1 nm for Sham, OVX, OVX + ALN, and OVX + CatKI respectively with standard error of 0.4. These differences were not significant and had Tukey-Kramer adjusted p-values of >0.50. Mean D-spacings for fibrils in sheets were determined as a function of treatment group and were found to be 62.6, 63.9, 63.6, and 62.7 nm for Sham, OVX, OVX + ALN, and OVX + CatKI respectively with standard error of 0.4. These differences were not significant and had Tukey-Kramer adjusted p-values of >0.12. Thus, neither the sub-regions of the *Parallel* microstructure, nor the sum of the fibril sets, exhibited significant shifts in the D-spacing value. The largest variance arose from the between fibril differences within an animal that was 7.4 nm for bundles and 3.8 nm for sheets. Plots of the D-spacing distributions are illustrated in **Figure A.3**. Previous studies of Sham and OVX sheep noted a treatment dependent shift in D-spacing distribution.[1, 2] No changes in D-spacing distributions are noted for the studies of Sham, OVX, and drug treated rabbits.

a)

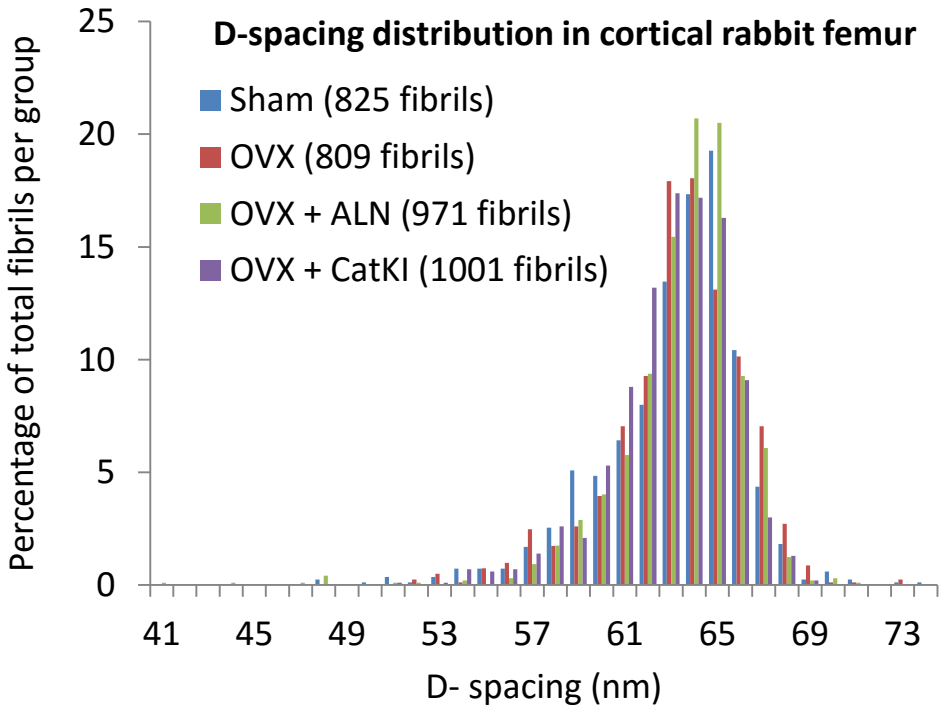

b)

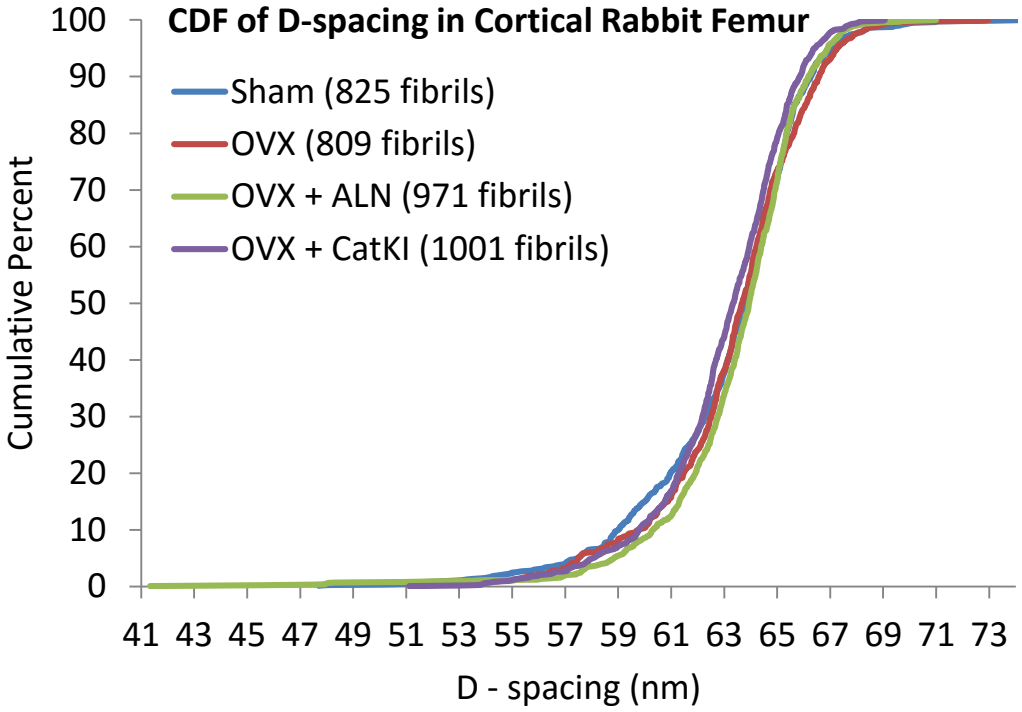
CDF of D-spacing in Cortical Rabbit Femur
Sham (825 fibrils)
OVX (809 fibrils)
OVX + ALN (971 fibrils)
OVX + CatKI (1001 fibrils)
Cumulative Percent
100
90
80
70
60
50
40
30
20
10
0
41 43 45 47 49 51 53 55 57 59 61 63 65 67 69 71 73
D - spacing (nm)

c)

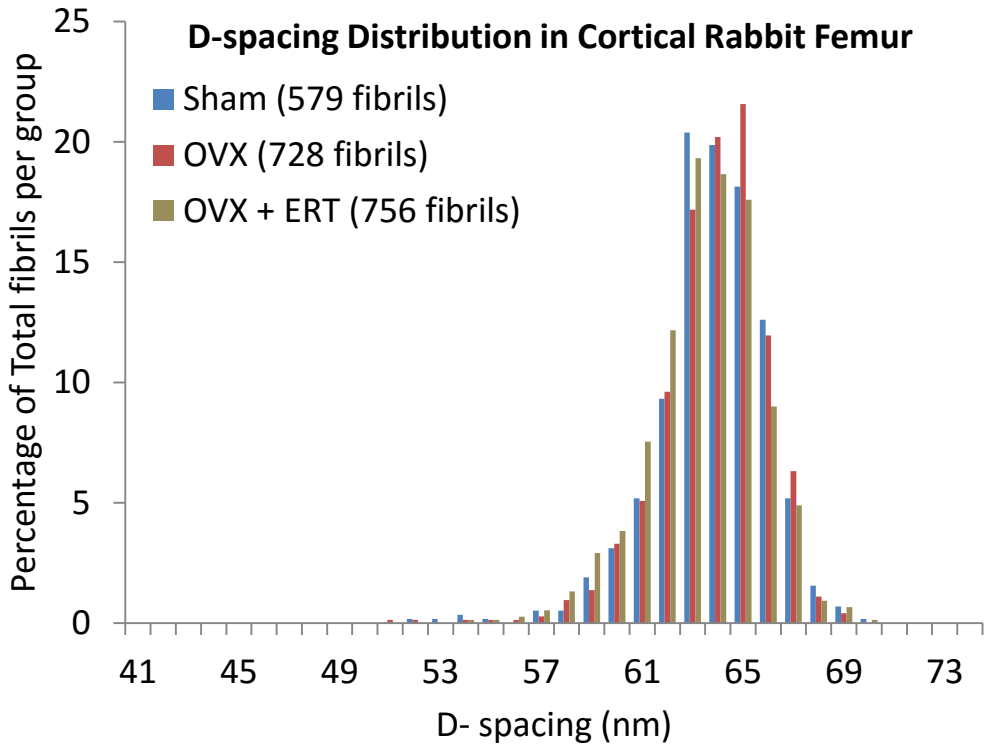
D-spacing Distribution in Cortical Rabbit Femur
Sham (579 fibrils)
OVX (728 fibrils)
OVX + ERT (756 fibrils)
Percentage of Total fibrils per group
25
20
15
10
5
0
41 45 49 53 57 61 65 69 73
D- spacing (nm)

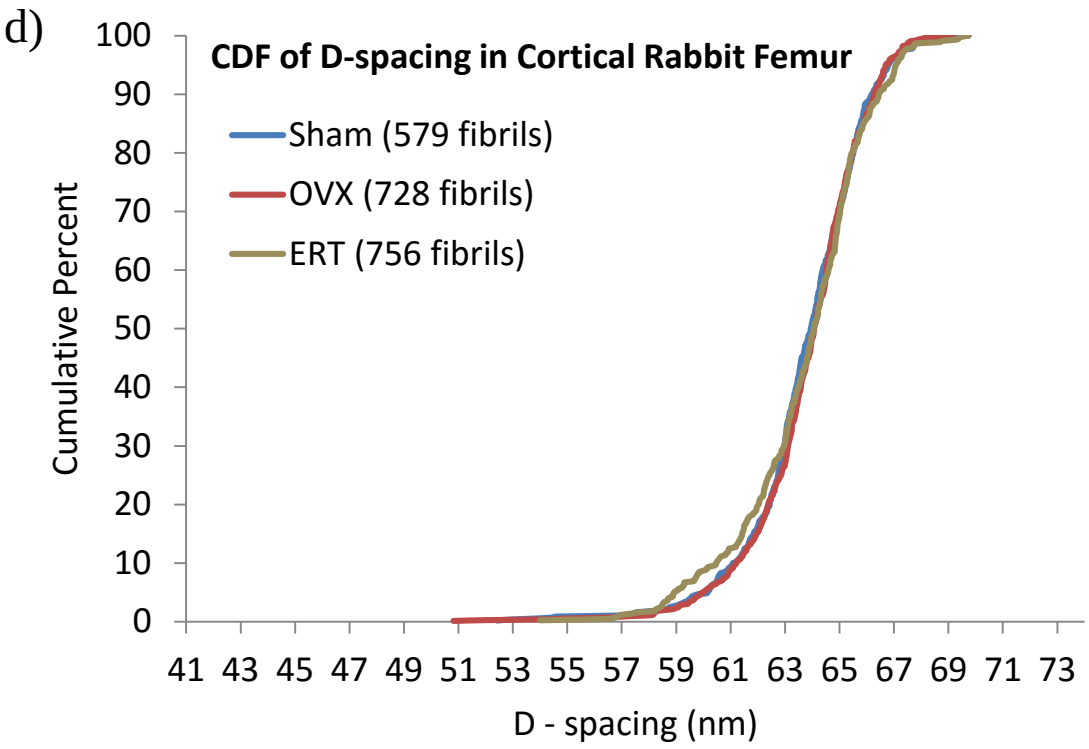

Figure A.3 D-spacing distributions for cortical bone from the mid-diaphysis of the rabbit femur. a) Histogram of D-spacing values for Sham, OVX, OVX + ALN, and OVX + CatKI (Data Set I), b) Cumulative density function of D-spacing values for Sham, OVX, OVX + ALN, and OVX + CatKI (Data Set I), c) Histogram of D-spacing values for Sham, OVX, and OVX + ERT (Data Set II), d) Cumulative density function of D-spacing values for Sham, OVX, and OVX + ERT (Data Set II).

1. Fang, M., Liroff, K.G., Turner, A.S., Les, C.M., Orr, B.G. & Banaszak Holl, M.M. Estrogen Depletion Results in Nanoscale Morphology Changes in Dermal Collagen. *J. Invest. Dermatol.* **132**, 1791-1797 (2012).
2. Wallace, J.M., Erickson, B., Les, C.M., Orr, B.G. & Banaszak Holl, M.M. Distribution of Type I Collagen Morphologies in Bone: Relation to Estrogen Depletion in Bone. *Bone* **46**, 1349-1354 (2010).

Figure A.4 Representative images from the Sham, OVX, OVX + ALN, OVX + CatKI, and OVX + ERT data sets.

Figure A.4.1 Sham animals in Data Set I (i and ii) and Data Set II (iii and iv).

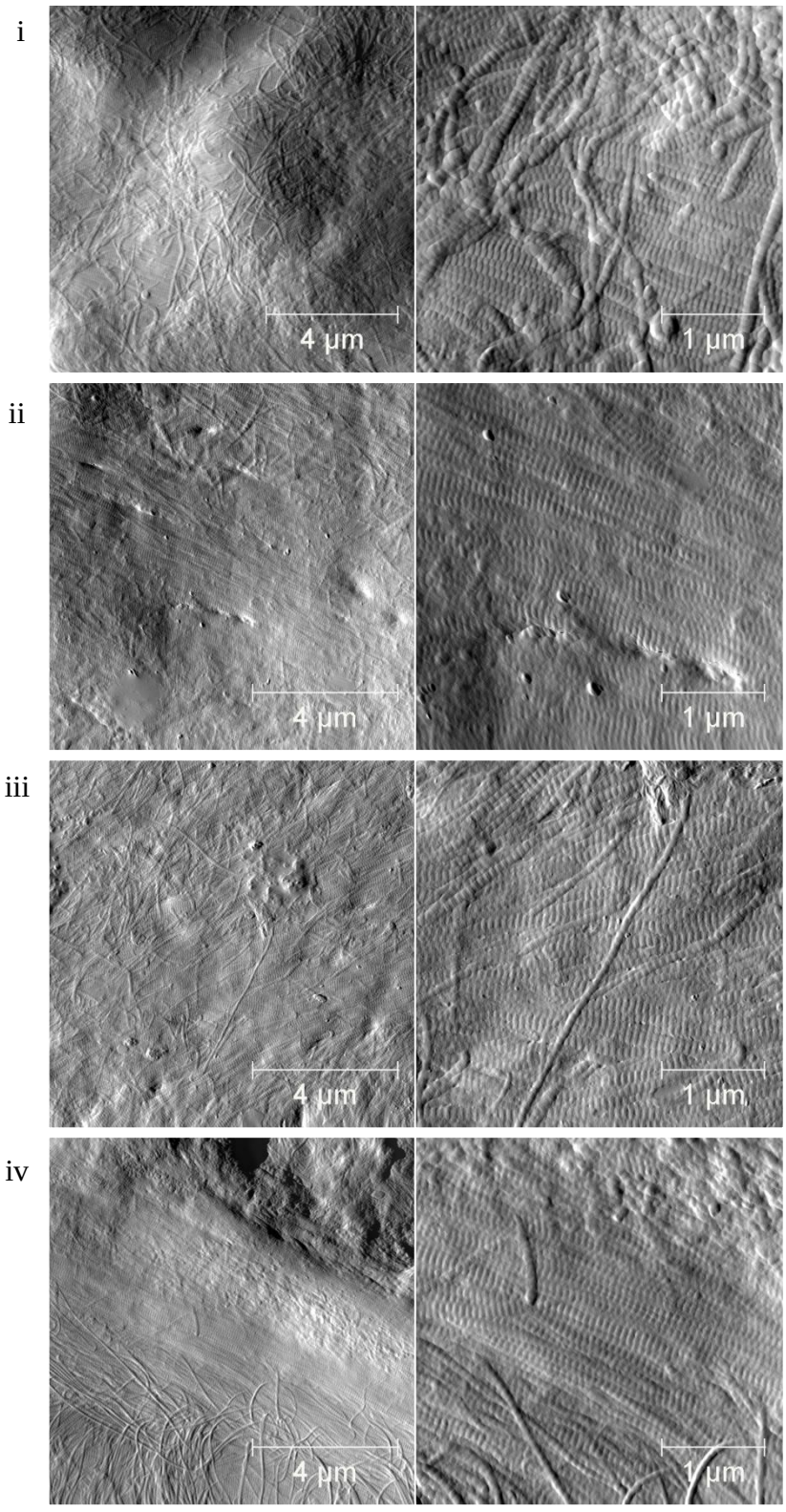

Figure A.4.2 OVX animals in Data Set I (i and ii) and Data Set II (iii and iv).

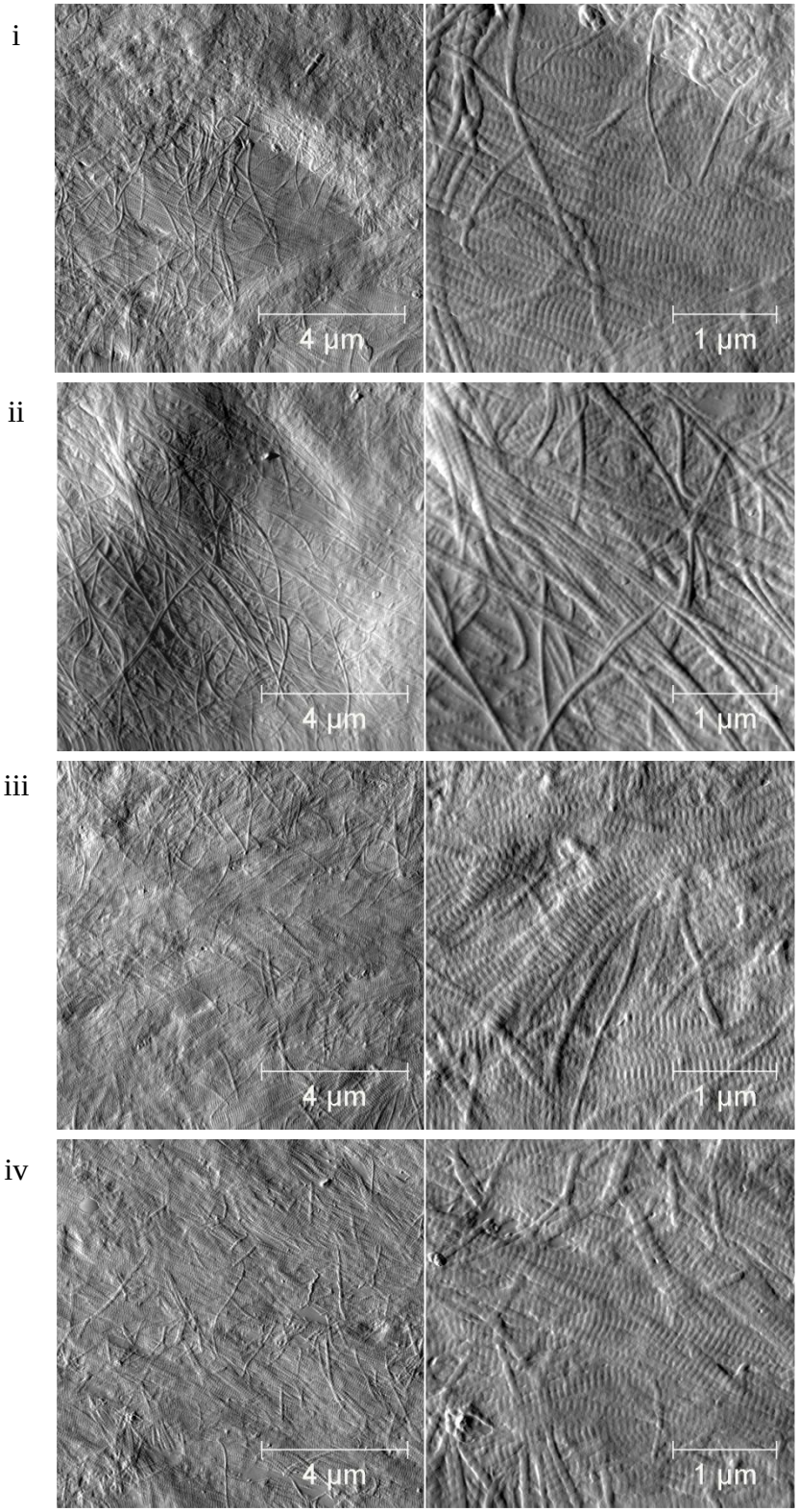

Figure A.4.3 OVX + ALN animals in Data Set I.

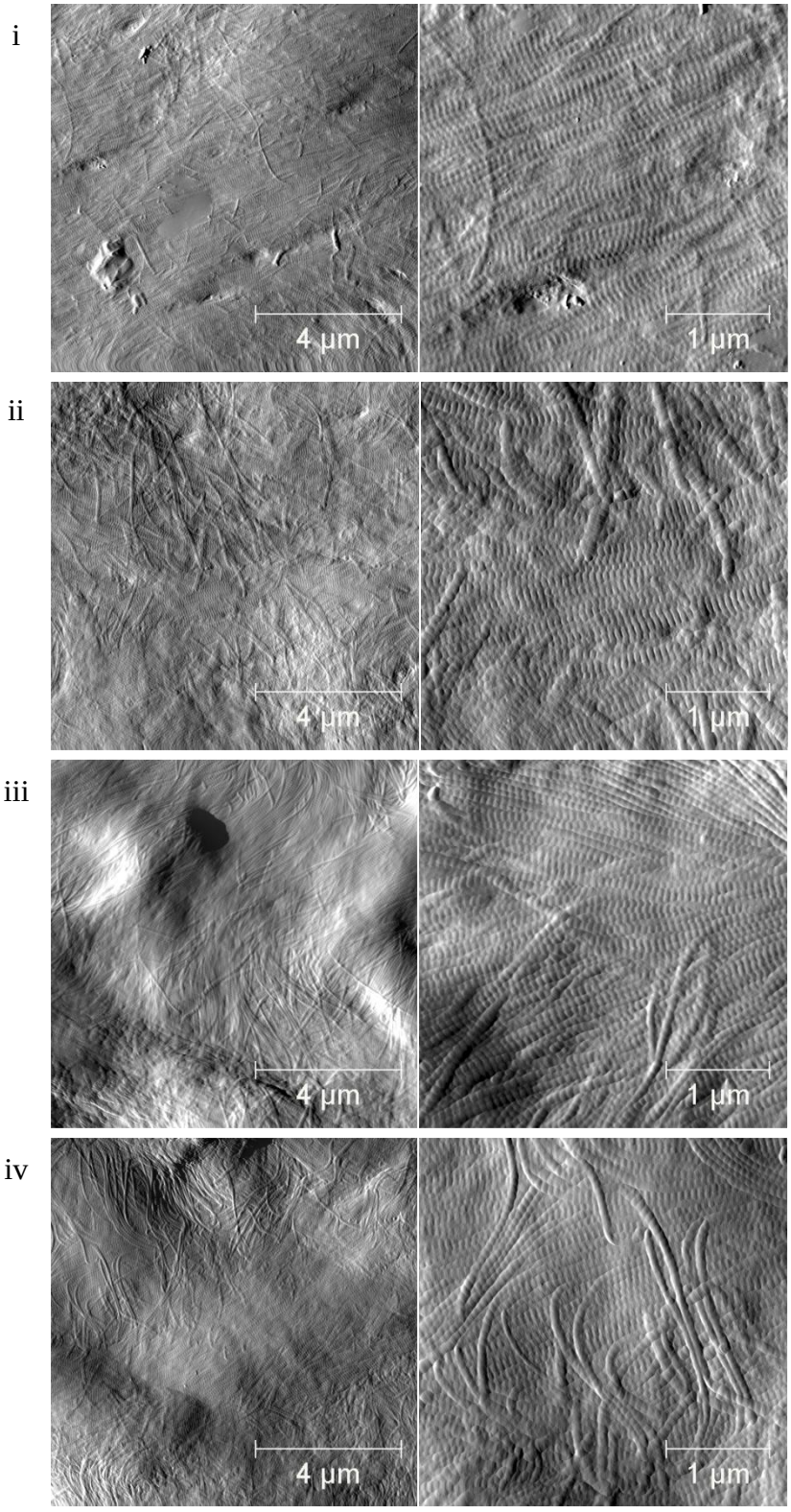

Figure A.4.4 OVX + CatKI animals in Data Set I.

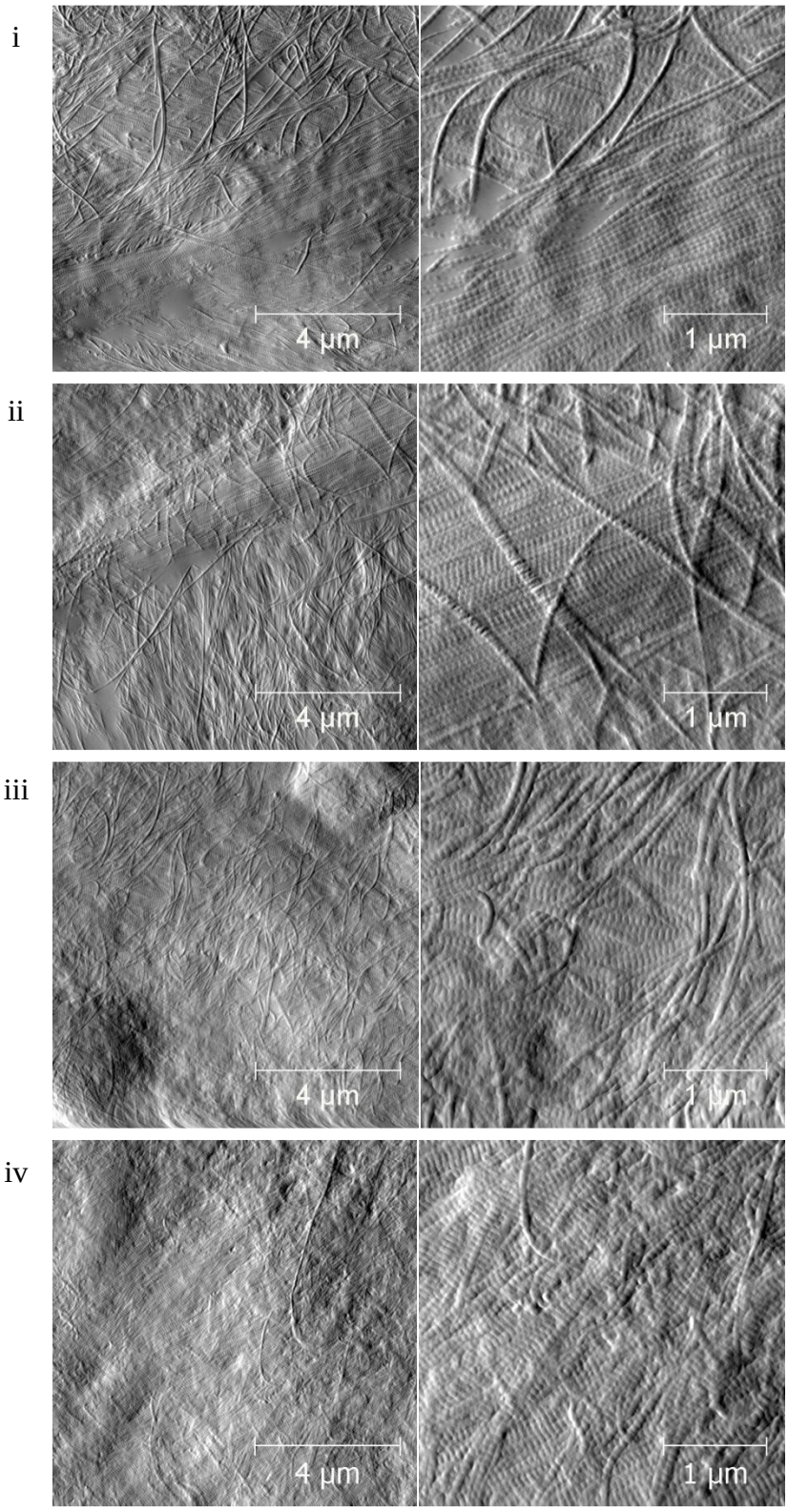

Figure A.4.5 OVX + ERT animals in Data Set II.

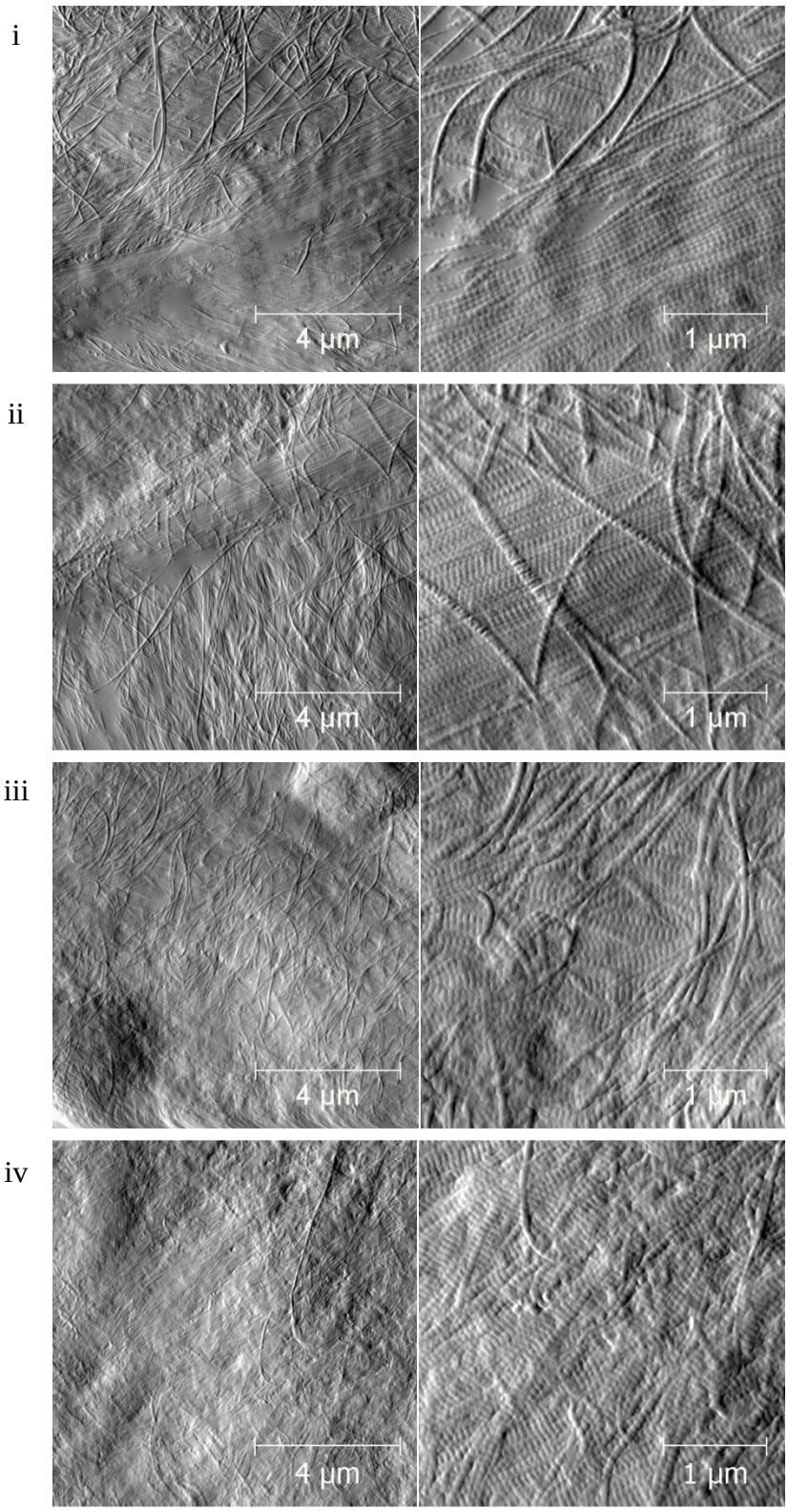

Appendix B

Estrogen Depletion and Drug Treatment Alters the Microstructure of Type I Collagen in Bone

In collaboration with Matt Muckley, Dr. Ming Fang, Prof. Jeffrey A. Fessler, Dr. Kathleen Welch, Prof. Edward D. Rothman, Prof. Bradford G. Orr, Dr. Le T. Duong, and Prof. Mark M. Banaszak Holl

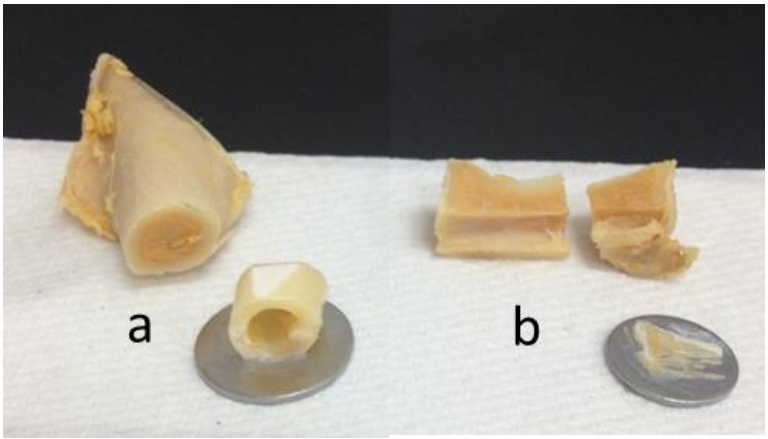

Figure B.1 Rabbit femur and lumbar vertebrae a) A section of rabbit femur was taken from the mid-diaphysis and mounted onto a steel puck. The remaining femur is shown behind the mounted sample. The mounted sample has been demarrowed, polished, and demineralized. b) The rabbit lumbar vertebrae sections were taken from the caudal end of the vertebrae. The mounted sample pictured has been demarrowed, polished, and demineralized.

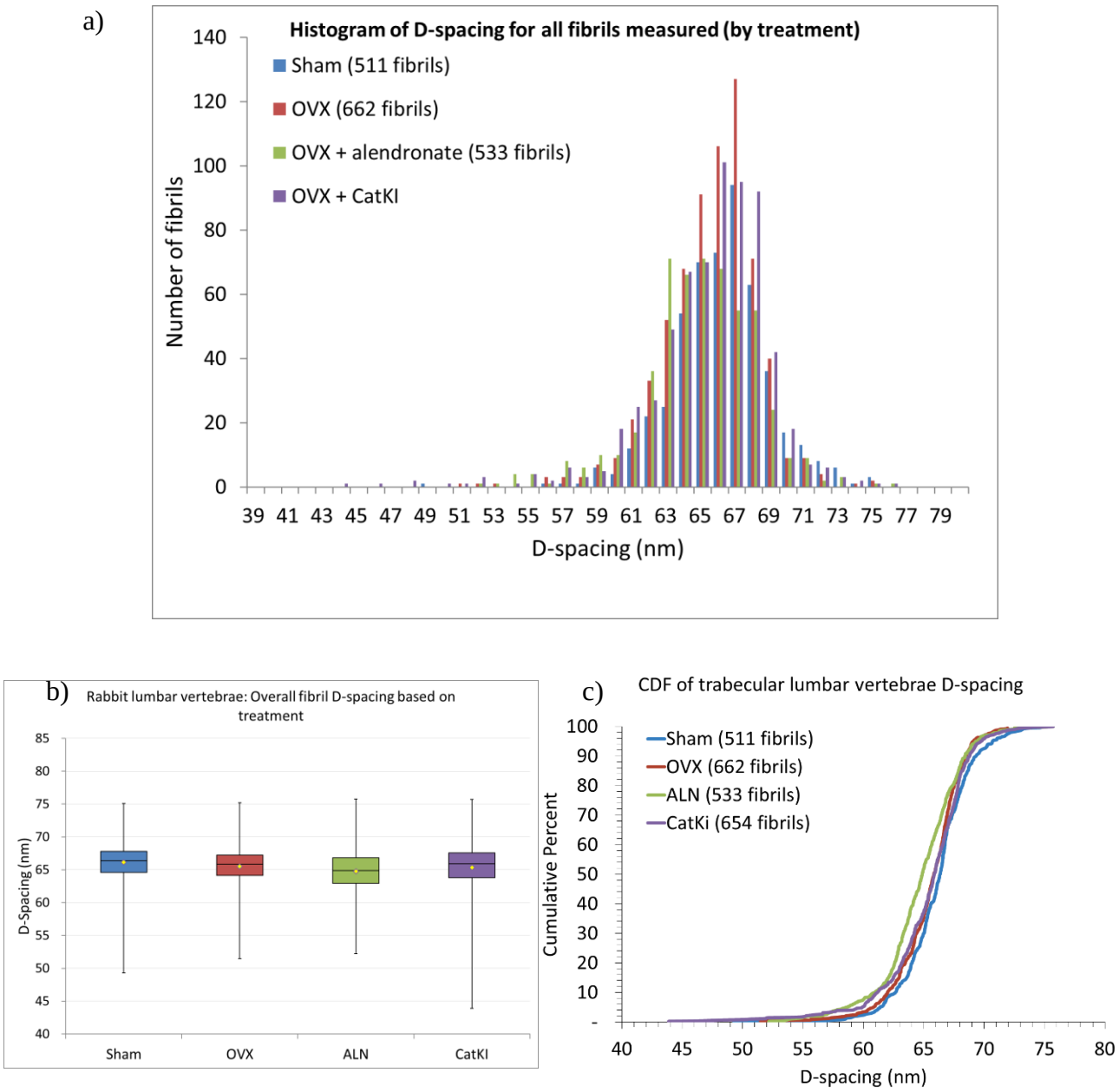

Figure B.2 Summary of D-spacing distributions in rabbit lumbar vertebrae. a) Histogram of all D-spacings measured for trabecular lumbar vertebrae, b) Boxplots of all D-spacings measured for trabecular lumbar vertebrae, c) Cumulative density function (CDF) of all D-spacings measured for trabecular lumbar vertebrae. There is not a significant difference between the average D-spacing values or the distribution of all D-spacing values as assessed by the Kolmorgorov-Smirnov statistic of the CDF.

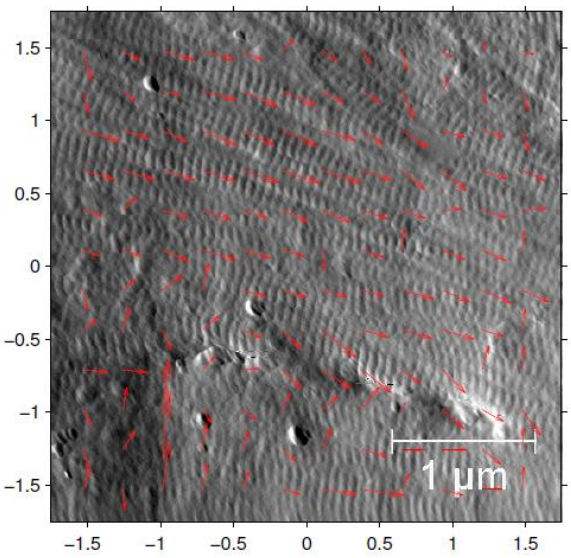

Figure B.3 Image of collagen, with arrows showing local alignment of collagen patches. The alignment was determined using an autocorrelation-based method. The arrow lengths are scaled to show the degree of alignment.

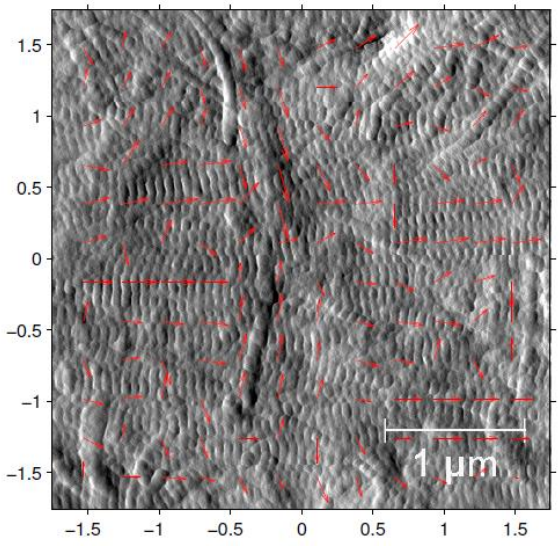

Figure B.4 Image of collagen, with arrows showing local alignment of collagen patches. The alignment was determined using an autocorrelation-based method. The arrow lengths are scaled to show the degree of alignment.

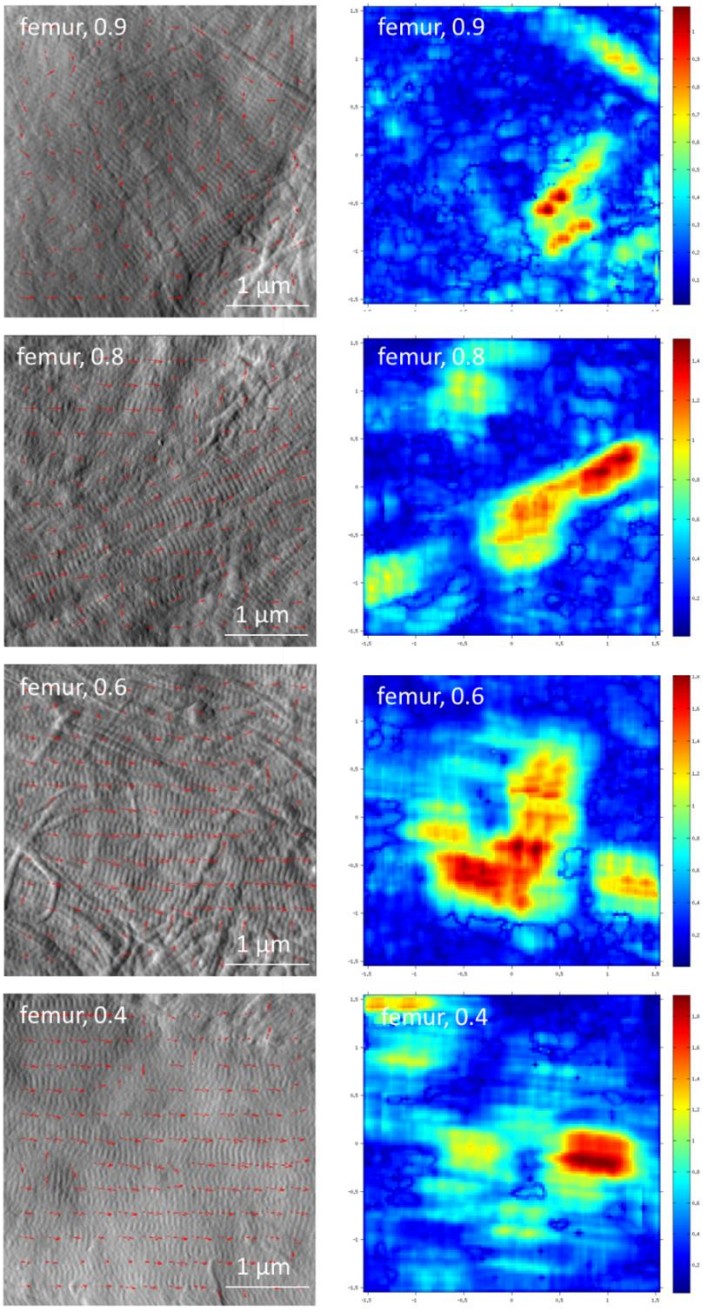

Figure B.5 Exemplary images of Sham rabbit cortical femur that correspond with **Figure 3.4b** with the superimposed vector fields and heat maps. The values included with each image are the fibril alignment parameter values.

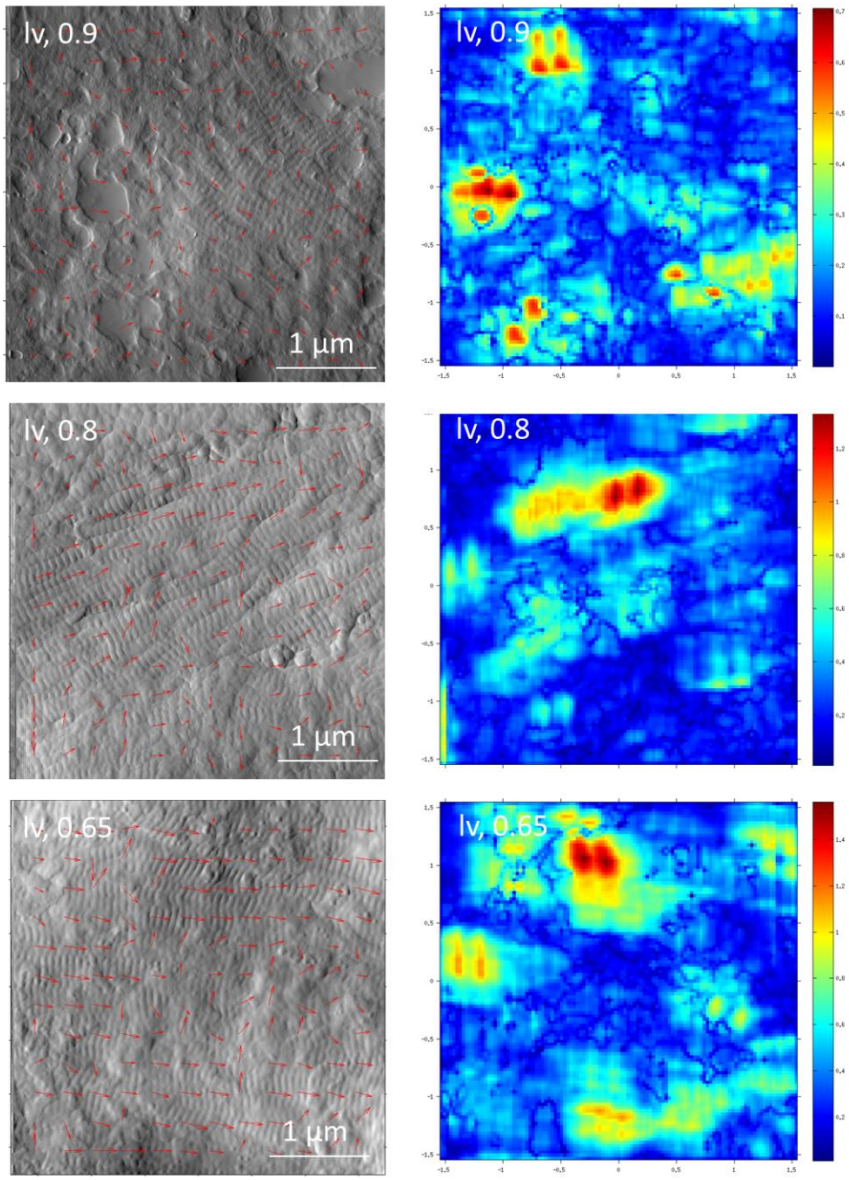

Figure B.6 Exemplary images of Sham rabbit trabecular lumbar vertebrae (lv) that correspond with **Figure 3.4b** with the superimposed vector fields and heat maps. The values included with each image are the fibril alignment parameter values.

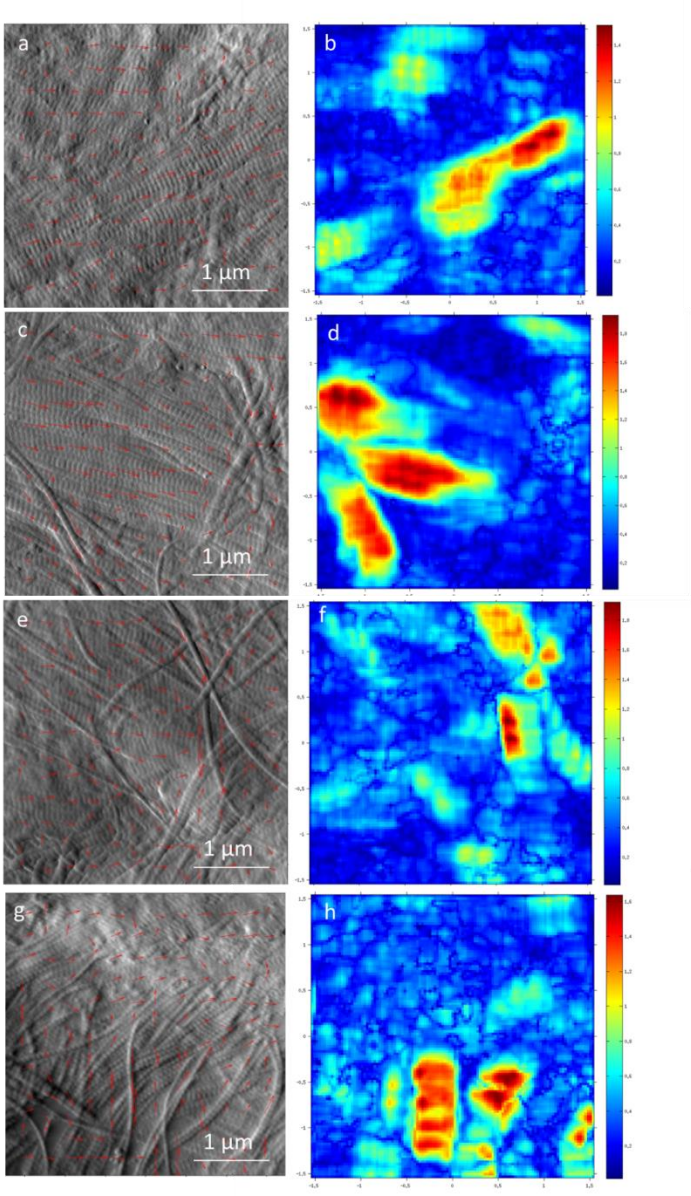

Figure B.7 Representative outputs from the autocorrelation-based analysis of AFM images from cortical femur samples. The left panel contains the amplitude AFM images with the superimposed vector fields. The arrows were calculated using the autocorrelation-based method (see **Figures B.3** and **B.4**). The right panel contains the corresponding heat maps. The heat maps show the alignment between a given vector with the vectors surrounding it. The images shown have approximately the same fibril alignment parameter (FAP) but come from different treatment groups. a-b) Sham, FAP = 0.8; c-d) OVX, FAP = 0.7; e-f) OVX + ALN, FAP = 0.9; and g-h) OVX + CatKI, FAP = 0.9.

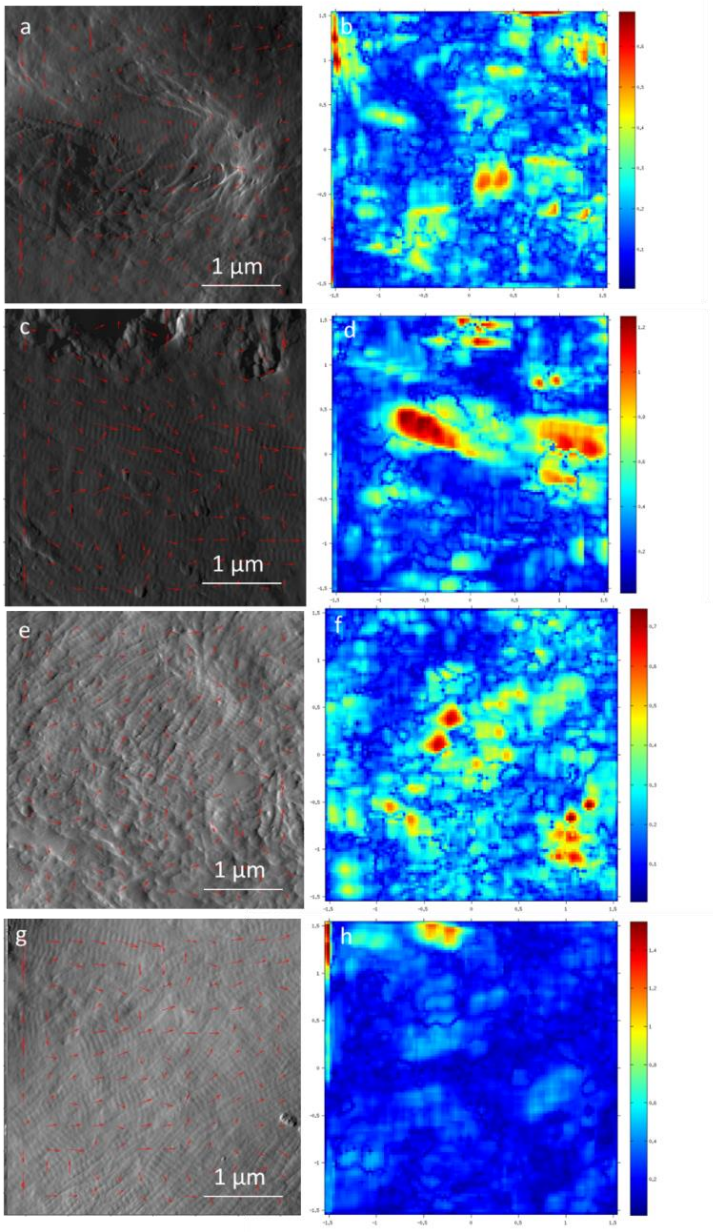

Figure B.8 Representative outputs from the autocorrelation-based analysis of AFM images from trabecular lumbar vertebrae samples. The left panel contains the amplitude AFM images with the superimposed vector fields. The arrows were calculated using the autocorrelation-based method (see **Figures B.3** and **B.4**). The right panel contains the corresponding heat maps. The heat maps show the alignment between a given vector with the vectors surrounding it. All images shown have a fibril alignment parameter (FAP) of 0.9 but come from different treatment groups. a-b) Sham, c-d) OVX, e-f) OVX + ALN, and g-h) OVX + CatKI.

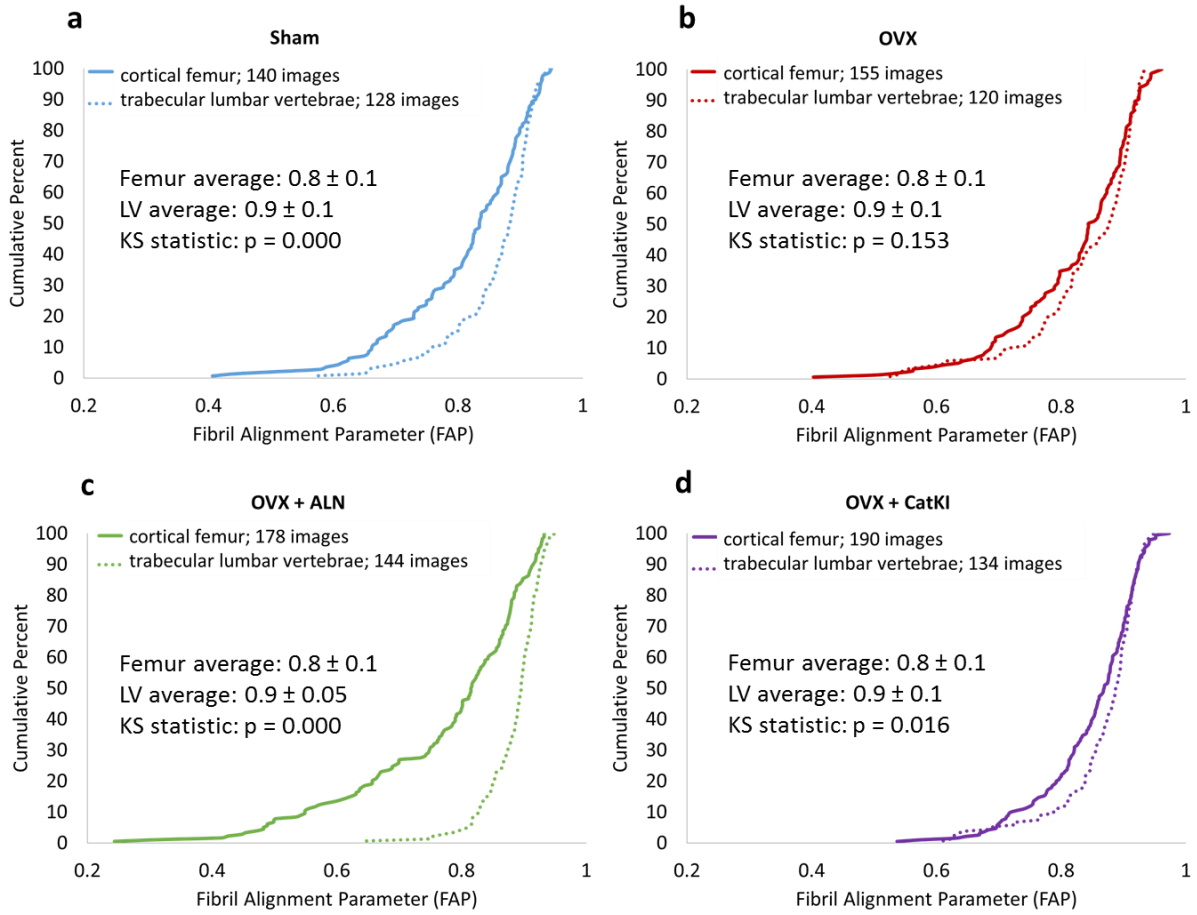

Figure B.9 Cumulative density function plots of FAP values to show the difference between cortical femur and trabecular lumbar vertebrae (lv) for each of the four treatment groups. For all plots, the average FAP value is the same for cortical and trabecular samples. a) The distribution of FAP values for Sham cortical femur is shifted towards lower values (more aligned collagen) in comparison to Sham trabecular lumbar vertebrae. b) Estrogen depletion resulted in cortical femur and trabecular lumbar vertebrae producing the same average and the same distribution of FAP values. The similarity in the distribution of FAP values arises from estrogen depletion shifting trabecular lumbar vertebrae towards lower FAP values while not affecting the cortical femur FAP values (**Figure 3.6**). OVX is the only treatment group with this result. c) OVX + ALN shifted cortical femur towards lower FAP values and trabecular lumbar vertebrae towards higher FAP values (**Figure 3.6**). As a result, cortical femur has a distribution of FAP values that are lower than trabecular lumbar vertebrae but the distributions are farther apart than Sham. d) OVX + CatKI cortical femur also has a distribution of FAP values that is shifted towards lower values.